(14)

Ultrasonic Phased Arrays for the Condition Assessment of Concrete Structures

by

Lawrence Azar

Submitted to the Department of Civil and Environmental Engineering
in partial fulfillment of the requirements for the degree of

Master of Science in Civil and Environmental Engineering

at the

MASSACHUSETTS INSTITUTE OF TECHNOLOGY

May 1998

Author .....
Department of Civil and Environmental Engineering
May 8, 1998

Certified by .....
Shi-Chang Wooh
Assistant Professor of Civil and Environmental Engineering
Thesis Supervisor

Accepted by .....
Joseph M. Sussman
Chairman, Departmental Committee on Graduate Students

Ultrasonic Phased Arrays for the Condition Assessment of Concrete Structures

by

Lawrence Azar

Submitted to the Department of Civil and Environmental Engineering
on May 8, 1998, in partial fulfillment of the
requirements for the degree of
Master of Science in Civil and Environmental Engineering

Abstract

Novel ultrasonic phased arrays were developed and the feasibility was tested for the condition assessment of concrete structures. These sensors are based on low frequency ultrasound technology, which is the preferred method for concrete testing to date. By combining multiple transducer elements in a linear configuration, dynamic phase focusing and/or steering of the ultrasound beam is possible. Using electronic scanning instead of mechanical scanning, these sensors eliminate the labor intensive physical relocation of a single element transducer. They realize high-resolution nondestructive evaluation (NDE) of concrete by enabling real-time two-dimensional imaging of the internal flaws and damage of concrete structures, a key improvement to current ultrasonic instruments utilized in Civil Infrastructure Systems (CIS).

A systematic approach using an automated testing assembly was used to assess the steering and focusing performance of the array in a cementitious medium. Experimental results agree well with numerical simulation presented. It was shown that the near field resolution can be greatly improved by electronically focusing the beam in the near field, and that phased arrays can be used as a primary imaging and scanning device for large-scale concrete structures.

Thesis Supervisor: Shi-Chang Wooh
Title: Assistant Professor of Civil and Environmental Engineering

Acknowledgments

First and foremost, I must extend my deepest thanks to my wife Pilar. Her confidence and love helped me through the toughest moments, and I would not be where I am without her undying support. I am greatly appreciative for all the sacrifices she has made for me, and am very proud of her own accomplishments at Boston College.

I must also thank my thesis advisor, Professor Shi-Chang Wooh, for all of his support and guidance. I thank him for expressing interest in me from the moment I arrived here at MIT, and nourishing my capabilities since. The knowledge I have gained from our experience together greatly exceeds my wildest expectations, and the confidence he instilled me with will forever be remembered.

Professor Eduardo Kausel deserves a special note of gratitude for his support and advice as my academic advisor. I have enjoyed our conversations, and his care and attention are greatly appreciated.

I express great thanks to my parents and Pilar's parents for all their support and faith. I could could not have made it this far without them. I also want to thank Jimmy, Sally, Pepo, and Patita for all their love and support.

Working with Coach Wei on many various project has been an enriching experience, that I will alway remember fondly. His generous nature and invaluable skills should never be underestimated. I look forward to our continued friendship.

I must thank Arthur Clay for sharing all his experiences in developing phased arrays for steel structures, and for sharing many of the key system components needed for my own research. His efforts greatly enhanced my own achievements here at MIT, and I wish him well.

Yijun Shi deserves special recognition for his analytical modeling, which has contributed greatly to my work.

I am grateful to Ji-yong Wang for his help with the sensor fabrication, and his general selfless nature.

Finally, I would like to thank all our friends at MIT, who have made our stay here so enjoyable.

Biographical Note

Lawrence Azar received his Bachelor of Science Degree from the University of California at Berkeley, where he majored in Civil Engineering (1992-1996). He then received a Master of Science from the Massachusetts Institute of Technology from the department of Civil and Environmental Engineering (1996-1998). While pursuing the Master's Degree, he was a graduate research assistant at the MIT Nondestructive Evaluation Laboratory, where he developed an ultrasonic phased array sensor to image and assess the condition of concrete structures. This sensor was submitted for patent approval at the time of this thesis submittal.

Lawrence was responsible for the design and testing of an ultrasonic detection system at P.P.B Inc. located in Palo Alto, CA in the summers of '95, '96 and '97. A semi-finalist at the 1998 MIT 50k Entrepreneurship Competition, he is in the process of starting up his own company, PASS Inc., which will manufacture ultrasonic phased arrays for the nondestructive testing industry. The following is a list of several current and pending publications.

1. L. Azar and S. C. Wooh, "A novel ultrasonic phased array for the nondestructive evaluation of concrete structures," *Review of Progress in QNDE Annual Conference*, Snowbird, Utah, July 1998.

2. L. Azar, Y. Shi, and S. C. Wooh, "Beam focusing behavior of linear phased arrays," submitted to *NDT&E International*, 1998.

3. S. C. Wooh and L. Azar, "Improved near field characteristics of phased arrays for assessing concrete and cementitious materials," *ASNT Fall Conference*," October, 1998.

4. A. C. Clay, S. C. Wooh, L. Azar, and J. Wang, "Experimental study of phased array beam steering characteristics," submitted to the *Journal of Nondestructive Evaluation*, 1998.

Contents

1 Introduction **13**

2 Condition Assessment of Concrete Structures **15**

2.1 Deterioration Mechanisms of Concrete Structures 15

2.2 Current Need for Nondestructive Evaluation 16

2.3 Current NDE Techniques for Concrete Structures 17

2.3.1 Radar 17

2.3.2 Infrared Thermography 19

2.3.3 Radiography 19

2.3.4 Stress Wave Methods 19

2.4 Overview of Stress Wave Techniques 19

2.4.1 Acoustic Emission (AE) 20

2.4.2 Pulse-Velocity 20

2.4.3 Impact-Echo 20

2.4.4 Spectral Analysis of Surface Waves (SASW) 20

2.4.5 Ultrasonic Testing (UT) 21

3 Ultrasonic Nondestructive Testing **22**

3.1 Fundamentals of Ultrasonic Wave Motion 22

3.2 Transmission and Reflection Coefficients 24

3.2.1 Acoustic Impedance 24

3.2.2 Normal Incident Waves 25
3.2.3 Oblique Incident Waves 26
3.3 Attenuation Coefficient for Concrete 27
3.4 Limitations of Current Ultrasonic Techniques for Concrete 29
3.5 Summary of NDT of Concrete 30

4 Ultrasonic Phased Array Transducers 31
4.1 Background of Ultrasonic Phased Arrays 31
4.1.1 Current Phased Array Applications 32
4.1.2 Fundamentals of Phased Arrays Technology 32
4.1.3 Other Types of Phased Array Configurations 36
4.2 Fundamentals of Phased Array Imaging 37
4.3 Fabrication Procedure for the Array Transducer 38
4.3.1 Conventional Single Element Construction 38
4.3.2 Phased Array Sensor Fabrication 41

5 Modeling of Focusing Pressure Distribution 48
5.1 Analytical Pressure Distribution for Focusing 49
5.1.1 Derivation of Focusing Formula 50
5.1.2 Analytical Pressure Distribution for Beam Focusing 52
5.2 Numerical Simulation and Analysis 53
5.2.1 Software Parameters 54
5.2.2 Single Element Characterization 55
5.3 Analysis of Beam Focusing Behavior 56
5.3.1 Numerical observations and discussion 56
5.3.2 Summary of Focusing Behavior 60

6 System Design and Experimental Setup 68
6.1 Pulser and Delay Circuit 68
6.1.1 Circuit Specification and Layout 68

6.1.2 Required Time Delays and Resolutions 69
6.2 Automated Testing Assembly 71
6.3 Experimental Testing Procedure 76

7 Experimental Results and Discussion **81**
7.1 Directivity Plots 81
7.2 Discussion 82
7.2.1 Steerability and Accuracy 84
7.2.2 Effects of d and N 84
7.2.3 Focusing Behavior 85
7.3 Summary and Conclusions 86

8 Conclusion **99**
8.1 Research Summary 99
8.2 Future Work and Concluding Remarks 100

A Analytical Pressure Distribution for Beam Focusing **103**
A.1 Time delay simplification 103
A.2 Analytical pressure distribution 105

List of Figures

2.1 The role of NDE in the life-cycle of civil infrastructure [12]. 18

3.1 Typical transducer arrangements: (a) pulse-echo, (b) through-transmission, and (c) pitch-catch. 23

3.2 Wave reflection, transmission and refraction: (a) normal incidence, (b) oblique incidence between two media, (c) obliquely-incident longitudinal wave at a free surface, and (d) obliquely-incident transverse wave at a free surface. 28

4.1 Linear array geometry and typical field of view. 33

4.2 Phase steered sound field of an array sensor. 34

4.3 Phase focused sound field of an array sensor. 35

4.4 Slotted transducer array design. 42

4.5 Single element pulse for mortar (f=170kHz, d=0.7λ, and c=3650m/s) and concrete (f=140kHz, d=0.58λ, and c=3500m/s), with their corresponding fast Fourier transforms. 45

4.6 Single element pulse acquired through the concrete wheel to ascertain the wavespeed of the material (R=30.48cm, ΔT=87.2μs, and c=3500m/s). 46

4.7 Phased array sensor: N=32, d=7.27mm, a=5.2mm, and D=22.3cm. . 46

4.8 Shielded cable. 47

5.1 Geometry of linear phased array needed for even-numbered focusing formula derivation. 51

5.2 Approach to modeling the numerical phased array pressure distribution: the array is an ensemble of multiple line sources, each of which is composed of an infinite number of point sources. 54
5.3 Single element directivities (R=30.48cm) for mortar (f=170kHz, d=0.7λ, and c=3650m/s) and concrete (f=140kHz, d=0.58λ, and c=3500m/s), both simulations include the cosine factor. 57
5.4 Steering in the near field. 62
5.5 Steer: N=16, c=36500m/s, f=170kHz, θ=30°, d=λ/2 and R=0.2m. . 62
5.6 Focusing in the near field. 63
5.7 Focus: N=16, c=3650m/s, f=170kHz, θ=30°, d=λ/2, F=0.2m and R=0.2m. 63
5.8 Steering in the far field. 64
5.9 Steer: N=16, c=3650m/s, f=170kHz, θ=30°, d=λ/2 and R=1m. . . . 64
5.10 Focusing in the far field. 65
5.11 Focus: N=16, c=3650m/s, f=170kHz, θ=30°, d=λ/2, F=1m and R=1m. 65
5.12 Comparison of pressure profiles along steered angle between steering and focusing in the near field and far field (N=16, c=3650m/s, f=170kHz, θ=30°, and d=λ/2). 66
5.13 Focusing in the near field, with directivities taken at various distances (N=16, c=3650m/s, f=170kHz, θ=30°, and d=λ/2). 67

6.1 Circuit layout for the 16-channel phased array system. 69
6.2 Steering delay and resolution in concrete (N=16, c=3500 m/s, d=1.454 cm, and F=30.48 cm). 72
6.3 Focusing delay in concrete (N=16, c=3500 m/s, d=1.454 cm, and F=30.48 cm). 73
6.4 Steering delay and resolution in concrete (N=8, c=3500 m/s, d=1.454 cm, and F=30.48 cm). 74
6.5 Steering delay and resolution in concrete (N=8, c=3500 m/s, d=1.454 cm, and F=30.48 cm). 75

6.6 Slotted concrete wheel mounted on motor controlled stand via an aluminum plate bolted to the back. 77
6.7 Concrete wheel in the water tank with a focused immersed transducer placed at the bottom for receiving the ultrasound, and the phased array transducer placed within the center of the wheel. 78
6.8 Complete setup, including wheel assembly, delay circuit, pulser/receiver, function generator and oscilloscope. 79
6.9 Experimental setup showing RS-232 motion control of step motor, GPIB for data acquisition and I/O board for steering control. 80

7.1 Experimental and simulated results demonstrating steering as compared to focusing behavior in mortar (R=30.48cm, F=30.48cm, N=8, c=3650m/s, f=170kHz, d=0.7λ, and θ=0^o). 87
7.2 Experimental and simulated results demonstrating steering as compared to focusing behavior in mortar (R=30.48cm, F=30.48cm, N=8, c=3650m/s, f=170kHz, d=0.7λ, and θ=15^o). 88
7.3 Experimental and simulated results demonstrating steering as compared to focusing behavior in mortar (R=30.48cm, F=30.48cm, N=8, c=3650m/s, f=170kHz, d=0.7λ, and θ=25^o). 89
7.4 Experimental and simulated results demonstrating steering as compared to focusing behavior in mortar (R=30.48cm, F=30.48cm, N=16, c=3650m/s, f=170kHz, d=0.7λ, and θ=0^o). 90
7.5 Experimental and simulated results demonstrating steering as compared to focusing behavior in mortar (R=30.48cm, F=30.48cm, N=16, c=3650m/s, f=170kHz, d=0.7λ, and θ=15^o). 91
7.6 Experimental and simulated results demonstrating steering as compared to focusing behavior in concrete (R=30.48cm, F=30.48cm, N=8, c=3500m/s, f=140kHz, d=0.582λ, and θ=0^o). 92

7.7 Experimental and simulated results demonstrating steering as compared to focusing behavior in concrete (R=30.48cm, F=30.48cm, N=8, c=3500m/s, f=140kHz, d=0.582λ, and θ=15^o). 93

7.8 Experimental and simulated results demonstrating steering as compared to focusing behavior in concrete (R=30.48cm, F=30.48cm, N=8, c=3500m/s, f=140kHz, d=0.582λ, and θ=25^o). 94

7.9 Experimental and simulated results demonstrating steering as compared to focusing behavior in concrete (R=30.48cm, F=30.48cm, N=8, c=3500m/s, f=140kHz, d=0.582λ, and θ=40^o). 95

7.10 Experimental and simulated results demonstrating steering as compared to focusing behavior in concrete (R=30.48cm, F=30.48cm, N=16, c=3500m/s, f=140kHz, d=0.582λ, and θ=0^o). 96

7.11 Experimental and simulated results demonstrating steering as compared to focusing behavior in concrete (R=30.48cm, F=30.48cm, N=16, c=3500m/s, f=140kHz, d=0.582λ, and θ=15^o). 97

7.12 Experimental and simulated results demonstrating the behavior of focusing at a constant directivity distance for various focal lengths: (R=30.48cm, N=16, c=3500m/s, f=140kHz, d=0.582λ, and θ=0^o). . . 98

8.1 Concrete sample, with a phased array sensor imaging voids and rebar. 102

List of Tables

3.1 Material properties. 24

3.2 Acoustic impedances for the components of concrete. 25

3.3 Acoustic impedances of various materials. 25

3.4 Reflection and transmission coefficients at normal incidence. 26

6.1 Specifications for phased array delay circuit. 70

6.2 Specifications for pulser and high voltage circuitry. 70

7.1 Z_{TR} values under various N and type of media 82

7.2 Summary of simulated and experimental results, demonstrating the accuracy and steerability of the directivities. For each case, results are given for steering followed by focusing. 83

Chapter 1

Introduction

The degradation of the civil infrastructure has placed a focus on effective nondestructive evaluation (NDE) techniques to correctly assess the condition of existing concrete structures. Conventional high frequency ultrasonic responses are severely affected by scattering and material attenuation, resulting in weak and confusing signal return [1]. Therefore, low frequency ultrasonic transducers, which avoid the problem of wave attenuation, are commonly used with concrete. The low frequency transducer avoids this potent attenuation due to its longer wavelength, causing the wave to go through unhindered, effectively ignoring inclusions which are smaller, such as porosity and aggregate. Some drawbacks do exist, such as poor resolution, signal-to-noise ratio, directivity and sensitivity [2].

This research relates to the assessment of concrete structures utilizing low-frequency ultrasonic phased array sensors. Phased array systems readily found in the medical, metal, and composite industries are not effective for concrete testing, since the frequencies used are too high by at least a factor of ten, and typically much more than this [3–7]. The contribution of a phased array approach is that it offers intrinsic signal processing capabilities that cannot be realized with a conventional single element transducer, allowing for detailed assessment of the object. A phased array system gathers quantitative measurements by electronically phase steering the acoustic beam rapidly throughout the object, rather than through mechanical means [3]. By using multiple piezo-elements excited with different time delays, the array can both steer

and focus the beam dynamically. Evaluation of the characteristics and flaws of concrete structures is possible in a quantitative and qualitative manner. These include determining the location, orientation, and size of cracks, delaminations, and existing reinforcing steel (rebar) [8].

A novel low-frequency ultrasonic phased array was developed, and its feasibility was tested for the assessment of concrete and other cementitious materials. The enlarged near field zone resulting from the immense size of the array, a consequence of the use of low frequency, authors in a "dead zone" where steering is not effective. Results show that the near field resolution can be greatly improved by electronically focusing the beam. A systematic approach, using an automated test assembly, was used to experimentally demonstrate the performance of steering and focusing of the array in a cementitious medium. The conclusion drawn from the experimental results is that phase steering and focusing ultrasound is possible in concrete and other cementitious media. The results demonstrated excellent steerability and accuracy, indicating that the phased array could be used as a primary imaging and scanning device for large-scale concrete structures.

Chapter 2

Condition Assessment of Concrete Structures

Deterioration of large scale structures, including an aging infrastructure, has become a central issue in reference to both safety and economic concerns. Priority on repair, replacement, and retrofitting must be evaluated, therefore making the development of a reliable, expeditious, and accurate nondestructive evaluation method essential.

2.1 Deterioration Mechanisms of Concrete Structures

The central deteriorating mechanism in concrete structures is cracking, caused by both chemical and physical processes. The former is due primarily to hydrolysis of the cement paste, cation-exchange inside the concrete, and formation of expansive products. The latter is due to both surface wear, which includes abrasion, erosion, cavitation, and cracking, derived from volume changes, structural loading, and exposure to temperature extremes [9]. Shrinkage cracks may be present even before the structure experiences any of its service loads. Once the loads are applied, additional shear and flexure cracks will appear. These will also worsen with cyclic loading.

Concrete is naturally porous, an effect of the evaporation of water needed for workability, leaving a continuous network of pores and capillaries. Water migration through the porosity network exerts significant pressure during freezing, causing the paste to fail. This can be described as scaling, local flaking or peeling away from the near surface portion of hardened concrete.

Corrosion of reinforcing steel greatly increases the volume of the original steel. This expansion causes the concrete to fracture, causing either feathered-edged surface cracks, spalling, or delamination. Dimensional loss, due to this spalling and delamination, can adversely affect the capacity of structural elements such as the slabs, beams, and columns. Corrosion by-products (e.g. rust) occupy a volume at least 2.5 times that of the parent metal [10].

2.2 Current Need for Nondestructive Evaluation

Developments of reliable NDE methods are critical with the growing concerns of deteriorating civil infrastructure systems (CIS), such as highways, railways, bridges, airports, subways, buildings, and power plants. Compared to metal and composite materials, where NDE techniques are readily applicable to *in-situ* testing, NDE in concrete is relatively undeveloped. The heterogeneous composition of concrete and high material attenuation, making detection of defects difficult to discern from naturally occurring inclusions, and the lack of an established failure criteria complicate the transition of NDE techniques to the field.

An estimated $450 billion per year is spent on the maintenance of CIS in the United States. An example of the crisis facing this country is the 576,460 bridges in the US, 23% of which are structurally deficient and 19% are obsolete [11]. Deterioration of existing structures is inevitable, but NDE offers a solution by detecting damage early, before more serious and expensive degradation occurs. The Loma Prieta and Northridge earthquakes have also demonstrated the need for more reliable and more efficient nondestructive inspection techniques which are can handle such abrupt, massive degeneration.

To limit the occurrence of such dramatic failures, the government has implemented guidelines to properly inspect and maintain the CIS. NDE plays an important role in the life cycle of a structure, as shown in figure 2.1. These include general inspection, condition monitoring, detailed inspection, and repair. The increasing recognition of the CIS deterioration opens the door for increased government support directed towards advances in nondestructive technology. Socio-economic concerns clearly justify the need for more research to achieve this goal, especially in the field of structural concrete, where existing efforts are lacking.

2.3 Current NDE Techniques for Concrete Structures

According to Malhotra and Carino [13], there are three principal categories for NDE methods for concrete: (1) methods to estimate the strength of the material, which include: surface hardness, penetration resistance, pullout test, break-off test, and maturity techniques, (2) methods that ascertain material properties, such as density, moisture content, dynamic elastic modulus, and sample thickness, and (3) methods that detect cracks, porosity, delamination, and reinforcing steel. These methods include: radar, infrared thermography, radiography, and stress wave techniques.

2.3.1 Radar

The principle of the radar technique is to generate and transmit electromagnetic impulse signals into a concrete element, and have the reflected pulse monitored and interpreted to detect voids, delamination, and reinforcing steel. The poor electromagnetic properties and high heterogeneity of concrete limit this method due to its low penetration capacity (for concrete thickness less than 0.6 m) [14], as well as cost [15–20].

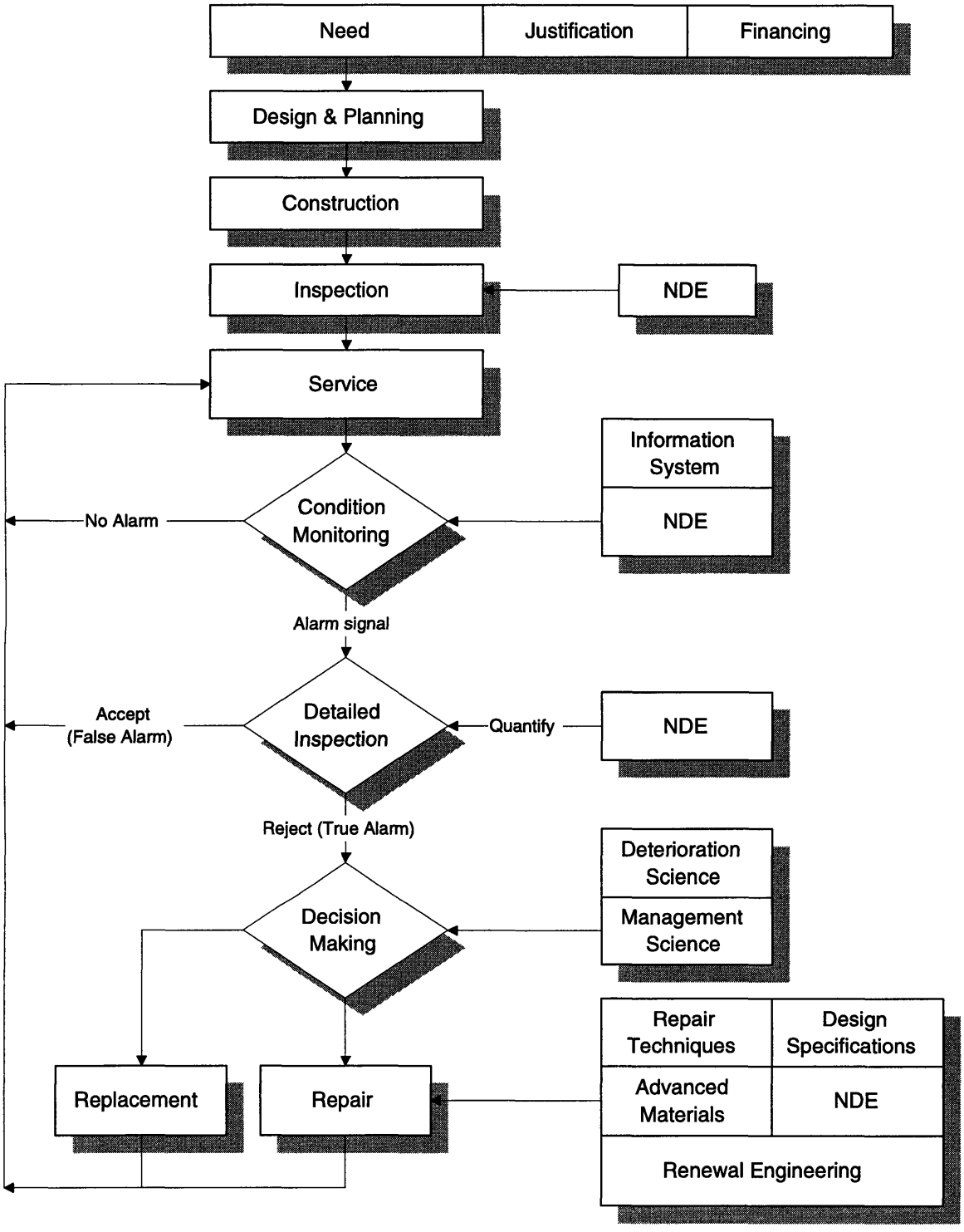

Figure 2.1: The role of NDE in the life-cycle of civil infrastructure [12].

2.3.2 Infrared Thermography

Infrared thermography is currently under development. This method is based on the principle that an air gap is introduced by delamination, which acts as an insulator and restricts heat flow out of the specimen, resulting in variations in surface temperatures. The limitation this method presents is that data interpretation is complicated by varying weather conditions and surface temperature variations related to the surface properties [22, 23].

2.3.3 Radiography

Radiography evaluates defects by measuring the energy attenuation of electromagnetic radiation (x-ray or γ-ray) transmitted through the tested object [13]. The beam of radiation passes through the concrete specimen and exposes a film on the other side, producing an easily interpretable output. This method is hindered, not only by the necessity for access to both sides of the specimen, but also by the danger of these rays to the human body.

2.3.4 Stress Wave Methods

The stress wave method includes techniques which are all based on the elastic wave propagation in solids [2]. When a stress is applied suddenly, the disturbance generated propagate through the solid as stress waves, and in concrete, is dependent on three major components: the density of concrete, Poisson's ratio, and on the dynamic Young's modulus [24].

2.4 Overview of Stress Wave Techniques

A stress wave encompasses a broad group of waves that cause physical distortion to the media in which they are traveling. Naturally occurring stress waves in concrete include compression (P-primary), shear (S-secondary), and surface (R-Rayleigh) waves. Compressive waves are the fastest waves, followed by shear waves, and finally

surface waves [25]. These waves are generated for NDE purposes using a variety of mechanical and electrical sources. The stress wave method includes techniques such as (a) acoustic emission, (b) pulse-velocity, (c) impact-echo, (d) spectral analysis of surface waves (SASW), and (e) ultrasonic techniques.

2.4.1 Acoustic Emission (AE)

The acoustic emission method is used to locate the position of acoustic sources (defects) by monitoring the acoustic waves generated during the formation and development of defects [26], but as it is a passive technique, it is not applicable for detection of existing defects. Berthelot, *et al.* were able to assess the condition of concrete structures by continually monitoring the spectrum of the received signals. This monitoring scheme measures the frequency response of the sensor, and the frequency dependent wave attenuation caused by the concrete specimen [27].

2.4.2 Pulse-Velocity

The pulse-velocity method utilizes the relationship between the quality of concrete and the velocity of an ultrasonic pulse through the material, but significant results have yet to be shown [28].

2.4.3 Impact-Echo

The basic principle of the impact-echo technique is that a stress pulse is introduced into the structure from a hammer, ball drop, or some other impact source, which is monitored by an ultrasonic transducer on the surface. Due to the relative low frequencies present, detection of relatively small cracks will not be detected [28].

2.4.4 Spectral Analysis of Surface Waves (SASW)

SASW is based on the idea that the dispersion of the surface wave is a function of the material properties at different depths, which implies that subsurface characteristics

could be evaluated without direct access. A surface wave is generated, in a manner similar to the impact-echo technique, and the displacement-time function of the surface wave is then measured by two in-line transducers a certain distance away from the source, and analyzed [28].

2.4.5 Ultrasonic Testing (UT)

Ultrasonic methods typically use transmission and reflection of high-frequency waves to detect defects or flaws within or on the surface of a body. The most common approach with civil structures is conventional pulse-echo, as the sound wave is reflected from the body's surfaces, and if present, from its imperfections as well. Ultrasonic testing in the field of NDE is perhaps the most versatile technique for the condition assessment of concrete structures, and forms the basis for the ultrasonic phased array. An in depth review of UT is given in the next chapter.

Chapter 3

Ultrasonic Nondestructive Testing

Ultrasonic testing is primarily based on the piezoelectric effect, which was introduced by the Curie brothers in 1880 [1]. They observed that certain materials, such as quartz, when mechanically stressed developed an electric charge. Upon further investigation, the converse to this situation was also proved to be true. If an electrical pulse was applied to a piezoelectric material, this material would rapidly deform and vibrate, generating ultrasonic energy in the range of 30kHz to over 100 MHz. These discoveries provide the foundation for almost all ultrasound applications.

Ultrasonic testing use these piezoelectric materials in the form of a "transducer". An electrical pulse excites the transducer, which causes ultrasound to be transmitted within the load material (i.e., concrete). These waves interact with inclusion and flaws, and the received ultrasonic energy is converted back to electrical energy via the piezoelectric effect. These signals are processed and displayed on an oscilloscope, where both the amplitude of the received echos, as well as the time-of-flight are used to evaluate the location of possible defects [29, 30]. Figure 3.1 shows the different arrangements for the transmitting and receiving transducers.

3.1 Fundamentals of Ultrasonic Wave Motion

The underlying theme in ultrasonic testing is the measurement of the time (t) needed for a pulse to traverse a distance (h), whereby one of the following velocities of

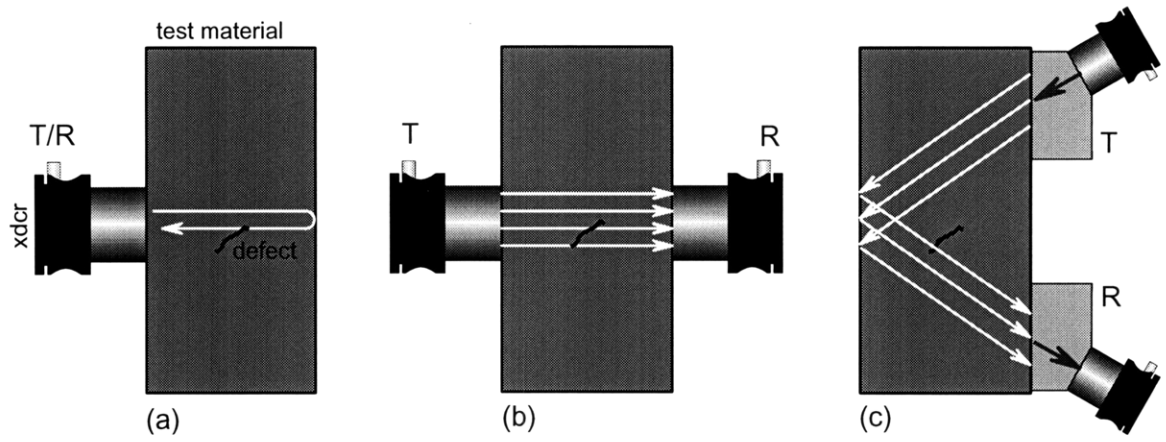

Figure 3.1: Typical transducer arrangements: (a) pulse-echo, (b) through-transmission, and (c) pitch-catch.

propagation can be determined: a compressional or longitudinal wave (c_L), a shear or transverse wave (c_T), or a Rayleigh or surface wave (c_S).

$$c = \frac{h}{t} \, .$$

These velocities can also be expressed by the density of the material (ρ), the modulus of elasticity (E) or shear modulus (G), and Poisson's ration (ν) for the one-dimensional strain case:

$$c_L = \sqrt{\frac{E}{\rho} \cdot \frac{1-\nu}{(1+\nu)(1-2\nu)}} \, ,$$

$$c_T = \sqrt{\frac{E}{\rho} \cdot \frac{1}{2(1+\nu)}} = \sqrt{\frac{G}{\rho}} \, ,$$

$$c_S = \frac{0.87+1.12\nu}{1+\nu} \cdot \sqrt{\frac{E}{\rho} \cdot \frac{1}{2(1+\nu)}} \, .$$

Longitudinal (compressive, dilatational) waves are bulk waves, where the direction of particle motion coincides with the direction of wave propagation. Transverse (shear, distortional) waves are also bulk waves, but the direction of particle motion is transverse to the direction of propagation. Rayleigh (surface) waves propagate along the surface of a solid and decay exponentially with depth from the surface, with particle motion parallel to the surface. Typically longitudinal waves are the most prominent, especially at incident angles normal to an interface. Table 3.1 contains values for the various wavespeeds and other parameters for various materials.

Material	Density, ρ (kg/m^3)	c_T (m/s)	c_L (m/s)	E (MPa)	G (MPa)	ν
Concrete	2300	2560	4430	36680	15000	0.26
Concrete	2460	2830	4960	48270	19800	0.27
Steel	7800	3230	5850	204000	85500	0.28
Aluminum	2700	3080	6260	71000	26400	0.34
Perspex	1180	1430	2730	5350	2430	0.35

Table 3.1: Material properties.

3.2 Transmission and Reflection Coefficients

3.2.1 Acoustic Impedance

A relationship can be established between the particle velocity (v) and the propagation velocity as follows:

$$\frac{\sigma}{v} = \rho c \,, \tag{3.1}$$

with σ as the wave stress and ρ as the density of the material. The term "ρc" is the acoustic impedance (Z) of the material, which varies from one type of material to another. The importance of the acoustic impedance will be explained shortly. Table 3.2 gives approximate values of the acoustic impedance for the components of

concrete [31], while Table 3.3 gives approximate values for the acoustic impedance for various materials [2].

Component	Z $g\ cm^{-2}\ s^{-1}$
Air	0.431
Water	1.5 x 10^5
Granite	7.5 x 10^5
Quartzite	14.5 x 10^5
Steel	39 x 10^5
Cement paste	4.0 x 10^5

Table 3.2: Acoustic impedances for the components of concrete.

Material	Density (Kg/m^3)	Velocity: c_L (m/s)	Z $g/cm^2s \times\ 10^5$
Air	1.205	343	0.413 $\times 10^5$
Concrete	2300	3000-4500	6.9-10.4
Granite	2750	5500-6100	15.1-16.8
Limestone	2690	2800-7000	7.5-18.8
Marble	2650	3700-6900	9.8-18.3
Quartzite	2620	5600-6100	14.7-16.0
Soils	1400-2150	200-2000	0.28-4.3
Steel	7850	5940	46.6
Water	1000	1480	1.48

Table 3.3: Acoustic impedances of various materials.

3.2.2 Normal Incident Waves

If an interface between different materials exists, some of the acoustic energy will continue to transmit through, while some will be reflected back. The product of the transmission coefficient (T) or the reflection coefficient (R), with the magnitude of the original pulse, gives the value of the transmitted and reflected pulses.

These coefficients, for normal incidents, are based on the ratio of acoustic impedances of the two materials (Z_1 and Z_2):

$$\beta = \frac{Z_1}{Z_2} = \frac{\rho_1 c_1}{\rho_2 c_2} \,. \tag{3.2}$$

Table 3.4 provides the reflection and transmission coefficients in terms of displacement, stress and energy.

Displacement	***Stress***	***Energy***
$R = \frac{1-\beta}{1+\beta}$	$R_\sigma = -R = \frac{\beta-1}{\beta+1}$	$R_E = R^2 = \left(\frac{1-\beta}{1+\beta}\right)^2$
$T = \frac{2}{1+\beta}$	$T_\sigma = \beta T = \frac{2\beta}{1+\beta}$	$T_E = \beta T^2 = \frac{4\beta}{(1+\beta)^2}$

Table 3.4: Reflection and transmission coefficients at normal incidence.

The coefficient of reflection at a concrete-air interface is high because of the comparatively much greater acoustic impedance of concrete with that of air. The reflection coefficient of a concrete-water interface is about .6 to .8. These account for the strong reflections of pulses as they interact with water or air filled voids and cracks in concrete. According to Jones [31], 10 to 24% of the amplitude of the original pulse passes through a thin water filled crack in concrete, and only a negligible amount passes through an air filled gap. However, a pulse can pass on either side of a crack by defraction, making for a complex situation indeed.

3.2.3 Oblique Incident Waves

In some cases, the incident angle traveling at a wavespeed c_1 may strike an interface at an oblique angle θ_i. The problems associated are three-fold: attaining the angle(s) of the refracted pulse (θ_r), the change in wavespeed due to possible mode conversion, and the transmit/reflection coefficients.

A fundamental equation to evaluate the first case is Snell's Law:

$$\frac{\sin\theta_i}{c_1} = \frac{\sin\theta_r}{c_2} \ , \tag{3.3}$$

where c_2 is the wavespeed in the second medium. Solving for θ_r, the refracted angle can be attained:

$$\theta_r = \sin^{-1}\left(\frac{c_2}{c_1}\sin\theta_i\right) \ . \tag{3.4}$$

To answer the second, observe that the refracted angle cannot exceed 90°, as a limit for θ_i will be introduced depending on the wavespeeds of the respective media. This critical angle can be attained as follows:

$$\theta_{cr} = \sin^{-1}\left(\frac{c_1}{c_2}\right) \ . \tag{3.5}$$

With an angle of incidence oblique to the interface, both longitudinal and transverse waves will form, and as this angle is increased, transverse and surface waves will remain, and then eventually only surface waves. With Concrete, an angle of 45^o will generate the strongest transverse wave [31]. Figure 3.2 demonstrates some various scenarios typical to NDE.

The reflection and transmission coefficients depend on various boundary conditions brought forth by the type of interface. These are too long to go through here, but can be found in Krautkramer and Krautkramer [1].

3.3 Attenuation Coefficient for Concrete

The natural frequency of a harmonic wave can be computed as follows:

$$f = \frac{c}{\lambda} \ , \tag{3.6}$$

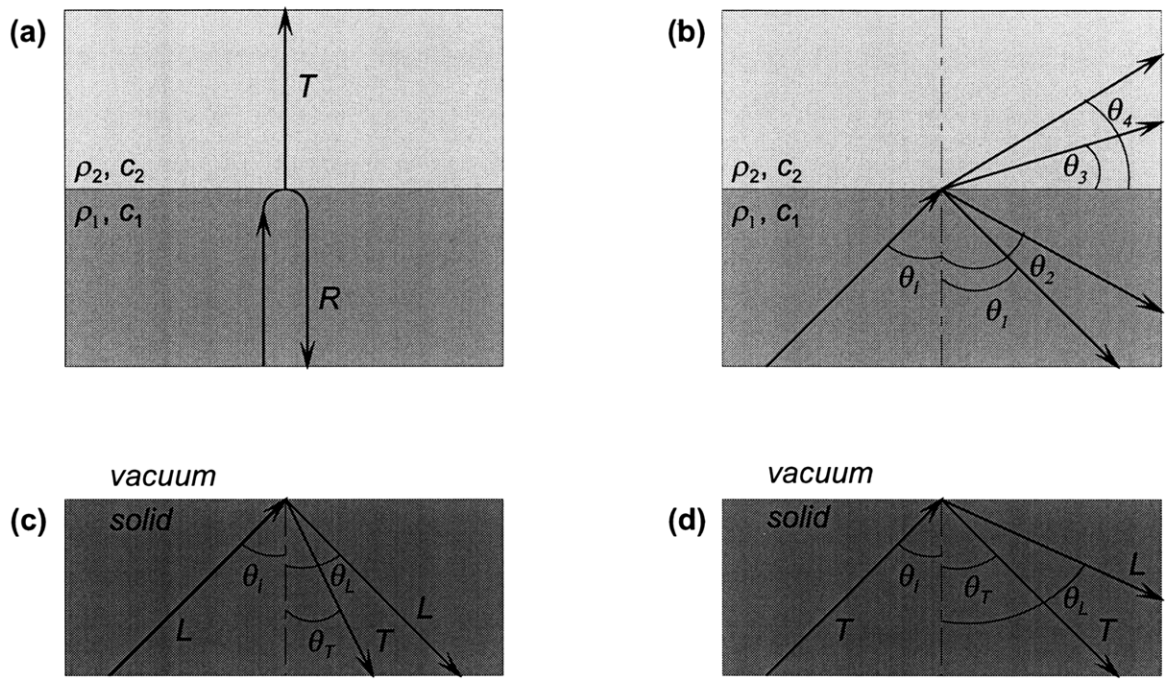

Figure 3.2: Wave reflection, transmission and refraction: (a) normal incidence, (b) oblique incidence between two media, (c) obliquely-incident longitudinal wave at a free surface, and (d) obliquely-incident transverse wave at a free surface.

where c is the velocity and λ is the length of the ultrasonic wave. Typically c_L (the longitudinal velocity) falls within 3500 to 5000 m/s in concrete. As an example, consider f=100 kHz, then λ will range from 45 to 50 mm. λ will be half that if f=200 kHz. I give these two examples for a specific reason. Although ultrasonic frequencies can range from 20 kHz to well over 100 MHz, the ones used in concrete are in the range of 20 kHz to 250 kHz, or at most 500 kHz. At these frequencies, we obtain adequate directionality and have a good chance of recording the wave fronts.

The limiting factor with concrete is its non homogeneous composition, resulting in strong attenuation with higher frequencies (and correspondingly smaller wavelengths) due to interaction of these waves at the cement paste/aggregate interface. If the wavelength is considerably greater than the dimension of this interface, the interface will be "invisible" to the passing wave. A balance must therefore be achieved in calculating the frequency to be used as to pass without considerable attenuation, yet

still have a wavelength small enough to detect defects within the concrete sample. This can be seen more clearly with the following approximation:

$$u(x,t) = Ae^{\alpha x}e^{j\omega(x/c-t)} , \tag{3.7}$$

where $\alpha = -\omega^2 D/2\rho c^3$ is the attenuation coefficient, used as a measure of attenuation for a given material and frequency, and D defined as the damping coefficient of the material. This represents a harmonic equation for the particle displacement as compared to time. It is important to note that as ω (the angular frequency) increases, the amplitude will decrease. For typical frequencies (between 100 to 200 kHz), $\alpha = 10dB/m$ (decibels per meter), or $1Np/m$ (Nepers per meter), for concrete. [31].

3.4 Limitations of Current Ultrasonic Techniques for Concrete

High-frequency ultrasonic pulse-echo systems have been successful with homogeneous materials, notably with metals and composites, but with the heterogeneous nature of concrete, frequencies above several hundred kilohertz are not practical because of the attenuation previously mentioned. Low frequency ultrasound must therefore be used, which reduces the resolution of the transducer in detecting inclusions and flaws.

Another important aspect is the small aperture size that is present with conventional methods, which utilize a static, single element transducer with limited capabilities. Aside from physically scanning at small increments, the only other alternative is to place the transducer on a mobile vehicle, such the roller transducer carriage developed at Northwestern University to detect crack depth [30].

3.5 Summary of NDT of Concrete

Concrete structures are a major part of CIS, many of which are aging and exhibiting various stages of decay and sometimes failure. There is a growing demand for the condition assessment of concrete as the degradation of CIS is being gradually recognized. Unfortunately, there is no effective technology to perform this task today. People have been using techniques such as radar, infrared thermography, radiography, impact-echo, and ultrasound for NDE of concrete. However, these techniques are hindered by low penetration capacity (for concrete thickness less than 0.6 meters), surface conditions, the need for access on both sides of the specimen, the inability to detect relatively small cracks, and a limited aperture size respectively [2, 9, 13, 22, 24, 26, 30].

The most employed technique is ultrasound, which offers the best penetration capacity and ability to detect flaws [14]. Current ultrasound techniques can only detect defects directly beneath the sensor, which require mechanical scanning and thus make it both time and labor consuming for testing large-scale concrete structures [28]. To meet the demand of applications in civil engineering, one should be able to penetrate a long distance into concrete (in the order of meters) and at the same time be able to rapidly scan over an area [8, 14]. None of the existing techniques satisfy these requirements, but as we shall see, low frequency ultrasonic phased arrays do.

Chapter 4

Ultrasonic Phased Array Transducers

A low-frequency phased array sensor and supporting system has been developed for assessing health conditions of concrete civil structures in the Nondestructive Evaluation (NDE) Laboratory at the Massachusetts Institute of Technology. The sensor is based on ultrasound technology, which combines multiple transducers into a sensor array and enables electronic steering and focusing of the ultrasound beam. It provides sufficient information about a large sector (in the order of meters) by placing a sensor at one position, eliminating the time consuming physical relocation of the existing single element transducer. The complete solution from this sensor enables real-time two-dimensional imaging of the internal structure of concrete, which is currently a key requirement for concrete assessment in Civil Engineering [14,28]. The sensor can be adapted to attain three-dimensional images in the future.

4.1 Background of Ultrasonic Phased Arrays

Ultrasonic phased array transducers have been around for two decades, mostly in application to many medical specialties. In order to image the moving targets within the body, phased arrays were developed to rapidly move the acoustic beam throughout a region necessary to image the organs of interest [3]. The active role of ultrasonic

phased arrays in the medical fields, such as hyperthermia applications, OB ultrasound, and echocardiography, helped establish their diagnostic importance, and the continued research and development will increase their benefit [3–5, 7, 32, 33]. Recently, phased arrays are also being utilized for the nondestructive evaluation of steel and composite materials [34–36].

4.1.1 Current Phased Array Applications

Medical phased arrays typically have operating frequencies ranging from 1 MHz to over 20 MHz, with an exception for the case of hyperthermia, where a lower frequency (ranging from 0.3 to 1 MHz [37]) focused beam is used in heating tumors. When producing a single focus, the array is able to increase tissue temperature by $12°C$, an in areas where heating would be undesirable, the phased array could take advantage of destructive interference to minimize power deposition at the locations [38]. An example of another medical application is phased arrays being used to create a pressure force used to position detached retinal tissue [39].

The importance of nondestructive testing (NDT) of metals, composites and concrete has issued in an new era for phased array technology. Currently, existing phased arrays have not been very well integrated into these areas, but recent studies [6, 7, 40, 43] do show considerable benefits of their use because of their 2-D and 3-D imaging, high resolution, and intrinsic signal processing capabilities. Most of the current research is aimed at developing arrays for metal and composite testing, which also employ operating frequencies ranging from 1 MHz to well over 20 MHz.

4.1.2 Fundamentals of Phased Arrays Technology

An ultrasonic phased array sensor is composed of multiple array elements, which enable steering and focusing of the ultrasound by triggering different elements at set time intervals. The transmitted waves interact with flaws, and are reflected back to the sensor. The received signal contains information about the flaw, which can be converted to a two-dimensional image through advanced signal processing. Referring

to figure 4.1, the fundamental design parameters for phased arrays are the frequency (f), the element width (a), the center-to-center spacing of the elements (d), the number of elements (N), the total aperture dimension (D), and the elevation dimension (L).

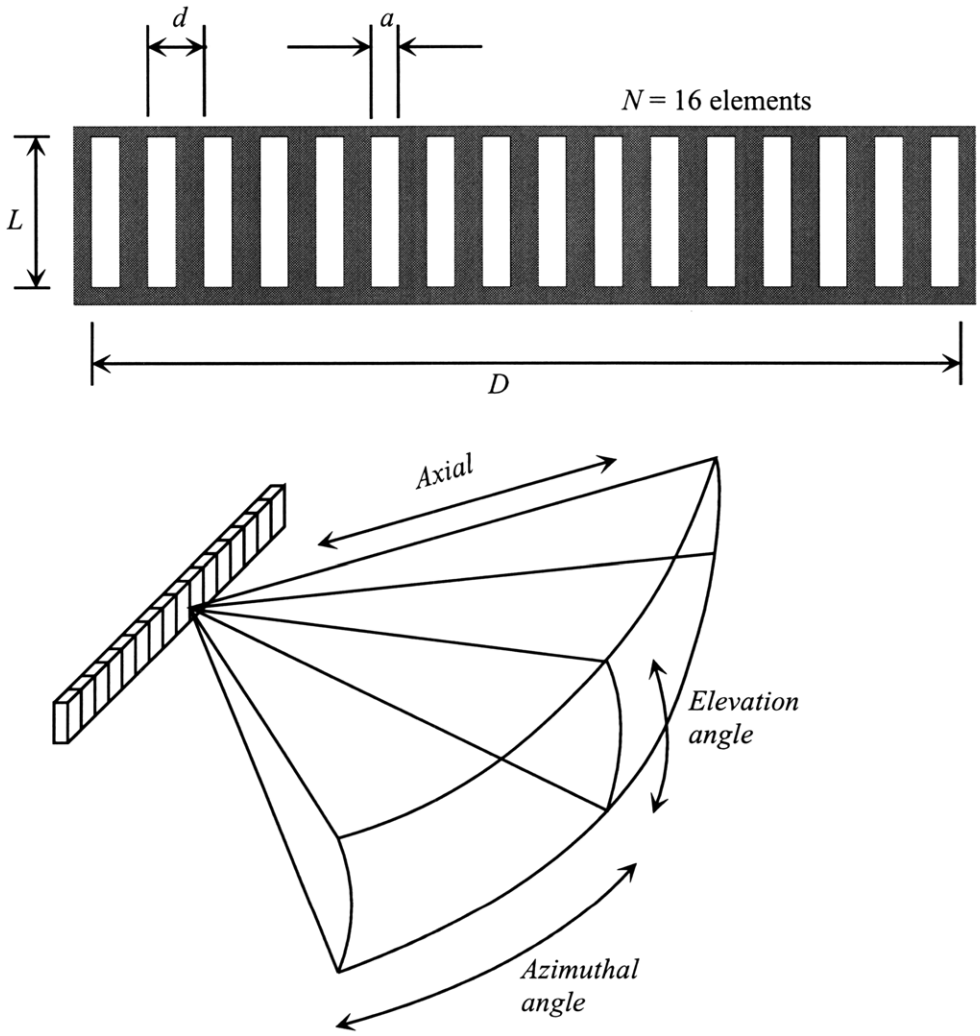

Figure 4.1: Linear array geometry and typical field of view.

Phase steering is accomplished by sequentially pulsing the array elements. The direction of the acoustic beam propagation may be reoriented to any azimuthal angle merely by altering the timing sequence of the excitation pulses [3]. The sound field is represented as Huyghen waves emitted from each element. All the individual wavefronts will add to produce a maximum acoustic intensity along the desired di-

rection [3]. The constant inter-element delay for steering the ultrasonic field can be calculated by [3]:

$$\Delta\tau_0 = \frac{d \sin\theta_s}{c} , \tag{4.1}$$

where $\Delta\tau_0$ is the time delay between adjacent elements, d is the distance between elements, θ_s is the required steering angle, and c is the wave speed in the acoustic medium. Figure 4.2 demonstrates a numerical pressure profile of an array being steered at 30°. This simulation constitutes a trace of the waves propagated by each element, and demonstrates Huyghen's principle of wave interaction needed to steer the acoustic wavefronts.

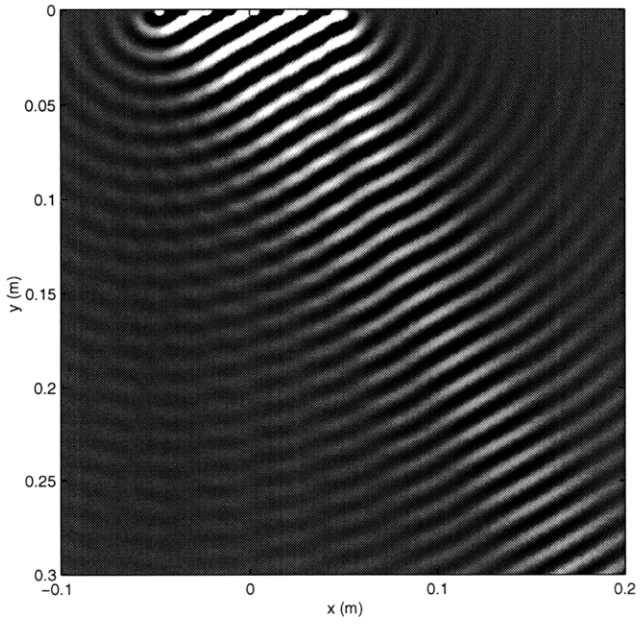

Figure 4.2: Phase steered sound field of an array sensor.

Focusing of the transmitted beam is accomplished by combining a spherical timing relationship with a linear one to produce a beam which is focused at a given range and propagated at a specific azimuth angle [3]. The focusing delays can be calculated

by the following traditional formula: [3, 44]

$$\Delta t_n = \frac{F}{c}\left(1 - \left[1 + \left(\frac{nd}{F}\right)^2 - 2\frac{nd}{F}\sin\theta_s\right]^{1/2}\right) + t_0 \ , \tag{4.2}$$

where Δt_n is the required delay for the nth element ($n = \ldots -2, -1, 0, 1, 2 \ldots$), F is the focal length, and t_0 is a constant to keep the delays positive. Figure 4.3 demonstrates a numerical pressure profile of an array being focused 30° at a focal length of 10 cm.

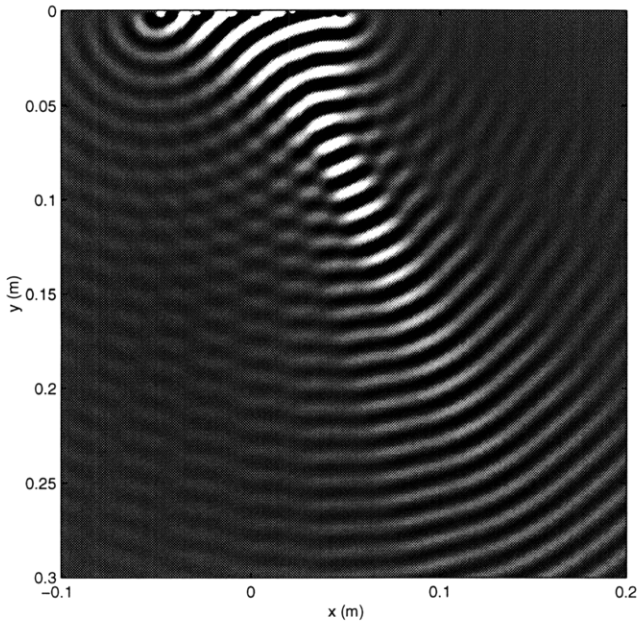

Figure 4.3: Phase focused sound field of an array sensor.

In addition to the primary lobe, other lobes exist due to constructive reinforcement of the Huyghen waves. These additional planes of constant phase are called grating lobes, and can be eliminated by having the inter-element spacing be less than $d_{\max}$, where:

$$d_{\max} = \frac{\lambda}{1 + \sin\left(\theta_s\right)_{\max}} \frac{N-1}{N} \ , \tag{4.3}$$

where $(\theta_s)_{max}$ is the desired maximum operating steering angle of the transducer without producing grating lobes [45]. Care must be taken to eliminate the effects generated, most notably the deceptive echoes that will be created. This can be accomplished by making sure that d is less than approximately $\lambda/2$, for a $(\theta_s)_{max}$ of 90^o.

4.1.3 Other Types of Phased Array Configurations

The linear array sensor produces only a two-dimensional image because the elevation angle is purposely reduced to a minimum by utilizing a large enough elevation distance. Otherwise one would not know where the flaw would be located on the elevation plane. Two-dimensional (matrix) arrays have control of the elevation and azimuthal angles, and allow three-dimensional imaging.

The most sophisticated medical ultrasound scanners now use (Nx1) linear arrays containing over one hundred transducer elements that may be multiplexed and/or electronically steered and focused via phased array techniques [46]. It has become evident that two dimensional (NxM) transducer arrays will be essential in future diagnostic ultrasound equipment to improve clinical image quality. The most immediate application of 2-D phased arrays is to reduce B-scan thickness by dynamic focusing in the elevation plane perpendicular to the azimuth. 2D Arrays can focus and steer in three dimensions, although with greatly increased complexity. While there has been much interest in the development of practical forms of such arrays, none are currently available commercially [47].

There are other array configurations currently under development and/or commercially available. Similar to phased arrays, which allow for an electronically steered/focused beam (sector scanning), linear arrays, which typically would allow groups of elements to be pulsed successively along the array, are also widely utilized [7]. A two-dimensional image is produced in a linear array by sequentially transmitting and receiving the signals down the assembly, producing a rectangular image.

In principle, the design of an array with periodic spacing is simple if the elements are spaced no further than one-half wavelength apart ($\lambda/2$), a requirement to prevent

unwanted grating lobes [3]. A larger overall dimension ,"D", of an array signifies a much narrower main lobe width. This, and the fact that we have a spacing limitation greatly increases the number of elements used. Arrays, with fewer elements than required by the $\lambda/2$ condition, are often called "sparse arrays" [48]. A sparse array with the same effective aperture element spacing and width (although not necessarily the same aperture shape) as a dense 128-element array could be designed using only 16 transmit and 16 receiving elements [48]. Additional elements must be added to the array to maintain the desired radiation pattern within the near field [48].

Alternate approaches to reduce the number of elements in a linear phased array have been proposed [3, 49], which utilize variably spaced elements. Annular arrays, which are comprised of element in a ″ring″ formation, have excellent focusing capabilities, but cannot be steered [40].

4.2 Fundamentals of Phased Array Imaging

The reception of ultrasound by a phased array is the inverse of transmission. Signals from each element must be delayed relative to one another before combined to realize a steered or focused directivity [6]. The absolute value of collected waveform amplitudes are plotted at their corresponding θ_s and respective radial depths, calculated by $(\Delta T/2)c$, and an image is formed. Only the part of the waveform which appears beyond the near field is imaged when steering is employed, and only the part that falls within the focusing range is imaged when focusing.

There are numerous image processing and acquisition techniques that are employed to optimize the image quality. These will not be discussed, but can be found in many publications [3, 4, 6, 38, 41–43, 50].

4.3 Fabrication Procedure for the Array Transducer

Transducers are perhaps the most vital component in the ultrasonic testing and imaging systems. Their function is to convert applied voltage to ultrasonic pressure, and generate electrical signals from the received waves. A well designed transducer will do this with high fidelity, with good conversion efficiency, little introduction of noise or other artifacts, and will provide control over the system resolution and its spatial variation [50].

4.3.1 Conventional Single Element Construction

Piezoelectric element

The phased array elements are usually cut or are etched to the required dimension from a single piezoelectric plate of lead zirconate titinate (PZT), of which the thickness determines the operating frequency of the transducer. Another material frequently used is polyvinylidene difluoride (PVDF), a polymer which can exhibit piezoelectric properties [7, 44]. Silver electrodes are deposited on the front and back faces, and the element is permanently polarized across its thickness. The speed of sound in PZT is approximately 4000 m/s, which gives a fundamental resonance ($\lambda/2$) at frequency f and thickness T related by: [50]

$$T(mm) = \frac{2}{f}\,(\text{MHz}) \quad . \tag{4.4}$$

For example, at 200 kHz, $T \approx 10\ mm$.

Mason and KLM model

The well-known one-dimensional Mason model [51] was originally used to derive the electrical input impedance of an acoustic transducer, and other parameters of interest

by introducing an equivalent circuit. An improvement of the Mason Model is the transition line model of Krimholtz, Leedom, and Matthaei (KLM Model) [52].

Through these models, the required acoustic and electrical impedances can be solved, and the shape of the pulse derived. The evaluation of parameters such as the required backing, matching layer, and electronic input can all attributed to the Mason and KLM models [53–57].

Backing medium

The main problem with transducers is the large mismatch between the piezoelectric ceramic (PZT) and the load (concrete). Consequently, most of the acoustic energy is reflected back and forth between the rear and front faces of the ceramic. The acoustic pulse transmitted into the load will therefore be long and the axial resolution poor [54].

The method commonly used to dampen these oscillations is to attach an absorbing material to the rear face of the piezoelectric ceramic. If the acoustic impedance of the absorbing material is close to that of the ceramic, the length of the pulse transmitted and, after reflection, received will be short. However since most of the energy is absorbed into this backing, the transducer sensitivity is low. A compromise is therefore usually made by using a backing with a lower acoustical impedance [54].

The most commonly used backing consists of epoxy or araldite resin mixed with a high ultrasonic absorption material, such as tungsten powder, to increase the density and therefore the acoustic impedance [57]. Tungsten/epoxy densities in the region of 13.5 g/cm^3 are required to match acoustically with PZT, but that mixture is very difficult to reach. Typically, tungsten powder in an epoxy resin or araldite mixture produce a $Z_B \approx Z_C/2$, where Z_C is the impedance of the ceramic (i.e, PZT) and Z_B is the impedance of the backing [50, 55].

To evaluate the optimum backing impedance, the following relation can used to evaluate the amount of trapped energy: [58]

$$W = \left(\frac{Z_C - Z_L}{Z_C + Z_L}\right)\left(\frac{Z_C - Z_B}{Z_C + Z_B}\right) , \tag{4.5}$$

where W represents the square root of the trapped energy after one oscillation, and Z_L is the impedance of the load (i.e., concrete). A high value for W (greater than 0.75) leads to excessive ringing, while low values (less than 0.1) result in very short transducer response. An acceptable value of W for ultrasonic testing is 0.3. Therefore, the required backing impedance can be calculated as follows:

$$Z_B = Z_C\left[1 - 0.3\left(\frac{Z_C + Z_L}{Z_C - Z_L}\right)\right]\left[1 + 0.3\left(\frac{Z_C + Z_L}{Z_C - Z_L}\right)\right]^{-1} . \tag{4.6}$$

Matching layer

The acoustic impedance of PZT is approximately 14 times that of water, while that of $PVDF$ is only 1.5 times that of water [50]. Referring to table 3.2, an approximate value for the acoustic impedance of concrete is 3 to 6 times that of water. The acoustic impedance mismatch with PZT will hinder the energy transfer into concrete. $PVDF$ would be better suited, but suffers from lower sensitivity due to poorer conversion efficiency [50].

Energy transfer when using PZT can be improved by providing one, or more, front matching layer(s) to the base of the piezoelectric material. DeSilets (1978) is credited for the derivations put forth for the required acoustic impedance and thickness for matching layers [53]. The required impedance for a single matching layer can be calculated as follows:

$$Z_a = \sqrt{Z_C Z_L} , \tag{4.7}$$

where Z_a is acoustic impedance of the matching layer, Z_L is the impedance of the load material, and Z_C is the impedance of the ceramic material.

Multiple matching layers may sometimes be required if the acoustic mismatch is significant. If two matching layers are required, their impedances can be calculated as follows:

$$\begin{aligned} Z_a &= Z_L^{3/7} Z_C^{4/7} \ , \\ Z_b &= Z_L^{6/7} Z_C^{1/7} \ , \end{aligned} \tag{4.8}$$

where Z_a is the impedance for the matching layer in contact with the ceramic, and Z_b is the impedance for the matching layer in contact with the load material.

The ideal thickness (t_a) for the matching layers to maximize energy transfer can be calculated as follows:

$$t_a = \frac{\lambda}{4} = \frac{c_a}{4f_\circ} \ , \tag{4.9}$$

where λ is the wavelength within the matching layer, c_a is the wavespeed in the matching layer, and $f_\circ$ is the center frequency of the ceramic material.

An excellent experimental study based on the Mason model can be found in Persson and Hertz [54]. They predicted the transducer response with theoretical calculations, and experimentally verified the effects of applying various assemblies of matching layers between the ceramic and load. They were able to optimize matching layer requirements to develop a transducer with good sensitivity and short pulses.

4.3.2 Phased Array Sensor Fabrication

A phased array is a multi-element transducer, whereby each element observes the required parameters put forth in the previous section. Referring to figure 4.4, the elements were elastically isolated by cutting fully through the ceramic, into the backing. If partial or no cutting (monolithic) assembly is used, the effective excitation width of each element would be much greater than the physical dimension due to acoustic crosstalk [6]. Inter-element crosstalk limits the angular response of transducer arrays and hence the ability to steer to large angles [46].

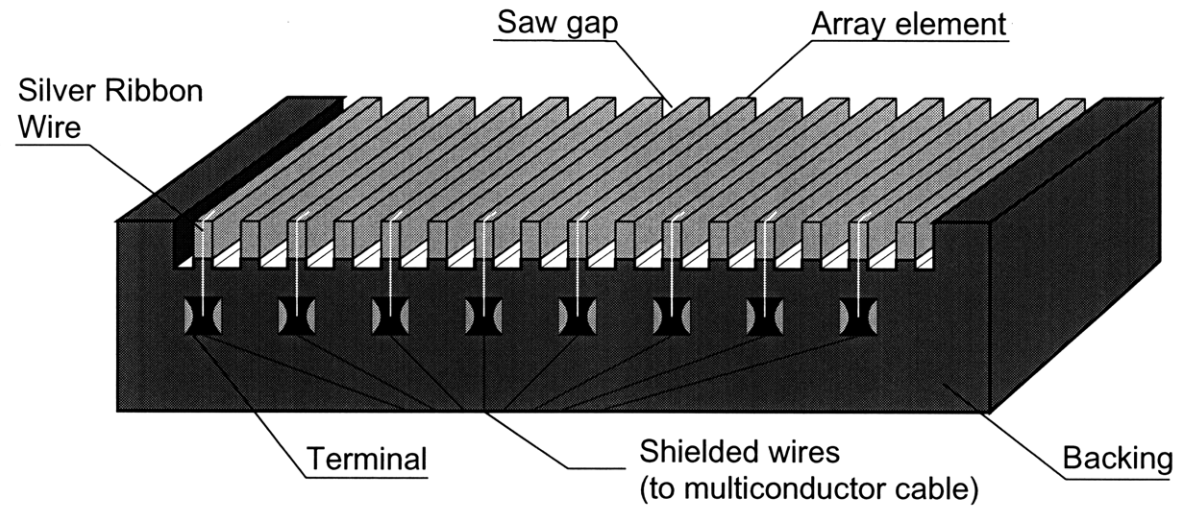

Figure 4.4: Slotted transducer array design.

Piezoelectric element

A ceramic piezoelectric material, lead zirconate titanate (PZT), was utilized. With a thickness of 0.75 mm, the center frequency was approximately 270 kHz. The acoustic impedance (Z_C) was measured to be approximately 34.5 MRa ($=34.5\times10^5 g/cm^2 s$), with a wavespeed of 4700 m/s. It should be noted that with the combination of backing, ceramic, and load, the frequency was reduced to 140 kHz in concrete and 170 kHz in mortar. Figure 4.5 shows the pulses attained through mortar and concrete, with their respective Fourier transforms.

Backing medium

The acoustic impedance of concrete was measured to be approximately 1 MRa, with a wavespeed measured to be approximately 3500 m/s, as shown in figure 4.6. Therefore, the required backing impedance (Z_B) was calculated using eq. (4.6) to be 18 MRa. A mixture of tungsten powder and epoxy resin was utilized for the backing material, at a tungsten/epoxy (T/E) weight ratio of 3:1. This resulted in a Z_B of 6 MRa. Obtaining a higher T/E resulted in a mixture that was too viscous, and too costly. This resulted in a W of 0.66, which results in some ring down effect.

Matching layer

Three possible configuration were tested with regard to the matching layers. For most of the experimental results (i.e., directivities), no matching layer was needed for the type of data required, although a protective layer of Kapton tape was applied. For future imaging, a single and double matching layer scheme will be attempted.

For the single matching layer, a Z_a of 6 MRa is required, which was attained using a T/E weight ratio of 3:1. The wavespeed in the layer (c_a) was measured to be approximately 1600 m/s. The needed thickness (t_a) of the layer was calculated to be approximately 1.5 mm.

For the double matching layer, the impedances of the first and second layer were calculated, with $Z_a \approx 7.5$ and $Z_b \approx 1.7$ MRa. A T/E ratio of 3:1 was used for the first layer ($Z_a \approx 6$ MRa) and a RTV silicone adhesive was used for the second layer ($Z_b \approx 1.2$ MRa). The wavespeed in RTV is approximately 990 m/s. The thickness of the first layer was approximately 1.5 mm and the thickness of the second layer was approximately 1 mm.

Contact transducers typically use a coupling gel to properly transmit the energy to the load material. Since the surface of *in situ* concrete is relatively coarse, applying this gel is critical. A silicone layer allows for dry coupling to the load material, as its elasticity overcomes many of the surface irregularities. Although RTV is considered very attenuative for most ultrasonic applications, the low frequencies inherent for concrete testing remove this deleterious effect.

Dimensions

Two types of arrays were fabricated. As will be shown, the array needed to acquire directivity plots required a lateral dimension (L) of 1.6 cm to fit in the testing assembly. It will be shown that this will not deleteriously affect the results. For imaging, a sensor with a proper L of approximately 11.6 cm was fabricated. This is needed for the wavefront to behave as a line source in the lateral dimension.

Figure 4.7 shows the array that was fabricated, and used to attain the directivity results. 32 elements were cut, resulting in an inter-element spacing (d) of 0.727'cm, and an element width (a) of 0.52 cm. The experiments were made using every other element, which resulted in a d of 1.454 cm. With a frequency of 140 kHz measured for concrete, the spacing resulted in a d of 0.582λ. With a frequency of 170 kHz measured for mortar, the spacing resulted in a d of 0.7λ. (Remember that the optimum spacing to avoid grating lobes was 0.5λ). The overall dimension D was 23.3 cm.

Shielded wire

An individually shielded, 22 gauge wire was used to connect to each element. As shown in figure 4.4, the wire was connected to terminals affixed to the side of the sensor, which in turn were connected (via a silver ribbon wire) to the electrodes of the PZT. The ground wire was connected to a copper foil that had been bonded with silver-filled epoxy across the entire plate prior to the backing installation. Individual shielding is a key, and often overlooked, aspect of sensor design. Without this, electrical crosstalk can greatly reduce the effectiveness of the sensor.

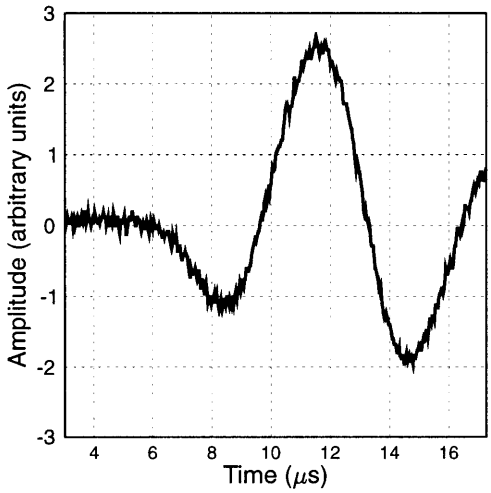

(a) Single element pulse in concrete

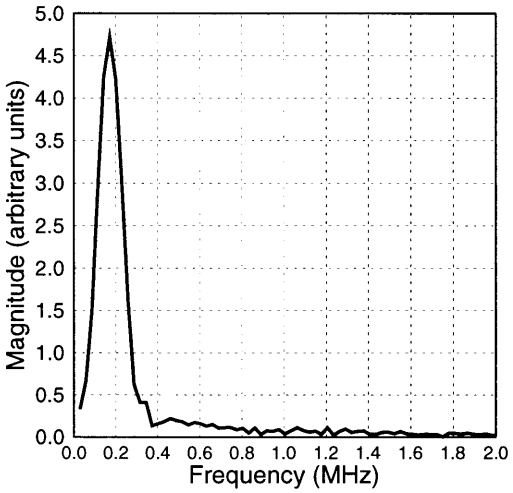

(b) Fast fourier transform: f=170kHz

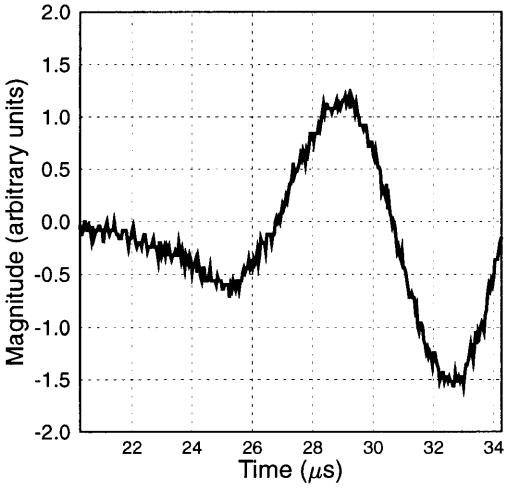

(c) Single element pulse in mortar

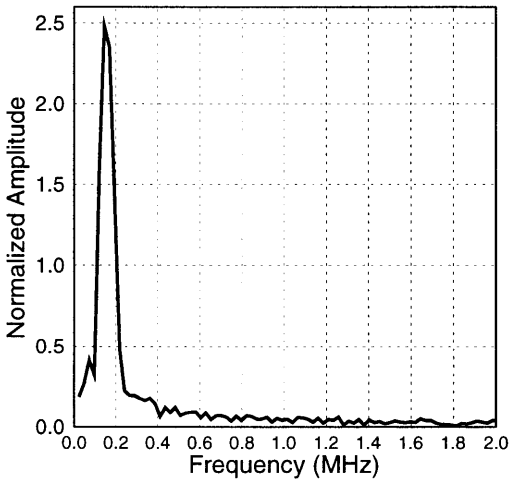

(d) Fast fourier transform: f=140kHz

Figure 4.5: Single element pulse for mortar (f=170kHz, d=0.7λ, and c=3650m/s) and concrete (f=140kHz, d=0.58λ, and c=3500m/s), with their corresponding fast Fourier transforms.

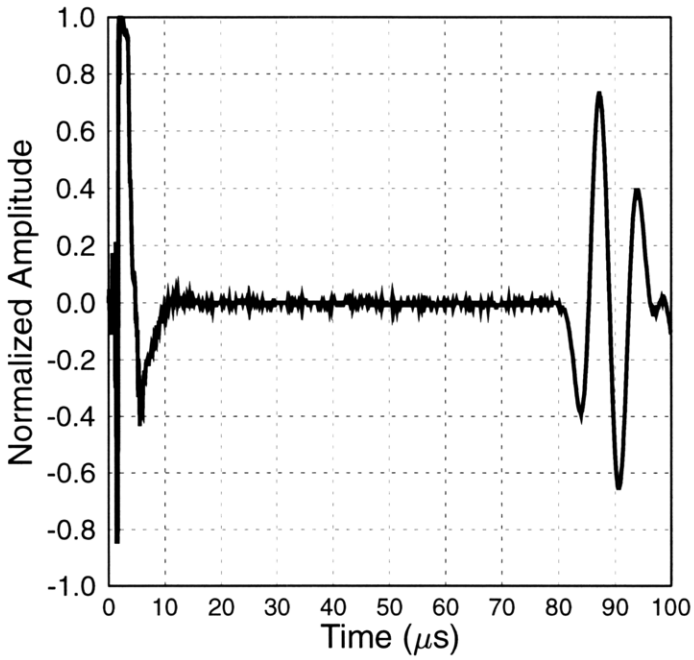

Figure 4.6: Single element pulse acquired through the concrete wheel to ascertain the wavespeed of the material (R=30.48cm, ΔT=87.2μs, and c=3500m/s).

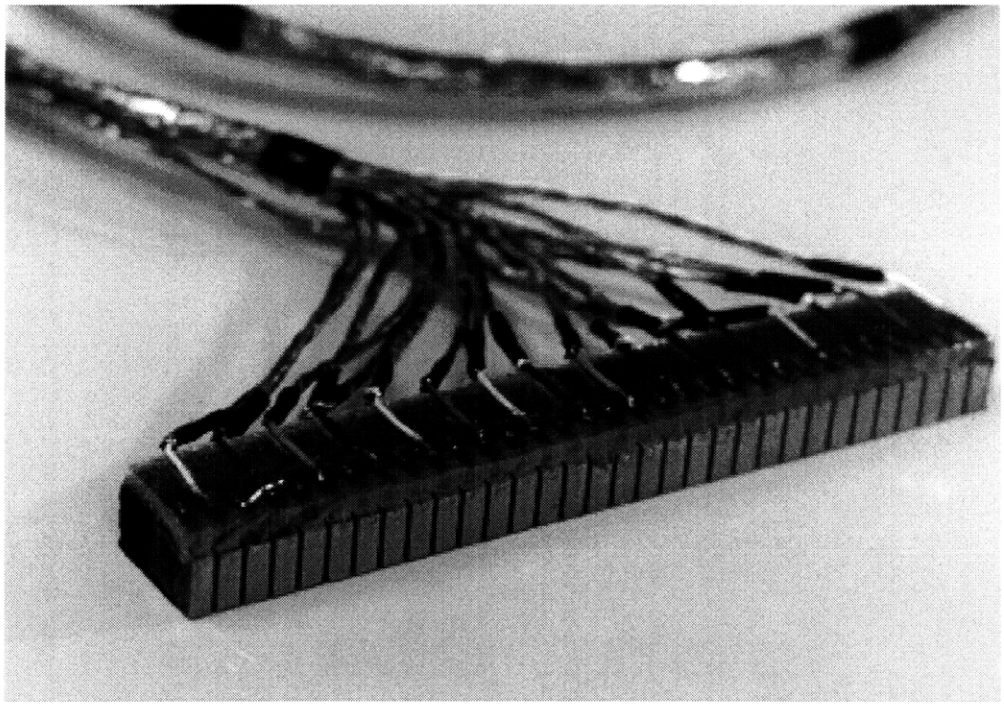

Figure 4.7: Phased array sensor: N=32, d=7.27mm, a=5.2mm, and D=22.3cm.

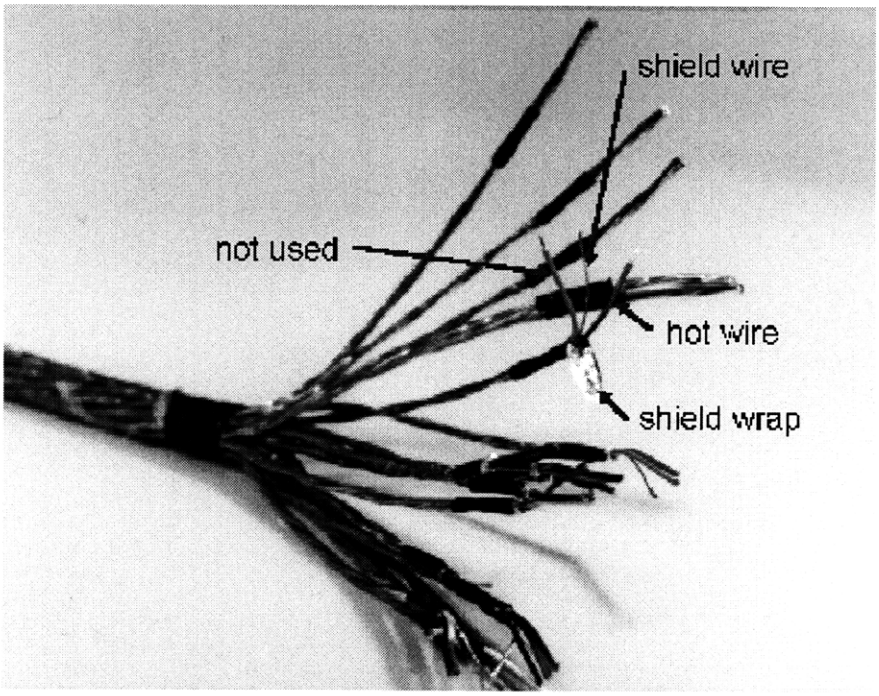

Figure 4.8: Shielded cable.

Chapter 5

Modeling of Focusing Pressure Distribution

One of the fundamental properties of linear phased arrays is the ability to focus the propagating waves at a specific point within the load material by inducing a parabolic time delay. Focusing is a critical tool used to obtain adequate directivities in the near field of an array. Since the frequencies needed for concrete assessment are in the 100 to 200 kHz range, the overall aperture length is quite large. This creates a significant near field zone, and focusing must be employed.

The required focusing delay has been modified from the current formulation to incorporate either an odd or an even number of elements. A brief procedure leading to the derivation of the pressure distribution for beam focusing is attempted, which gives rise to an unclosed form. Consequently, a numerical method is desirable for the analysis of beam focusing. Using this approach, beam directivity and image pressure distributions were developed to determine the behavior of focusing as compared to steering. This showed a benefit of focusing over steering within the near field of the array, and that the directivity of focusing converges to that of steering in the far field.

5.1 Analytical Pressure Distribution for Focusing

The analytical pressure distribution regarding beam steering was previously derived [59]. This analytical model is crucial in resolving the key parameters for these arrays. One such parameter is the effect the number of elements (N) have on the directivity while steering. As the number of elements increases, the main lobe of the directivity also sharpens, which allows for better imaging. This result introduces some drawbacks which can be overcome by focusing the ultrasonic field, as we shall see.

Von Ramm and Smith [3] stated that little image improvement will result if the focal point is beyond the transition range of the array denoted by:

$$Z_{TR} = \frac{D^2}{4\lambda} , \tag{5.1}$$

where D is the overall dimension of the array, and λ is the wavelength in the acoustic medium. This transition range separates the near field from the far field of the array. If targets within the near field of the array aperture are imaged, that is, at distances less than Z_{TR}, then focusing may be employed to increase the system resolution [3].

How focusing improves the resolution over steering has not been explained. Understanding the behavior within this transition zone is very critical. As can be seen by eq. (5.1), as the overall dimension of the array increases, this transition zone will also increase by a factor squared. Since the inter-element spacing should be less than approximately half the wavelength to avoid grating lobes [59], the number of elements affects the overall dimension of the array. If the number of elements doubles while fixing the inter-element spacing, then the transition zone quadruples.

The aperture width for phased arrays used to assess concrete is much larger than that of any existing arrays, primarily due to the low frequencies utilized. This creates an expanded near field zone, and focusing becomes a critical issue. A significant amount of effort was made to better understand the effects of wave interaction while focusing, which included extensive analytical and numerical models, and experimental verification [60].

The analytical solution to establish the pressure distribution for focusing was attempted, resulting in an unclosed form [60]. Therefore, the numerical model was developed to simulate the pressure field for steering or focusing within the transition zone (near field), and beyond (far field). This model was used to demonstrate how focusing improves resolution in the near field, and how focusing behavior converges to that of steering in the far field. The latter point is also proven analytically.

5.1.1 Derivation of Focusing Formula

Equation (4.2) has two limitations as it stands. First, this focusing formulation is only valid for an odd number of elements. Invariably, most phased arrays have an even number of elements. Second, the required constant t_0, to keep the delays positive, is very clumsy to utilize. A formulation to handle both even and odd numbers of elements was derived. Referring to figure 5.1, the following geometric relationship can be attained:

$$(F\cos\theta_s)^2 + \left[F\sin\theta_s - \left(nd - \frac{N-1}{2}d\right)\right]^2 = \left[F - (t_n - t_0)\,c\right]^2 \ , \qquad (5.2)$$

for the element $n = 0, 1, \cdots, N-1$, where N is the total number of elements. Note that in figure 5.1, the first element ($n = 0$) starts at the right hand side. Solving for t_n, we obtain:

$$t_n = \frac{F}{c}\left\{1 - \left[1 + \left(\frac{d}{F}\left(n - \frac{N-1}{2}\right)\right)^2 - 2\sin\theta_s\frac{d}{F}\left(n - \frac{N-1}{2}\right)\right]^{1/2}\right\} + t_0 \ . \qquad (5.3)$$

The constant t_0 can be determined by substituting the boundary condition ($t_n = 0$ for $n = 0$) into eq. (5.3), which results in:

$$t_0 = -\frac{F}{c}\left\{1 - \left[1 + \left(\frac{d}{F}\left(-\frac{N-1}{2}\right)\right)^2 - 2\sin\theta_s\frac{d}{F}\left(-\frac{N-1}{2}\right)\right]^{1/2}\right\} \ . \qquad (5.4)$$

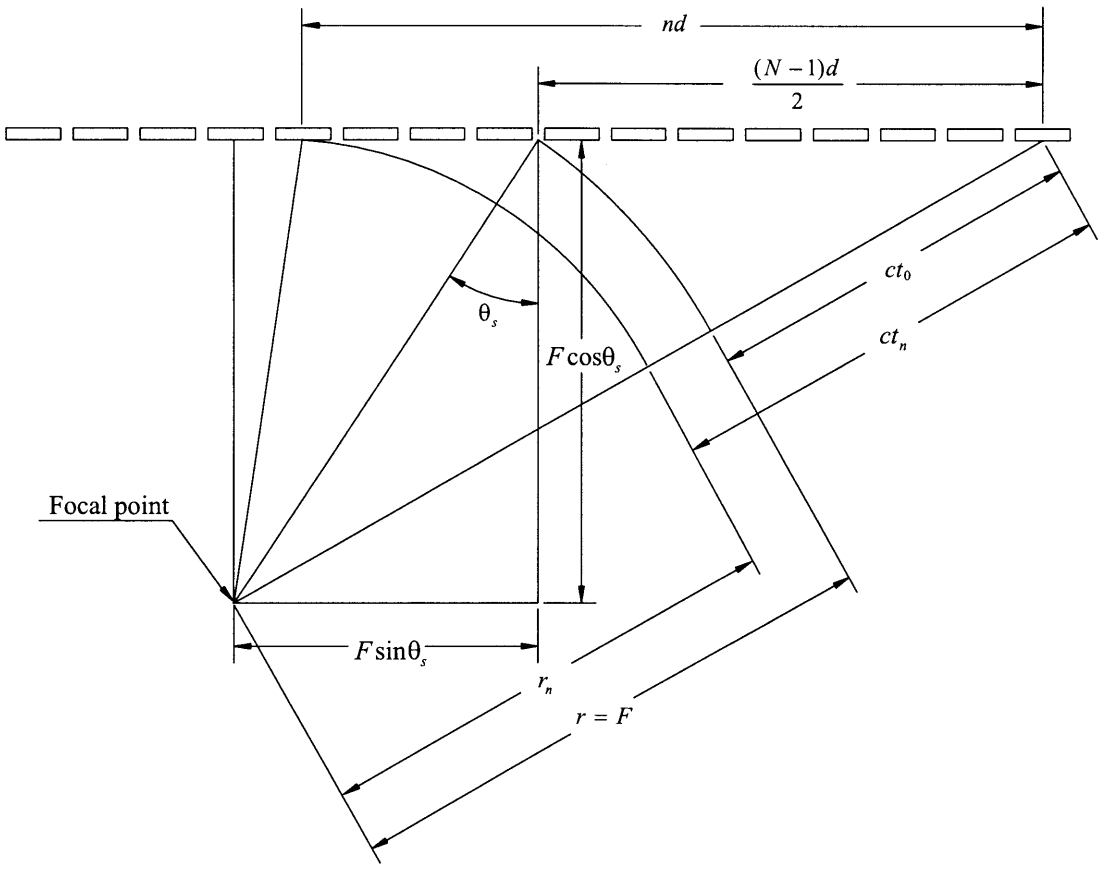

Figure 5.1: Geometry of linear phased array needed for even-numbered focusing formula derivation.

Substituting eq. (5.3) into eq. (5.4), we obtain:

$$t_n = \frac{F}{c}\left\{1 - \left[1 + \left(\frac{d}{F}\left(n - \frac{N-1}{2}\right)\right)^2 - \frac{2d}{F}\left(n - \frac{N-1}{2}\right)\sin\theta_s\right]^{1/2}\right\} - \frac{F}{c}\left\{1 - \left[1 + \left(\frac{d}{F}\left(-\frac{N-1}{2}\right)\right)^2 - \frac{2d}{F}\left(-\frac{N-1}{2}\right)\sin\theta_s\right]^{1/2}\right\} . \quad (5.5)$$

Simplifying, a general solution for the required element focusing delays can be written as:

$$t_n = \frac{F}{c}\left\{\left[1+\left(\frac{\bar{N}d}{F}\right)^2+\frac{2\bar{N}d}{F}\sin\theta_s\right]^{1/2}-\left[1+\left(\frac{(n-\bar{N})\,d}{F}\right)^2-\frac{2\,(n-\bar{N})\,d}{F}\sin\theta_s\right]^{1/2}\right\}, \tag{5.6}$$

where $\bar{N}=(N-1)/2$, t_n is the required delay for element n where $n=0,1,\cdots,N-1$, d is the center-to-center spacing between elements, F is the focal length from the center of the array, θ_s is the steering angle from the center of array, N is the total number of elements (even or odd), and c is the wavespeed. This generalized focusing time delay formula is valid for any number of array elements (even or odd). Furthermore, by eliminating the constant t_0, the formula guarantees positive time delays which do not have to be larger than necessary.

5.1.2 Analytical Pressure Distribution for Beam Focusing

With the delay formula now defined, a procedure leading to the derivation of the pressure distribution for beam focusing was attempted[1]. The final pressure distribution for the beam focusing is: [45]

$$p(r,\theta,t) = \frac{p_0 a}{r}\frac{\sin\left(\frac{ka\sin\theta}{2}\right)}{\frac{ka\sin\theta}{2}}\exp\left(-\frac{jka\sin\theta}{2}\right)\exp\left[j(\omega t-kr)\right]\sum_{i=0}^{N-1}\exp(jA\cdot i+jB\cdot i^2), \tag{5.7}$$

where:

$$A=\frac{c(N-1)}{2F\tan^2\theta_s}\Delta\tau_0^2-\omega\Delta\tau_0+kd\sin\theta\ ,$$
$$B=\frac{c\Delta\tau_0^2}{2F\tan^2\theta_s}\ .$$

[1]See derivation in Appendix A.

By looking at eq. (5.7), it is observed that the pressure distribution for beam focusing cannot be simplified into a closed form, unlike the case of steering, which results in an analytical solution. This means that the analytical method is indeterminate; rather, the numerical method to simulate the acoustic field is desirable and powerful.

5.2 Numerical Simulation and Analysis

Since an analytical solution to the pressure distribution cannot be attained with focusing, a numerical procedure can be invaluable. A numerical simulation program[2] was developed which can obtain directivity and a variety of image pressure distributions for ultrasonic linear phased arrays. This software can simulate wave propagation fields for either steering or focusing, in both the near field and far field, and can produce directivities at any specified distance. The pressure along the steered direction when steering or focusing can also be simulated.

The simulation is based upon Huyghen's principle, which states that wave interactions can be analyzed by summing the phases and amplitudes contributed by a number of simple sources. The pressure at a given distance form the source is computed as follows:

$$p\left(r,t\right)=\frac{p_0}{r}\exp[j\left(\omega t-kr\right)-\alpha r]\ , \tag{5.8}$$

where p_0 is the initial pressure (Pa), α is the attenuation coefficient (Np/m) and r is the radial distance from the source (m). Our simulation routine is similar to that utilized by Buchanan [38], in that they modeled the transducer as an evenly spaced array of simple sources $(a \ll \lambda)$, whereas our model treats it as an ensemble of elements of finite width.

Figure 5.2 demonstrates how the pressure at any given point can then be attained by adding the contributions of a discrete number of simple sources which make up a

[2]For information regarding the software, contact Lawrence Azar at azar1@ix.netcom.com

given element. The contributions of all the elements, each modified by the product of a cosine envelope, are then added up.

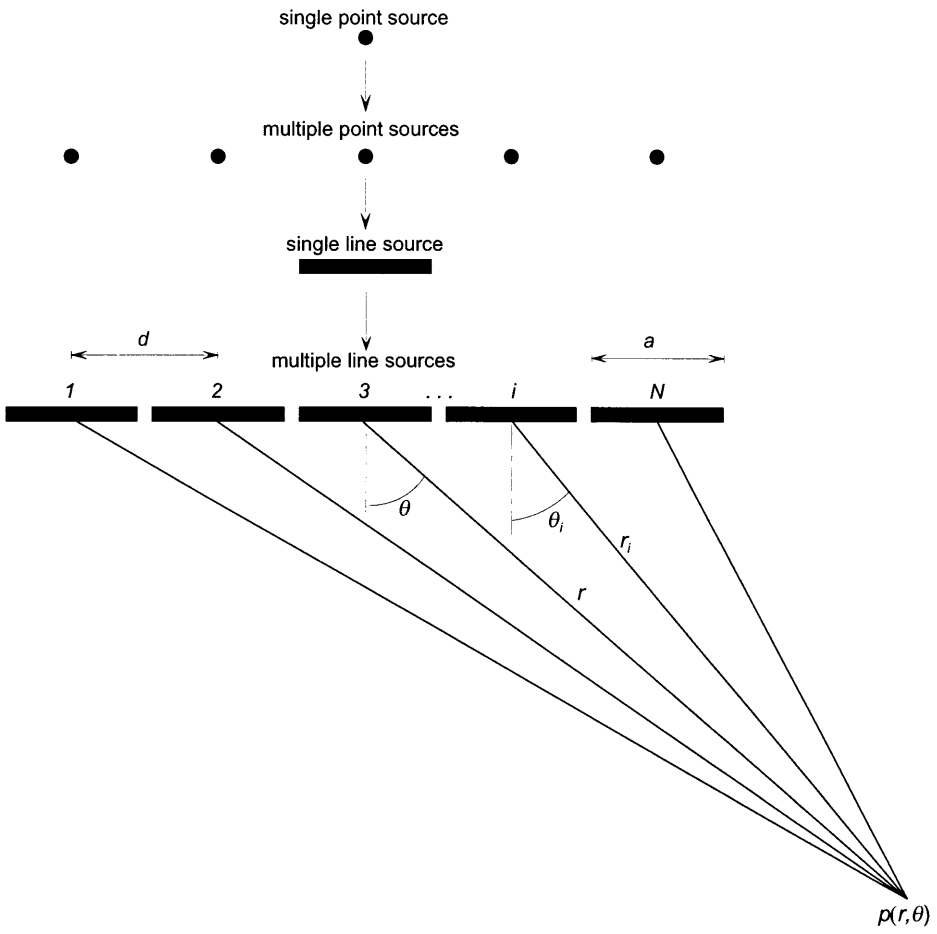

Figure 5.2: Approach to modeling the numerical phased array pressure distribution: the array is an ensemble of multiple line sources, each of which is composed of an infinite number of point sources.

5.2.1 Software Parameters

A sample input parameter file showing the settings programmed for the simulated directivity shown in figure 7.1(d) is given below. This program was written in "C," which either outputs a two column data file, or a matrix to a data file. Matlab was used to plot all image pressure distributions.

```
Quality..... 512
Number_of_elements..... 8
Wavespeed_m/s..... 3650
Frequency_Hz..... 170000
Angle_degrees..... 0
Ratio_d/Lambda..... 0.7
Focus_1_or_Steer_2..... 1
Image_1_Directivity_2_Enter_3_Wave_4_Line_5..... 2
Ratio_a/d..... 0.36
Odd_points_that_make_up_a..... 51
Focal_length_(meters)..... 0.3048
Directivity_distance_(meters)..... 0.3048
Attenuation_coefficient_(dB_per_meter)..... 10
Number_of_decimal_places_for_time_delay(9_is_for_ns).. 9
Ratio_L/lambda..... 0.5
Points_along_L..... 51
Width_of_image_(m)..... 1
X_min_(m)..... -0.3
Cosine_Factor_(nothing_0_cosine_1_cosine_squared_2)... 1
```

5.2.2 Single Element Characterization

The cosine contribution used in the numerical simulation provides a more realistic representation for slotted arrays, as demonstrated by Selfridge *et al.* [61]. He examined the radiation pattern of a narrow-strip transducer, and compared the results to the commonly used angular response, or far-field radiation pattern, of a single element given in the form:

$$p(\theta) = p_{\circ} \frac{\sin\left(\frac{\pi a \sin\theta}{\lambda}\right)}{\left(\frac{\pi a \sin\theta}{\lambda}\right)}, \tag{5.9}$$

where $p(\theta)$ is the pressure due to the acoustic field, $p_{\circ}$ is the pressure at the element face, a is the width of the transducer element, and λ is the wavelength of the acoustic wave in the propagating medium. They suggest that this formula has been arrived at by an inadequate interpolation of scalar diffraction theory because it is usually

assumed that the transducer element is surrounded by a rigid baffle. This leads to the result:

$$p(r,\theta) = \frac{p_o a}{j(\lambda)^{1/2}} e^{2j\pi r/\lambda} \frac{\sin\left(\frac{\pi a \sin\theta}{\lambda}\right)}{\left(\frac{\pi a \sin\theta}{\lambda}\right)} \cos\theta \ , \tag{5.10}$$

which is valid only in the far field. We can pull the fact that there is an extra $\cos\theta$ term from these results. This implies that however narrow the width of the transducer, the response must fall to zero at $\theta = \pi/2$ and fall off monotonically with angle θ, a result which would certainly seem to be physically reasonable [61]. Since this equation is used in the far field, the envelope can encompass the entire array. This cosine effect is not limited to the far field, but represents an envelope over the pressure distribution for each element. The simulation applies a per element cosine effect, which validates its use in the near field. The credibility of utilizing a cosine effect was also supported by Smith, *et al.* (1997), Bernstein, *et al.* (1997), and McNab, *et al.* (1985) [6,62,63].

A directivity plot is a measure of the pressure distribution at a fixed distance from the center of the array. The experimental setup will be discussed shortly, but for the sake of continuity, the following results shown in figure 5.3 are shown here. This demonstrates single element directivities for mortar and concrete, as compared to the simulation based on the cosine factor, which shows adequate agreement. Although only an approximation, the cosine factor was found to be an integral component to better match with experimental results.

5.3 Analysis of Beam Focusing Behavior

5.3.1 Numerical observations and discussion

A numerical simulation of the acoustic pressure field is utilized to demonstrate some key effects of focusing within and beyond the transition range of a linear phased

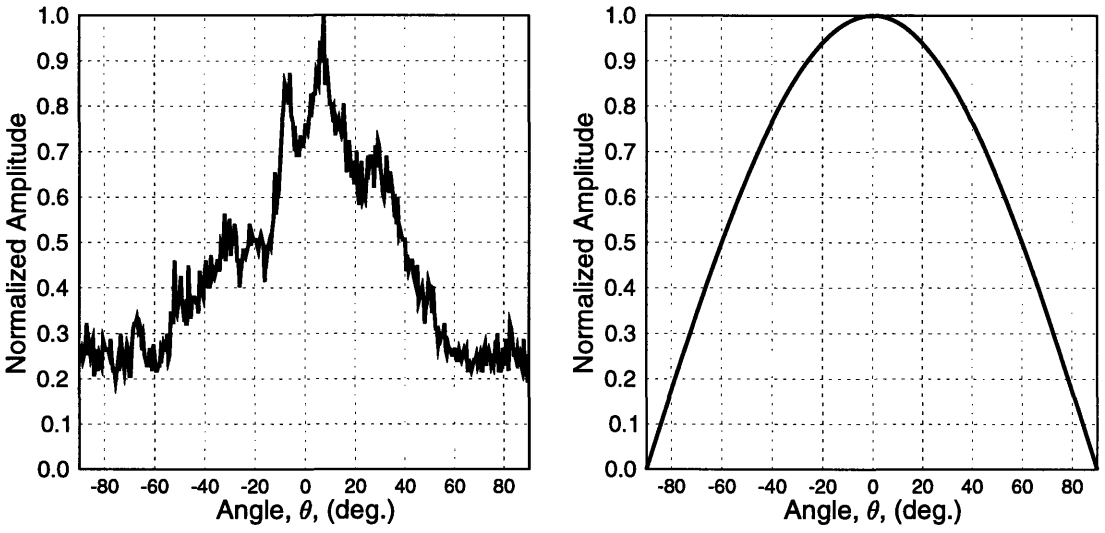

(a) Experimental: Mortar

(b) Simulated: Mortar

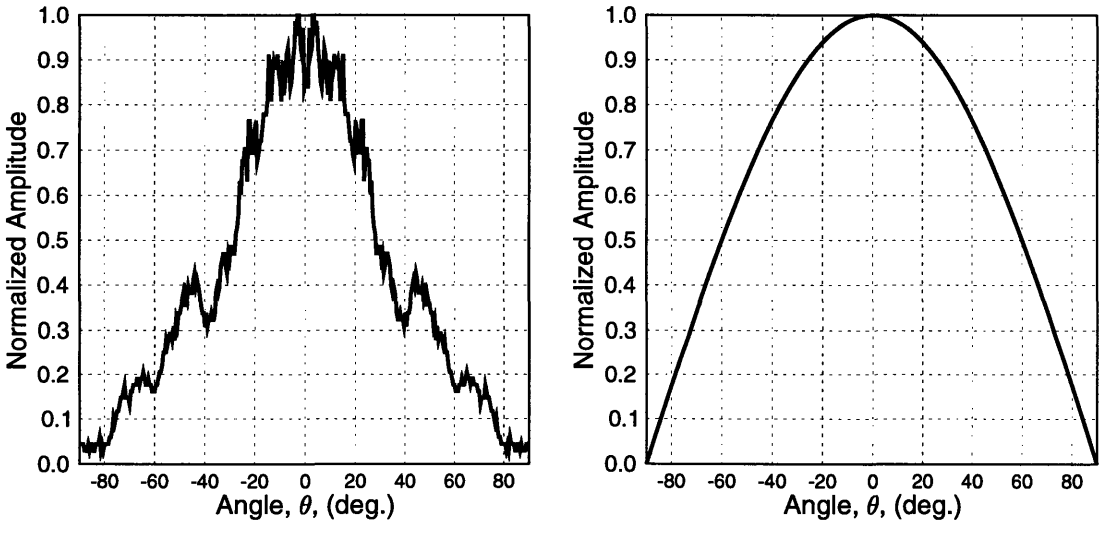

(c) Experimental: Concrete

(d) Simulated: Concrete

Figure 5.3: Single element directivities (R=30.48cm) for mortar (f=170kHz, d=0.7λ, and c=3650m/s) and concrete (f=140kHz, d=0.58λ, and c=3500m/s), both simulations include the cosine factor.

array. A comparison between steering and focusing is undertaken, revealing a distinct benefit of focusing over steering within the near field. Verification that the directivity of focusing converges to that of steering in the far field is attained both analytically and numerically. The simulated array is made up of 16 elements, with a frequency of 170 kHz, center-to-center element spacing of $\lambda/2$, and a wavespeed of 3650 m/s. The transition range for this array is calculated to be 34 centimeters.

A directivity plot is utilized to show the pressure along a radial distance from the center of the array, and is an accepted standard to demonstrate the accuracy of steering and focusing behavior [38,61]. An ideal plot should have a very good directivity, characterized by a very narrow main lobe width. They are derived from the image pressure distribution, which map the contributions of pressure from each element via Huyghen's Principle. These contributions incorporate the respective phase shifts, which lead to constructive and destructive interference of the ultrasound.

Figure 5.4 shows an image pressure distribution of the array being steered at 30 degrees, with figure 5.5 showing a directivity R taken at 20 cm. This directivity is in the near field of the array, and as a result, is quite poor. This is shown by the unsatisfactory width and shape of the main lobe. A received signal from this region could not be properly mapped to the appropriate location on an image, the resolution of which is based on the sharpness of the main lobe. Figure 5.6 shows an image pressure distribution as the array is also being focused at a distance of 20 cm. The directivity shown in figure 5.7, which passes through this focal point, shows a dramatic improvement over that of steering. Looking at the respective image distributions, the differences in the pressure fields are quite obvious. Focusing enables the acquisition of data from within a region not previously attainable, and contributes to increased resolution capabilities within the transition zone of the array.

Referring back to eq. (5.7), when the focal length is infinitely large, i.e., $F \to \infty$, then $A \to -\omega\Delta\tau_0^2 + kd\sin\theta$, and $B \to 0$. In this case the pressure distribution, i.e., eq. (5.7) becomes:

$$
\begin{aligned}
&p(r,\theta,t) \\
&= \frac{p_0 a}{r} \frac{\sin\left(\frac{ka\sin\theta}{2}\right)}{\frac{ka\sin\theta}{2}} \exp\left(-\frac{jka\sin\theta}{2}\right) \exp\left[j(\omega t - kr)\right] \sum_{i=0}^{N-1} \exp\left[j(-\omega\Delta\tau_0^2 + kd\sin\theta)\right] \\
&= \frac{p_{0a}}{r} \frac{\sin\left(\frac{ka\sin\theta}{2}\right)}{\frac{ka\sin\theta}{2}} \frac{\sin\left[\left(\frac{\omega\Delta\tau_0 - kd\sin\theta}{2}\right)N\right]}{\sin\left(\frac{\omega\Delta\tau_0 - kd\sin\theta}{2}\right)} \exp\left[-j\left(\frac{ka\sin\theta}{2}\right)\right] \\
&\quad \times \exp\left[-j\left(\frac{\omega\Delta\tau_0 - kd\sin\theta}{2}\right)(N-1)\right] \exp\left[j(\omega t - kr)\right].
\end{aligned}
\tag{5.11}
$$

This is exactly the pressure distribution for the steering of linear phased array [45]. Equation (5.11) shows that if the focal length is sufficiently large, i.e., beyond the transition range, the pressure distribution for focusing will converge to that of steering. To illustrate numerically, figure 5.8 shows an image pressure distribution of the array again being steered, but this time the directivity in figure 5.9 is taken at 50 cm. This is beyond the transition zone, and as such, the directivity is good. Figure 5.10 shows an image profile of the array now being focused at 50 cm, which now resembles that of steering. Taking a directivity at 50 cm, figure 5.11, the benefit over focusing is negligible. This is critical because at the transition zone, or close to that, the use of only steering is adequate. Since focusing requires analysis of a large number of points, it does introduce a cost, namely scanning time. Steering is much more efficient, as each sectorial line can be analyzed at a time.

Directivities are not the only criteria that should be considered when evaluating the importance of focusing. Simulating the pressure along the steered direction, figure 5.12 shows how the pressure of focusing compares to steering in the near and far field. Within the transition range, the pressure with focusing is more concentrated

than with steering. This added pressure contribution improves the resolution when acquiring data from the near field. Figure 5.12 also demonstrates one other important fact: the focal point does not always contain the greatest pressure. Although the focal point is at 20 cm, figure 5.12(b) shows that this is not the point of maximum pressure. Figure 5.13 demonstrates that only at the focal point, the directivity is well defined, as plots taken at the maximum pressure point and beyond the focal point demonstrate poor directivity. It should be noted that focusing at a specific point will give the maximum pressure that point can attain. The improvements in resolution are only valid in a small region around the focal point, and therefore imaging within the near field requires a discrete number of focal points per angle. Only the data that fell within the small focal zones should be acquired and processed.

Figure 5.12 also shows that beyond the transition range, the pressure along the steered direction, when focusing, will also converge to that of steering. This compliments the observations made analytically and utilizing the directivity plots.

5.3.2 Summary of Focusing Behavior

The existing delay formula required for focusing was found to be deficient, as it could only be used for an odd number of elements, and the required constant to keep the delays positive was awkward. This equation had been modified to incorporate either an odd or an even number of elements, and the required constant replaced. With the formula now defined, an attempt was made to reach an analytical solution to the pressure distribution with focusing. This resulted in an unclosed form. Rather, a numerical simulation is recommended to attain the pressure field. This simulation was derived using Huyghen's principle with a discrete number of simple sources.

Numerical directivity and image pressure profiles were utilized to compare the behavior of focusing and steering within and beyond the transition zone of the phased array. This demonstrated the importance of focusing in the near field, as the directivity for steering is quite poor, while that of steering is well defined. This transition range is proportional to the square of the overall dimension of the array. As the number of elements increase, there is a subsequent increase in the region where steering

cannot be used. To benefit from the added number of elements, focusing must be used in this "dead" zone. The numerical simulation proved our analytical conclusion that as the focal length goes to infinity, the pressure distribution of focusing converges to that of of steering.

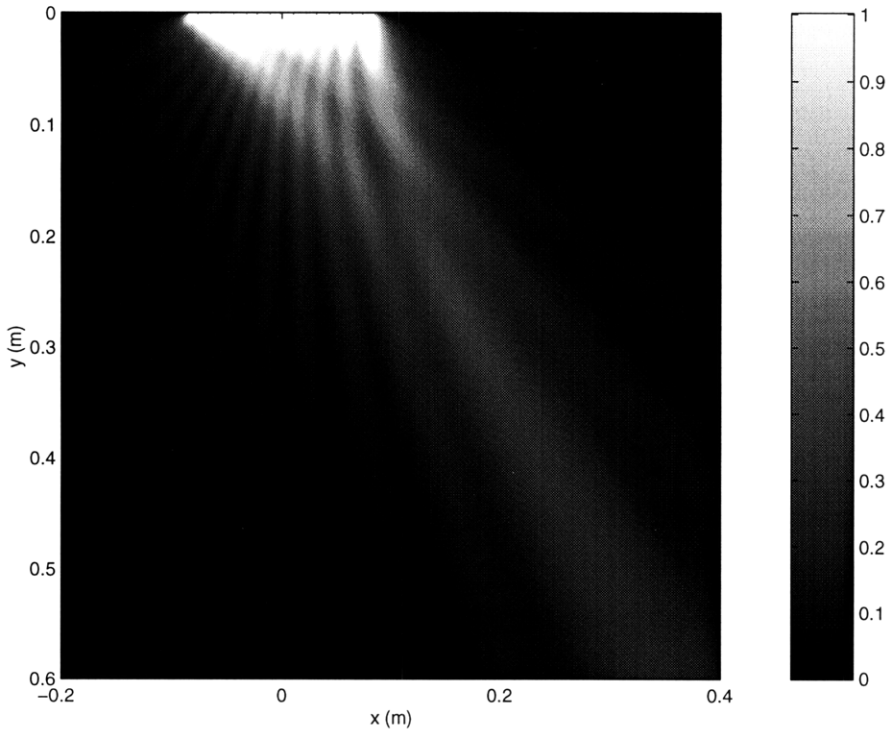

Figure 5.4: Steering in the near field.

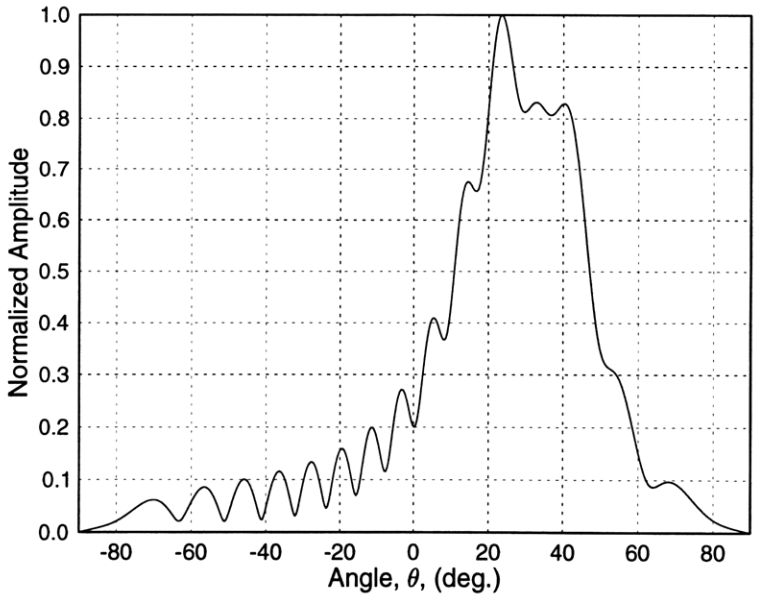

Figure 5.5: Steer: N=16, c=36500m/s, f=170kHz, θ=30°, d=$\lambda/2$ and R=0.2m.

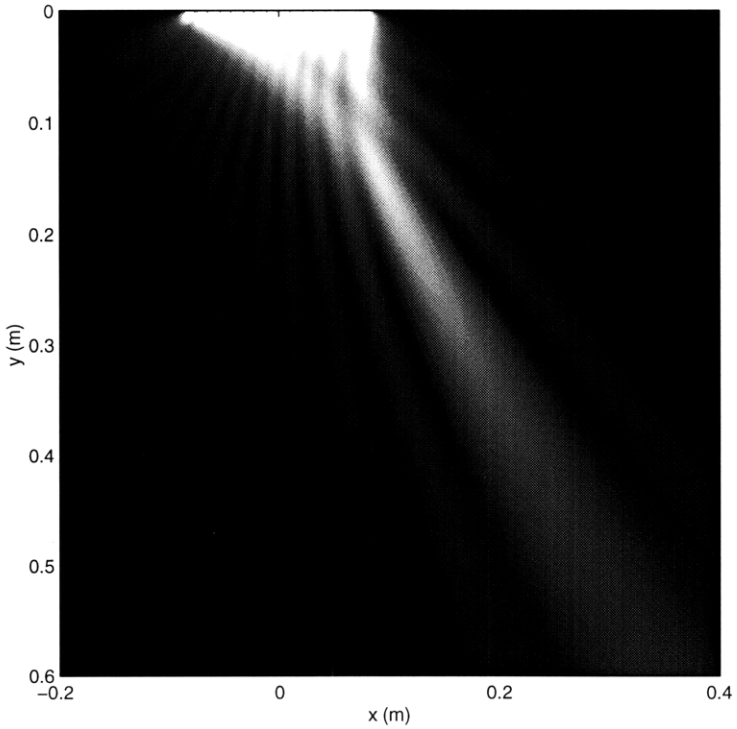

Figure 5.6: Focusing in the near field.

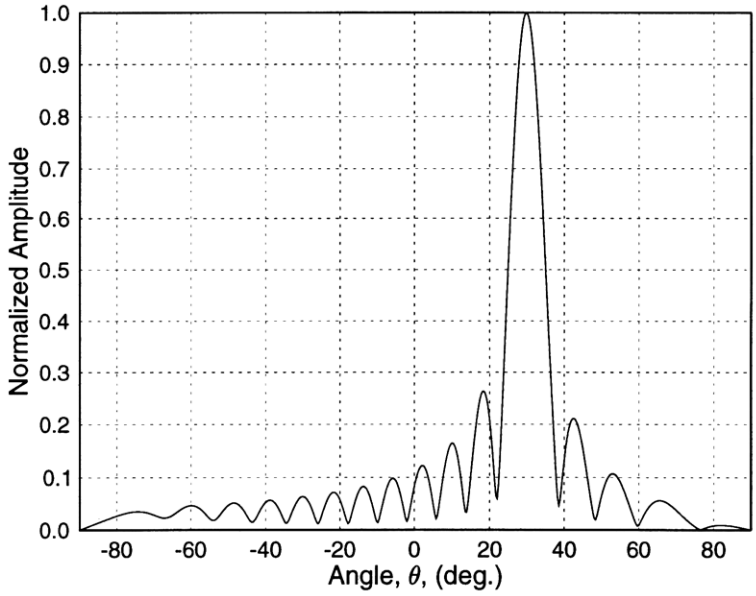

Figure 5.7: Focus: N=16, c=3650m/s, f=170kHz, θ=30°, d=$\lambda/2$, F=0.2m and R=0.2m.

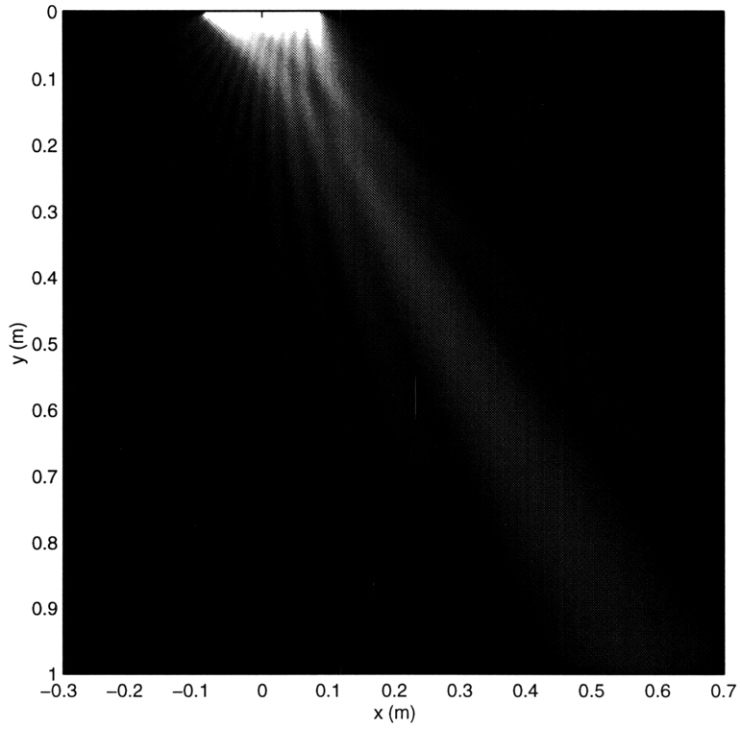

Figure 5.8: Steering in the far field.

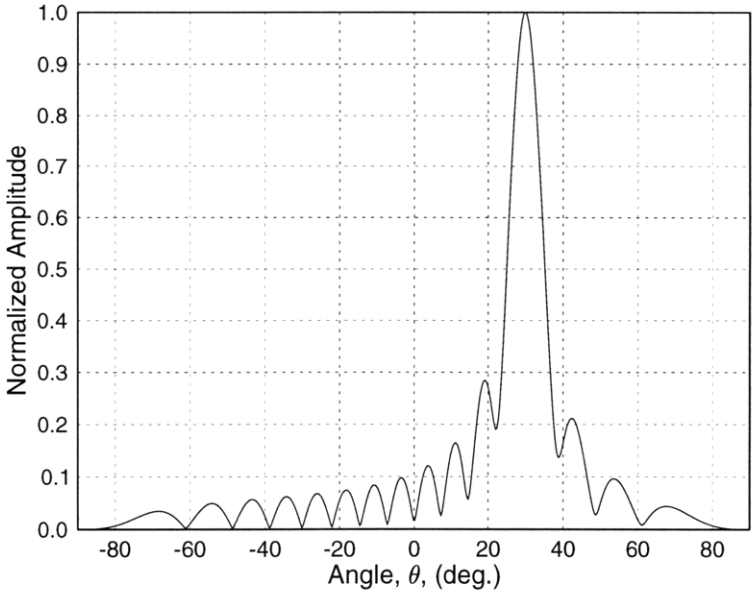

Figure 5.9: Steer: N=16, c=3650m/s, f=170kHz, θ=30°, d=$\lambda/2$ and R=1m.

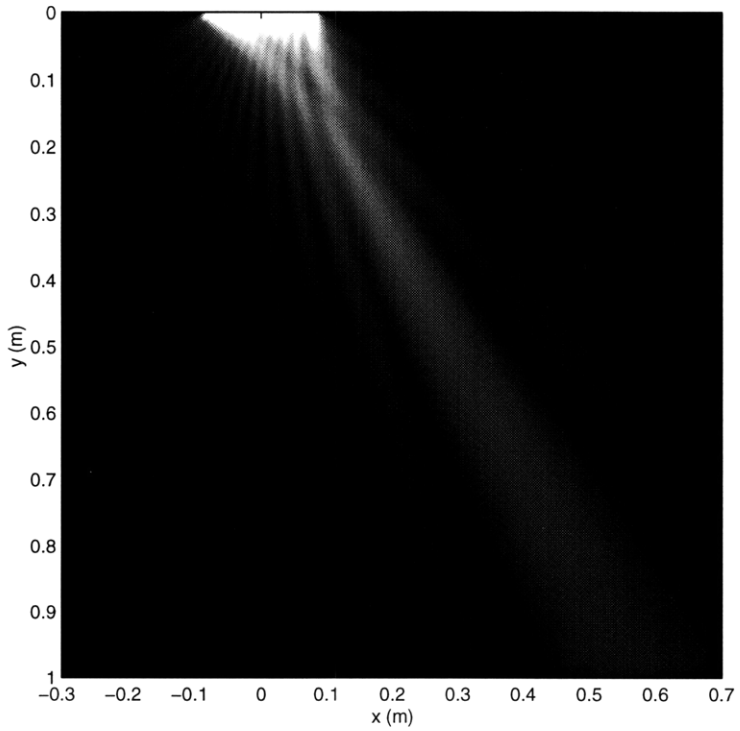

Figure 5.10: Focusing in the far field.

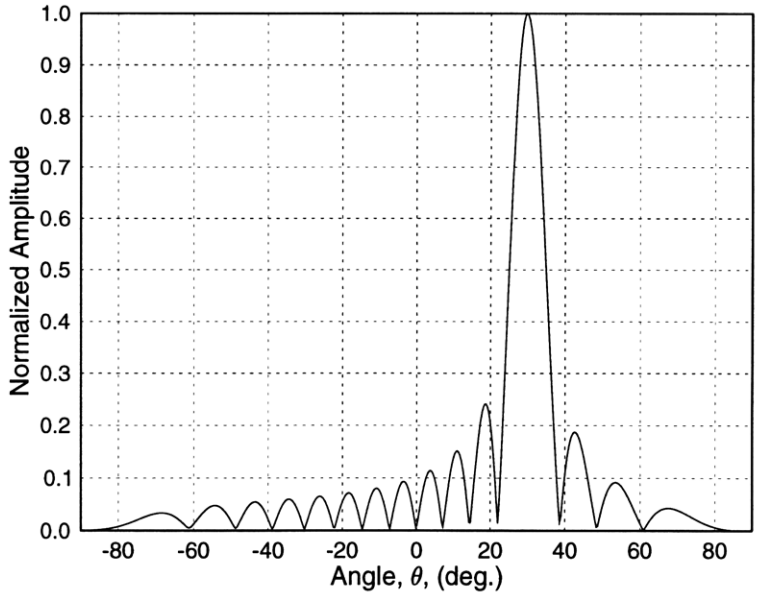

Figure 5.11: Focus: N=16, c=3650m/s, f=170kHz, θ=30°, d=$\lambda/2$, F=1m and R=1m.

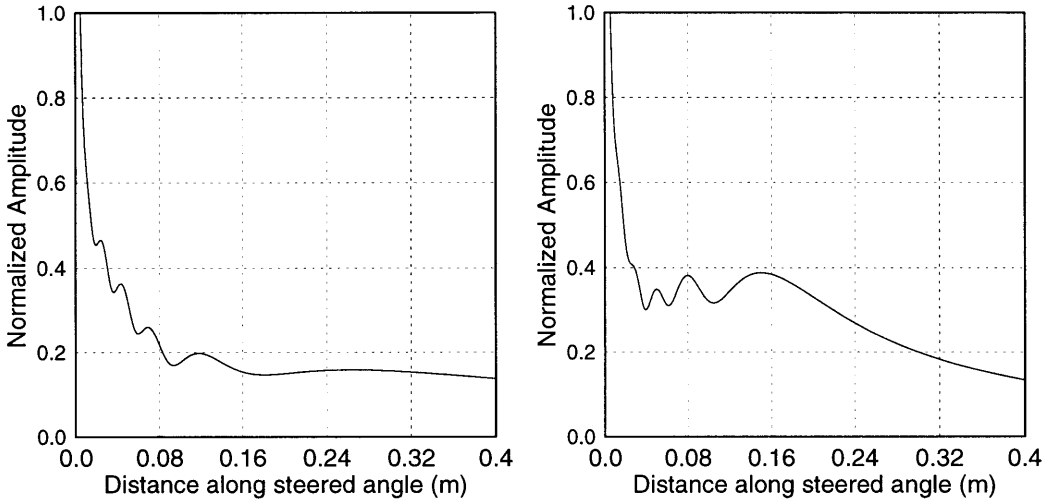

(a) Steering in the near field

(b) Focus in the near field: F=0.2m

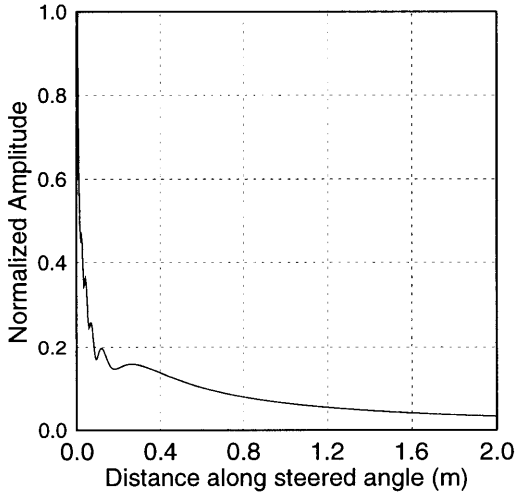

(c) Steering in the far field

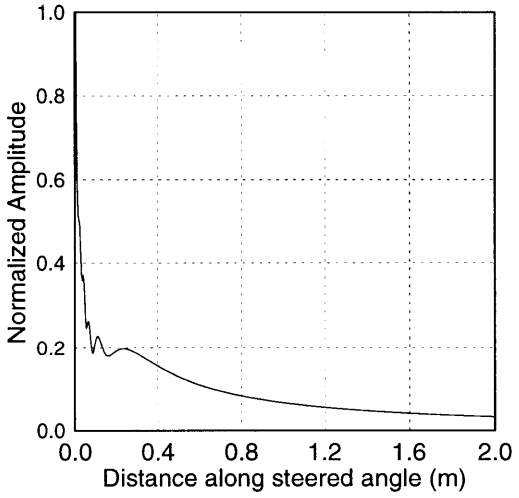

(d) Focusing in the far field: F=1m

Figure 5.12: Comparison of pressure profiles along steered angle between steering and focusing in the near field and far field (N=16, c=3650m/s, f=170kHz, θ=30°, and d=λ/2).

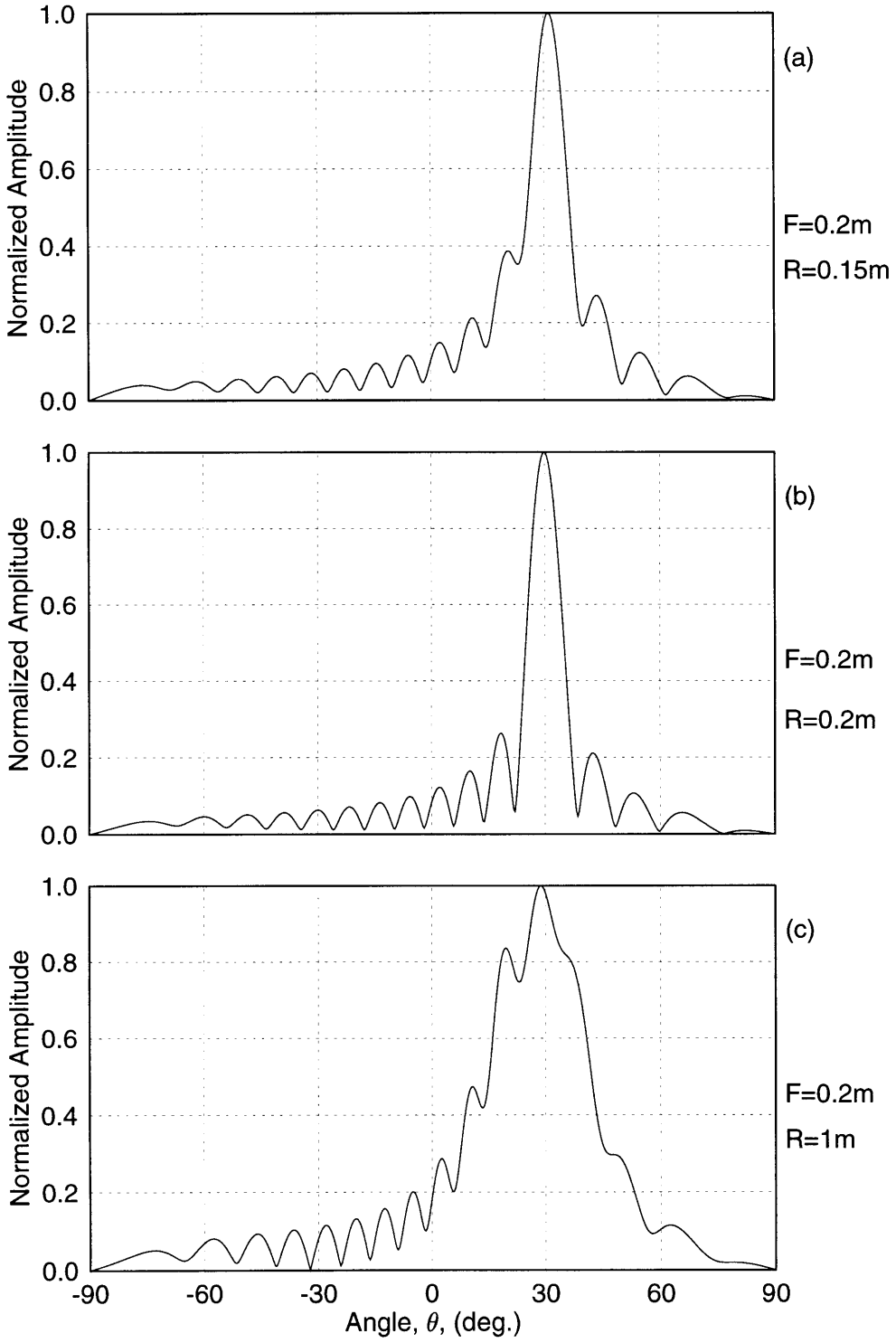

Figure 5.13: Focusing in the near field, with directivities taken at various distances (N=16, c=3650m/s, f=170kHz, θ=30°, and d=$\lambda/2$).

Chapter 6

System Design and Experimental Setup

A novel approach to attain the steering and focusing behavior of the array in a cementitious medium was undertaken. In this section, the system components that drive the array, and the automated assembly that allowed acquisition of the directivities is discussed.

6.1 Pulser and Delay Circuit

6.1.1 Circuit Specification and Layout

A phased array sensor is useless without a manner to trigger each element to their respective time delay. The layout of the circuit that enabled this, as well as the required peripheral devices is shown in figure 6.1. The delayed pulses used to excite the transducer were created, using a 16-channel independently programmable multiplexing circuit. The initial TTL signal was furnished using a function generator (HP 33120A) and dispersed to delay banks which are composed of tapped digital delay lines and multiplexers. The delays for each channel were adjustable in 5 ns steps up to a maximum delay of 2500 ns. A 192-bit programmable digital I/O board (Cyber Research DIO-192) was used to interface the controlling computer to the in-

puts of the multiplexers. Each delayed TTL signal subsequently triggered a high voltage negative spike pulse which was issued to a specific array element through an individually shielded cable. General specifications for the delay and pulser circuitry are given in Tables 6.1 and 6.2.

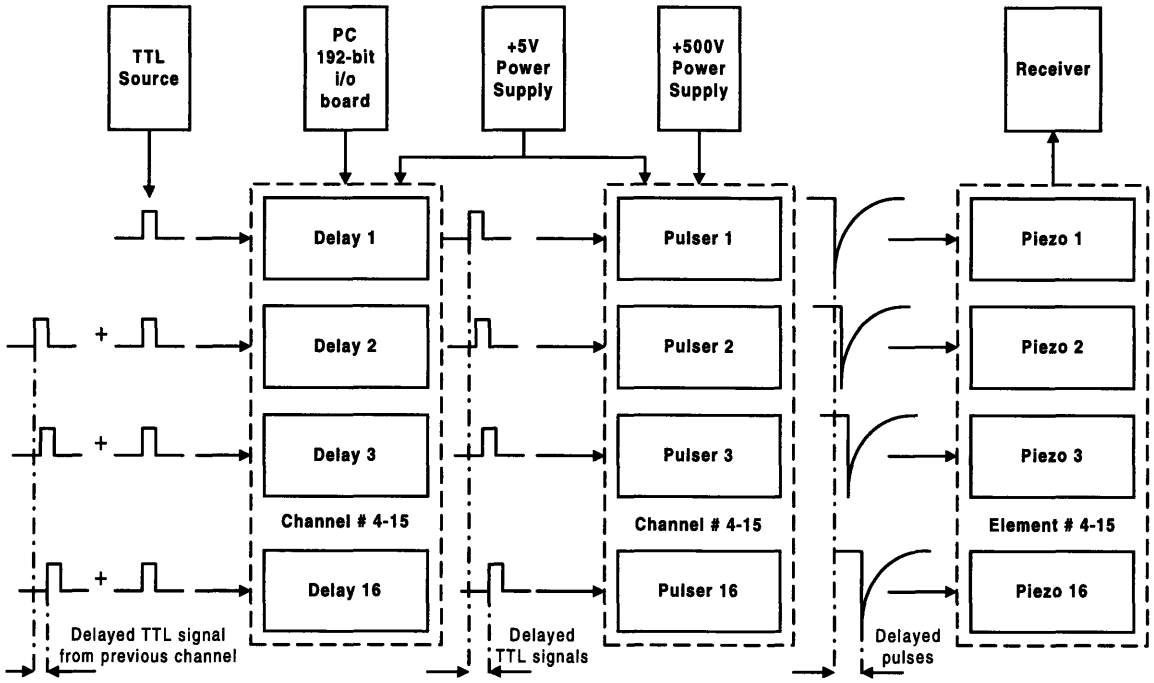

Figure 6.1: Circuit layout for the 16-channel phased array system.

6.1.2 Required Time Delays and Resolutions

For most steering angles, the outputs of each channel were rewired to form a serial connection, such that the output from channel n was fed to the input of channel $n+1$, and so forth. This enabled very high delay ranges up to approximately 15 to 22 μs and allowed the beam to be steered and focused to adequate angles, dramatically increasing the field of view.

No. of channels:	16
I/O per channel:	12
Total I/O:	192
Input signal:	TTL
Resolution:	5 ns
Range:	2500 ns (ch.1-ch.9)
	1500 ns (ch.10-ch.16)

Table 6.1: Specifications for phased array delay circuit.

No. of channels:	16
Input:	TTL
Pulse amplitude:	0–500, 1 V steps, programmable
Pulse width:	10 μs
Repetition rate:	100 Hz–5 kHz, continuous
Polarity:	negative
Pulse type:	spike

Table 6.2: Specifications for pulser and high voltage circuitry.

As will be shown, directivity plots will be attained at a distance (R) of 30.48 cm for steering and focusing, the latter also requiring a focal length (F) of 30.48 cm. Equations (4.1) and (5.6) were plotted, which demonstrate the angular limit the system can support.

Figures 6.2(a) and 6.3(a) plot the required time delays for steering and focusing, respectively, for the array using 16 elements. As shown, the maximum angle attainable is limited to approximately 15°. Figures 6.2(b) and 6.3(b) demonstrate the required 1° resolution in time. With a 5 ns system resolution, and a 15° angle limit, this system will be satisfactory in attaining the required delay in increments of 1°. Also, with the large wavelength produced using low frequency ultrasound, the minor delay errors experienced were found to be negligible.

To increase the angular capabilities, 8 elements were used, while maintaining the inter-element spacing when using 16 elements. As mentioned earlier, this spacing d

was 1.454 cm. This enabled steering and focusing capabilities up to approximately 40°, as shown in figures 6.4(a) and 6.5(a).

6.2 Automated Testing Assembly

An experimental device was fabricated for calibrating phased arrays used for assessing cementitious materials. The directivity patterns for both steering and focusing were obtained using the assembly illustrated in figures 6.6 and 6.7. A concrete (or mortar) wheel, with an array positioned within the groove, rotates about its center, and the transmitted energy is received by a stationary receiver located at the base of the assembly. Detection of energy along the periphery is recorded as the wheel is rotated from -90° to 90°, maintaining a set delay for the array. As the receiver is not in contact with the wheel, partially immersing the material in water is required for continued transmission of the energy.

The assembly is comprised of a disk-shaped concrete (or mortar) wheel bolted to an aluminum disk, and is cantilevered from a vertical steel support shaft attached to a rigid steel base. The motion of the disk was controlled by a programmable step motor which not only automates testing, but also ensures accuracy in angular position. A 100:1 gearbox was placed between the motor output shaft and the coupling shaft to the wheel in order to increase the torque and reduce the inertial mismatch between the motor and the wheel.

The concrete and mortar wheel fabricated measured 30.48 cm in radius and 6.35 cm in thickness. Selection of the disk's radius was based on the approximate near field formula, $Z_{TR} = D^2/4\lambda$, where D is the array aperture. This yielded a Z_{TR} of 11.5 cm for 8 elements, and a Z_{TR} of 50.0 cm for 16 elements in concrete. As we were interested in measuring directivities in both the near and far fields to examine the benefit of focusing, a directivity length (R) of 30.48 cm seemed tp be a good medium distance. The thickness of the disk provided enough clearance so that the first received signal was not interfered with any sidewall reflections.

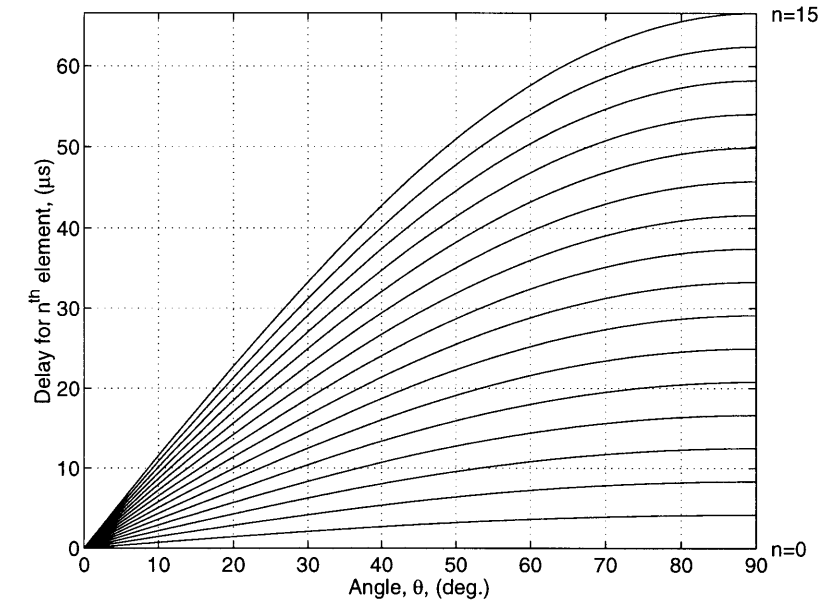

(a)

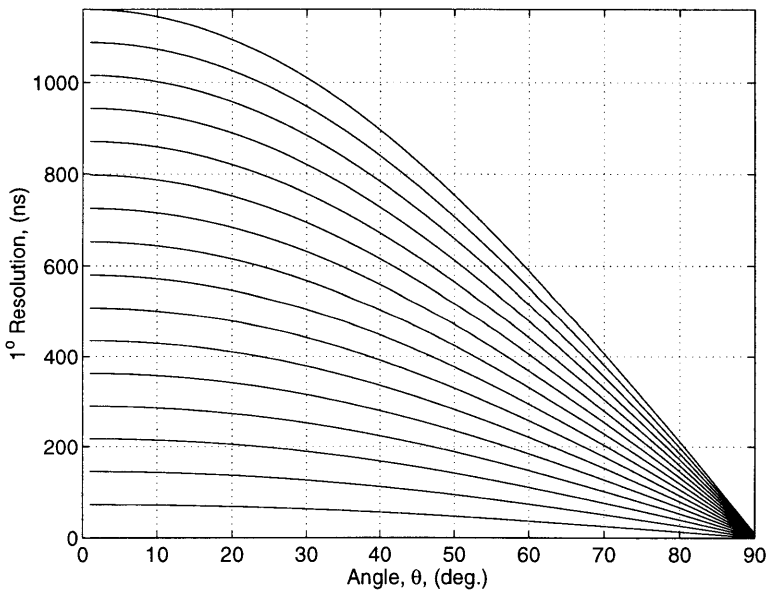

(b)

Figure 6.2: Steering delay and resolution in concrete (N=16, c=3500 m/s, d=1.454 cm, and F=30.48 cm).

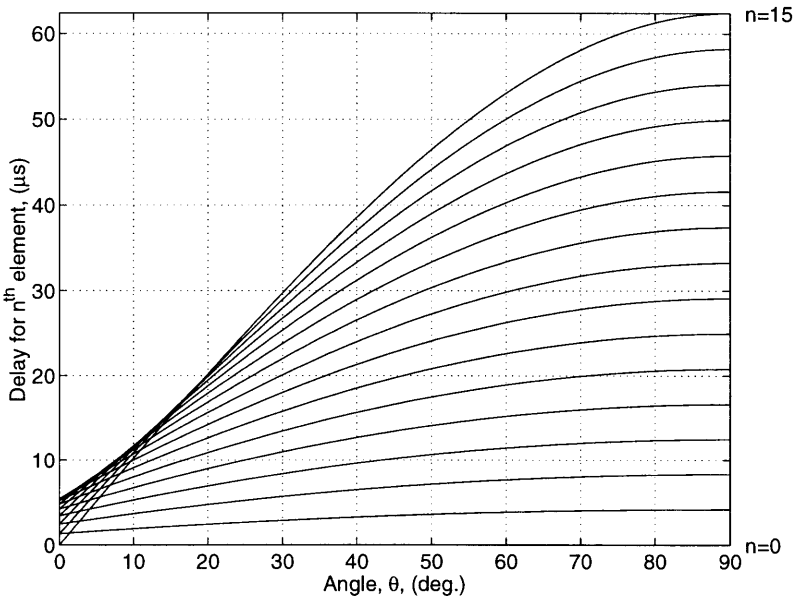

(a)

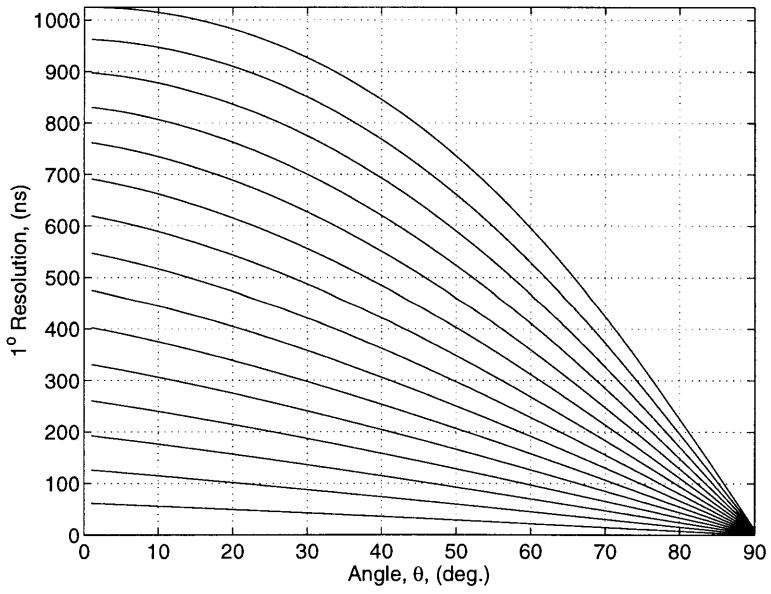

(b)

Figure 6.3: Focusing delay in concrete (N=16, c=3500 m/s, d=1.454 cm, and F=30.48 cm).

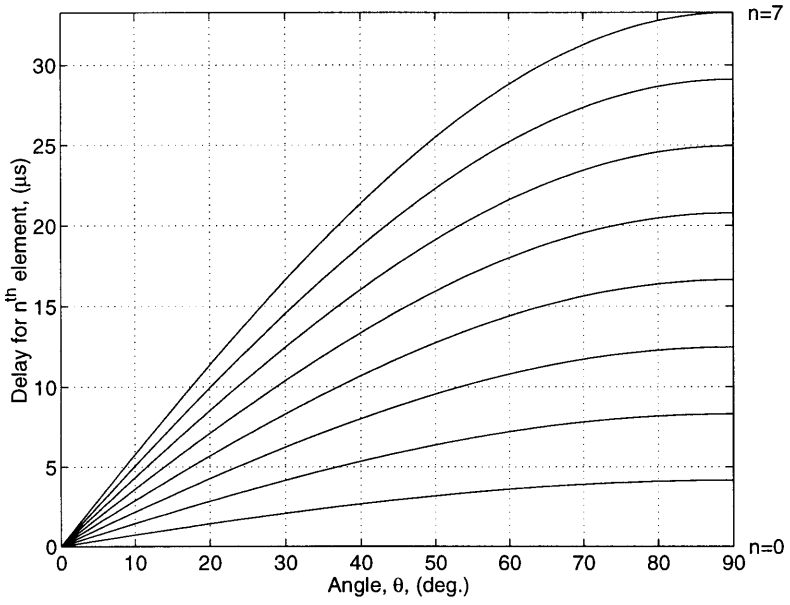

(a)

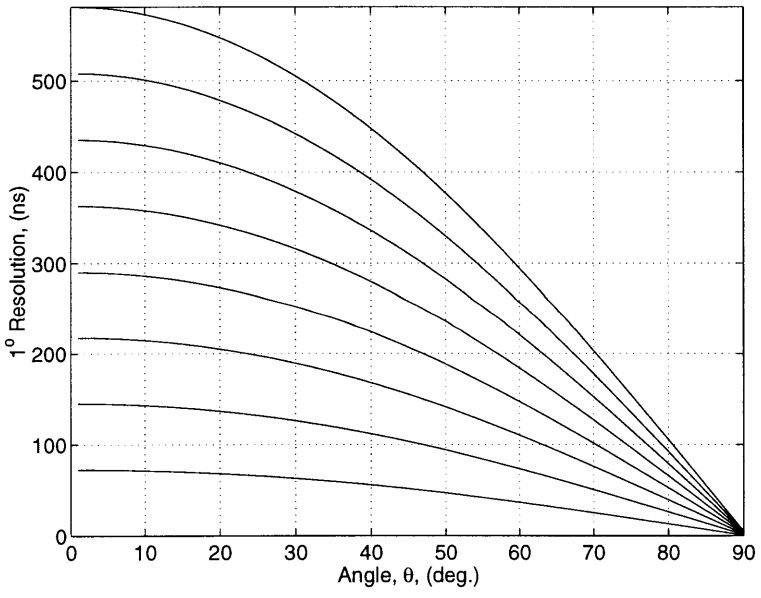

(b)

Figure 6.4: Steering delay and resolution in concrete (N=8, c=3500 m/s, d=1.454 cm, and F=30.48 cm).

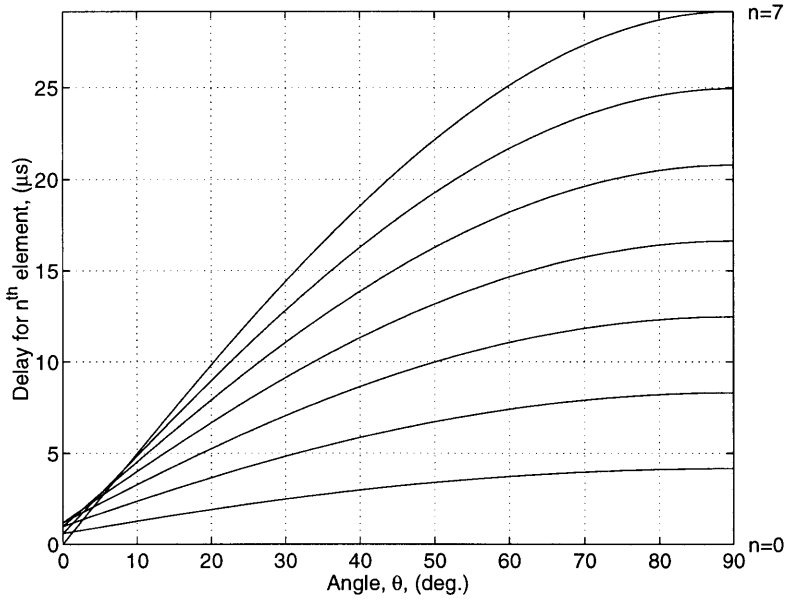

(a)

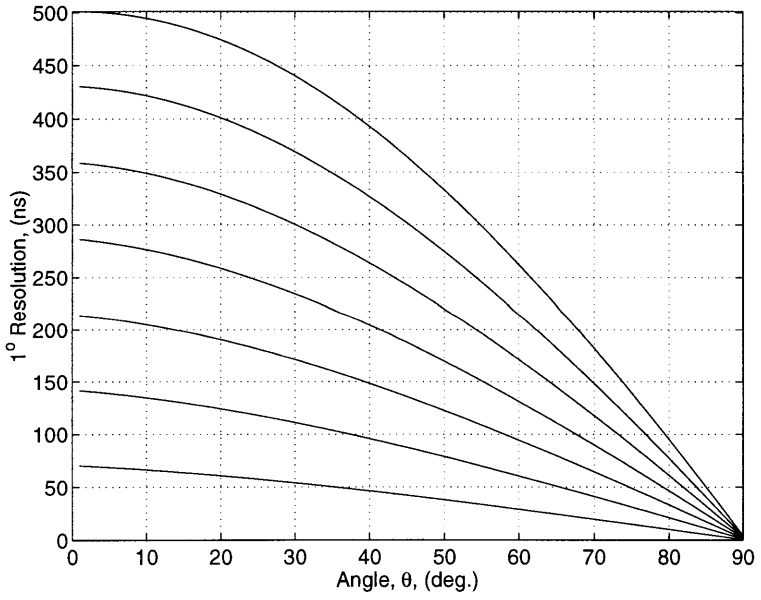

(b)

Figure 6.5: Steering delay and resolution in concrete (N=8, c=3500 m/s, d=1.454 cm, and F=30.48 cm).

Other features of this assembly include a rectangular groove, which was introduced above the horizontal centerline of the disk, to house the phased array. Expansion bolts were inserted in the groove to stabilize the sensor and to maintain strong coupling contact with the aluminum surface. The bottom half of the disk was placed inside a Plexiglas water tank, with the water level set slightly above the rim. A fabricated 150 kHz fixed-focused immersion transducer, situated directly beneath the center of the disk, was focused at the rim to receive the transmitted energy.

6.3 Experimental Testing Procedure

The overall connectivity of the various components and sub-assemblies used in this experiment is shown in figures 6.8 and 6.9. There are essentially three control paths in this setup which include (1) digital I/O control for beam steering, (2) motion control and (3) data acquisition. A central controlling PC enabled and monitored these routines through a 192-bit parallel I/O board, RS-232 serial port and GPIB, respectively. These ports were programmed in "C," hence providing flexible low-level control.

The I/O board was interfaced to the delay circuit module and selected the inputs of an array of multiplexers as logically high or low. These bit patterns were used to create various time delays so that the ultrasonic beam was steered or focused at an angle θ_s. The phased array was positioned in the groove of the circular calibration fixture whose rotation was controlled by the step motor.

The transmitted sound field was detected by a focused transducer and the signal was amplified with an external receiver unit (Panametrics 5072PR) and displayed using a digital oscilloscope (Tektronix TDS-210, 1 GHz sampling rate) which was synchronized with the rotation of the wheel at every 0.5°. All waveforms were acquired through GPIB and were gated and peak-detected. Directivities were obtained from $-90°$ to 90° by plotting the peak amplitude on the y-axis and the corresponding angle of the disk on the x-axis.

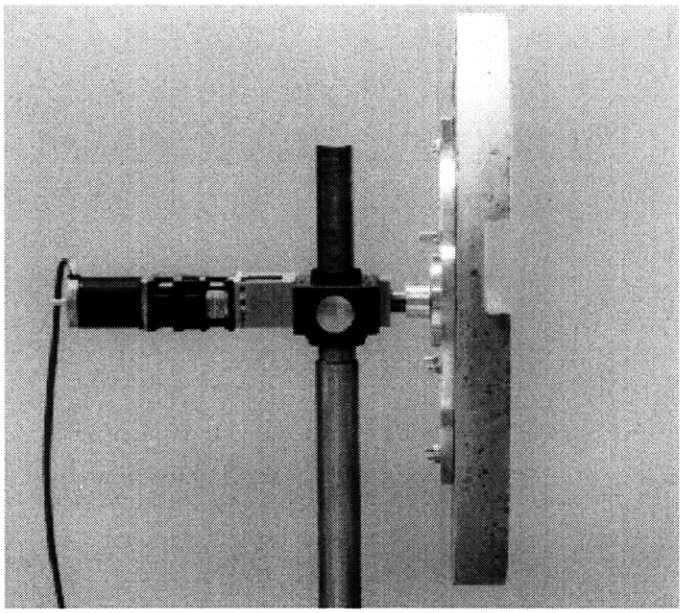

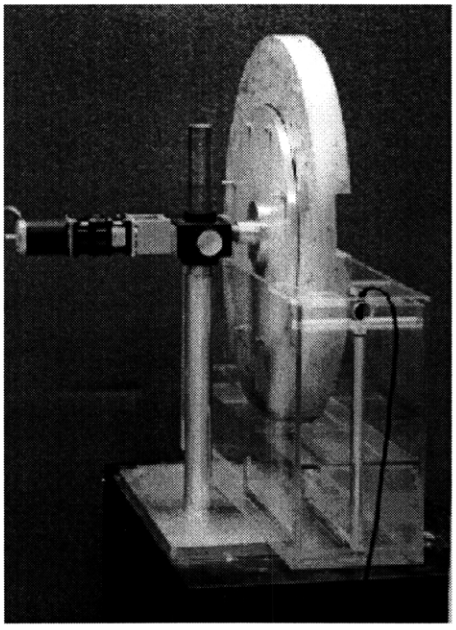

Figure 6.6: Slotted concrete wheel mounted on motor controlled stand via an aluminum plate bolted to the back.

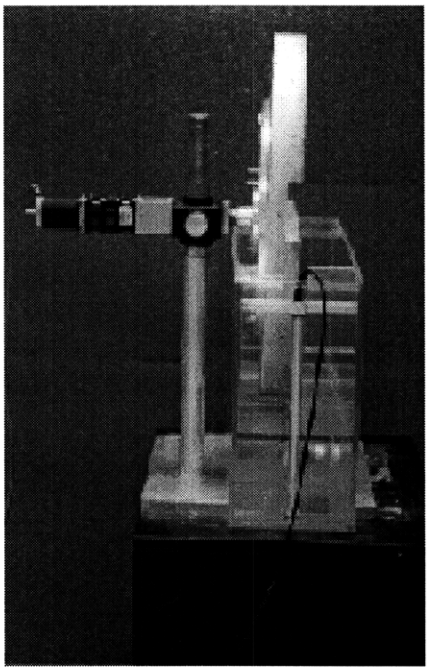

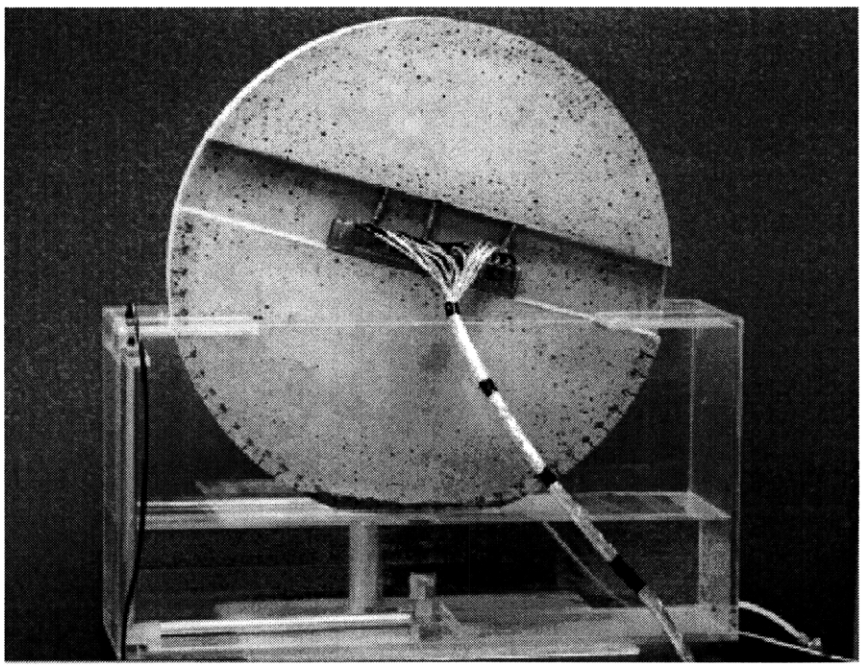

Figure 6.7: Concrete wheel in the water tank with a focused immersed transducer placed at the bottom for receiving the ultrasound, and the phased array transducer placed within the center of the wheel.

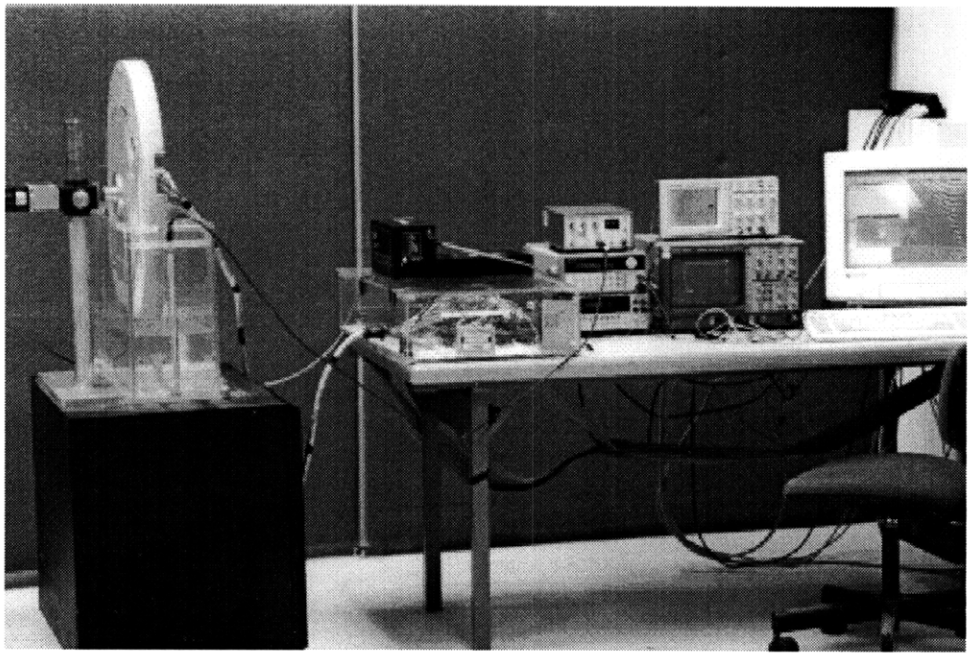

Figure 6.8: Complete setup, including wheel assembly, delay circuit, pulser/receiver, function generator and oscilloscope.

The sensor is calibrated and then programmed for a particular steering angle, θ_s, and the disk is rotated to the desired angle. An oscilloscope displays the received pulse, and a narrow acquisition gate is placed on the maximum peak of the first received pulse. Only the data within this gate will be acquired, and processed. The disk is then rotated to -90°, which is the start position of the setup.

Each time the wheel is rotated at a set increment of 0.5°, a waveform appearing within the gate is acquired from the oscilloscope, and stored. Once the assembly has rotated a full 180°, all the acquired waveforms are processed to attain their respective maximum amplitude (positive or negative). These maxima are stored in a data file, and directivities are plotted.

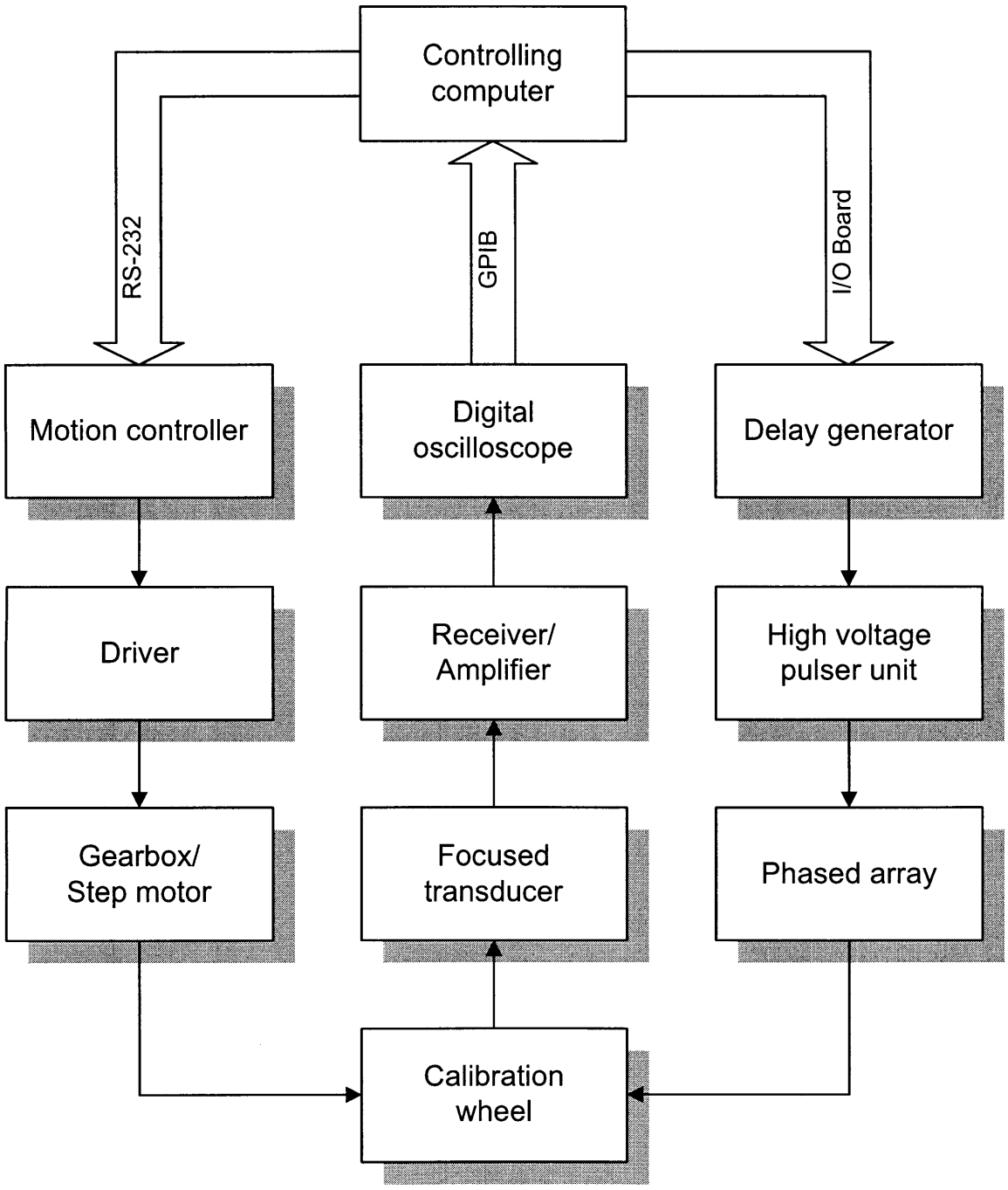

Figure 6.9: Experimental setup showing RS-232 motion control of step motor, GPIB for data acquisition and I/O board for steering control.

Chapter 7

Experimental Results and Discussion

This chapter covers acquisition of the directivity curves obtained for various steering and focusing angles, and other parameter settings. Experimental results were initially obtained for mortar, for an array with 8 elements and 16 elements, and then for a concrete medium. The experimental directivities were compared to the numerical simulation discussed in section 4.2. These results show excellent agreement quantitatively with the predicted steering and focusing characteristics.

7.1 Directivity Plots

This section provides the results of the experimental and simulated parameter study. For figures 7.1 to 7.11, experimental directivity curves for steering (a) and focusing (b) were compared to their respective predictions (b) and (d). This also allowed for direct examination of the potential benefits of focusing over steering.

With a directivity length R fixed at 30.48 cm, due to the geometry of the wheel assembly, observation of the behavior of beam directivities within the near field and far field of the array were attained by changing the overall lateral dimension D of the sensor. Table 7.1 shows the values of the transition range under various parameters, noting that the same d was utilized throughout.

	Mortar	Concrete
N=8	13.3 cm	11.5 cm
N=16	58 cm	50 cm

Table 7.1: Z_{TR} values under various N and type of media

For $N = 8$, experimental results for both steering and focusing were attained for 0°, 15°, and 25°. With concrete, an angle of 40° was also obtained. For $N = 16$, experimental results for steering and focusing were acquired for 0° and 15°. For reference, the directivities may be grouped according to the same parameter settings for type of media and N as follows:

- Figs. 7.1–7.3: Mortar, $N = 8$.
- Figs. 7.4–7.5: Mortar, $N = 16$.
- Figs. 7.6–7.9: Concrete, $N = 8$.
- Figs. 7.10–7.11: Concrete, $N = 16$.
- Fig. 7.12: Study of focusing at a constant R, for various F.

7.2 Discussion

The major observation drawn from figures 7.1 to 7.11 is that phase steering and focusing is not only possible in a cementitious medium, but that it does so with excellent agreement to predicted theory. As mentioned, directivity is the key parameter used to measure the accuracy and steerability of a phased array transducer.

Good accuracy implies a close match of the main lobe width of the experimental results to the simulation directivity. A notation for the main lobe sharpness factor q_{-6dB} will be utilized to evaluate the accuracy of all the experimental results. q_{-6dB} is an angular measure of the main lobe width at -6dB (50%) normalized by π (180°). Steerability is a criterion used to evaluate the correlation of the measured θ_s to the

Parameters			***Simulated Results***		***Experimental Results***	
mortar/concrete	N	θ_s	θ_s	$q_{-6dB} \cdot 180°$	θ_s	$q_{-6dB} \cdot 180°$
mortar (steer)	8	0°	0°	18°	1.5°	17°
mortar (focus)			0	12.4	1	11.5
mortar	8	15	15	14.4	14.5	16.5
			15	13	15	14
mortar	8	25	25.2	14.5	27	15.5
			24.8	13.4	26	14.6
mortar	16	0	NA	39.6	NA	31.3
			0	6.2	1	8
mortar	16	15	NA	39	NA	29
			15	6.5	17	6.6
concrete	8	0	0	16	0	20
			0	15	1	14.5
concrete	8	15	15	16.4	15.5	15.5
			14.6	15.5	15.5	15
concrete	8	25	24.8	17.3	24.5	20.2
			24.5	16.3	23.5	14
concrete	8	40	39.3	19.3	41.5	19.2
			39	18.6	41	19.2
concrete	16	0	NA	36	NA	34
			0	7.8	0	8.2
concrete	16	15	NA	38.5	NA	38
			15	8.2	15	11.5

Table 7.2: Summary of simulated and experimental results, demonstrating the accuracy and steerability of the directivities. For each case, results are given for steering followed by focusing.

expected θ_s. Values for $q_{-6dB} \cdot 180°$ and θ_s were collected from all experimental and simulated directivities, and summarized in Table 7.2. These values are given for steering, followed by focusing, for each representative parameter. Several observations can be inferred from the information summarized, and from the experimental directivity curves.

7.2.1 Steerability and Accuracy

Comparing the expected θ_s to those collected from the experimental results, the array is proven to exhibit great steerability, with an average variation of only 0.75°. Without proper steerability, angular errors will exist when imaging the received waveforms. This array has great steerability, as good as any commercially available high frequency arrays used in current medical and NDE applications. Also observed, is the negligible steerability differences between steering and focusing. With the case of steering in the near field, the resulting poor accuracy negated the possibility of attaining steerability values. These were marked as "Not Applicable."

The reason for attaining q_{-6dB} values was to observe the accuracy of the experimental directivities as compared to the simulation. Excluding steering in the near field, which exhibits inherently poor resolution, the average deviation from the simulation in $q_{-6dB} \cdot 180°$ was only 1.4°. The directivities obtained showed excellent accuracy.

7.2.2 Effects of d and N

The effects of parameters such as d and N on q_{-6dB} can also be observed from the results found in table 7.2. Increasing N has the most dramatic effect in reducing the main lobe width. With a constant N, increasing d can also reduce this width as well, but the angular resolution will be limited due to the appearance of grating lobes.

Figures 7.1 to 7.3 demonstrate the behavior of an 8 element array in mortar. With $d = 0.7\lambda$, a grating lobe was predicted, expected to increase in magnitude with increasing θ_s, as observed most dramatically for $\theta_s = 25°$. The appearance of a grating lobe is not a reflection of the performance of the sensor in mortar, but a consequence of d being larger than $\lambda/2$. The fact that the experimental results show the grating lobe actually confirms that the waves are interacting as predicted. Although the shape and location of the grating lobes do not match perfectly, this can be attributed to the approximations of the numerical modeling. With a value of $d = 0.582\lambda$ for

concrete, a significant grating lobe is not observed for figures 7.6 to 7.9, which was limited to a maximum θ_s of 40° because of circuit limitations.

7.2.3 Focusing Behavior

Focusing ultrasound is a key function of phased arrays, especially within cementitious materials. As shown in Table 7.1, there is a significant increase in the near field length when the number of elements is increased from 8 to 16. Using 8 elements, figures 7.1 to 7.3 and figures 7.6 to 7.9 demonstrate the negligible improvement focusing will have over steering within the far field. Table 7.2 does show some improvement though, more so with mortar, which has a slightly longer transition zone than with concrete.

When the number of elements is increased from 8 to 16, R appears within the near field of the sensor. The directivities acquired when steering the ultrasound, shown in figures 7.4 to 7.5 and figures 7.10 to 7.11, demonstrate poorly shaped main lobes. When the ultrasound is focused at the rim of the wheel, dramatic improvements for the directivities are observed. These focused directivities show excellent steerability, and excellent accuracy as compared to the simulated results. The results also confirm the observations made in section 4.3.

Experimental and simulated results demonstrating the behavior of focusing at a constant directivity distance for various focal lengths are shown in figure 7.12. Observe that if the focal point appears closer to the sensor ($F = 20\ cm$), the directivity attained has a much larger main lobe width than that observed when $F = R = 30\ cm$. This is due to the spreading of the beam beyond the focal point. When the focal point was beyond the directivity length ($F = 40\ cm$), there was some degradation, but not as dramatic. This shows that the range about the focal point that will give acceptable directivities is greater before the focal point, than beyond.

7.3 Summary and Conclusions

The conclusion drawn from the experimental results is that phase steering and focusing ultrasound is possible in a cementitious medium. Theses results showed excellent steerability and accuracy, and provide excellent agreement to the numerical simulation. In summary, the following key points were observed:

- The array is proven to exhibit great steerability, with an average variation of only 0.75°.
- The directivities obtained show excellent accuracy, with an average deviation from the simulation in $q_{-6dB} \cdot 180°$ of only 1.4°.
- Increasing d improves q_{-6dB} while keeping N constant.
- Increasing N improves q_{-6dB} while keeping d constant.
- Grating lobes were observed for $d >> \lambda/2$, increasing in amplitude with increasing θ_s.
- Steering within the near field results in very poor directivities.
- A benefit of focusing over steering within the near field of the array was observed.
- The directivity of focusing converges to that of steering in the far field.
- The range about the focal point that will give acceptable directivities is greater before the focal point, than beyond.

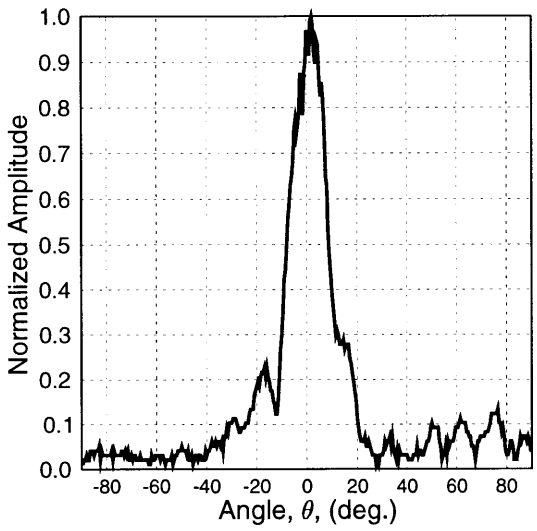

(a) Experimental: steering at θ=0°

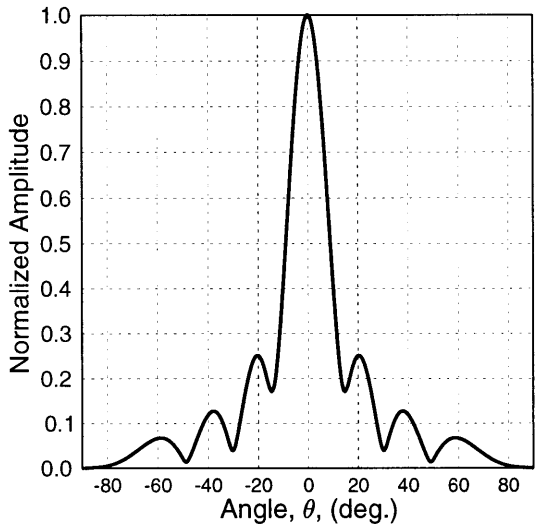

(b) Simulated: steering at θ=0°

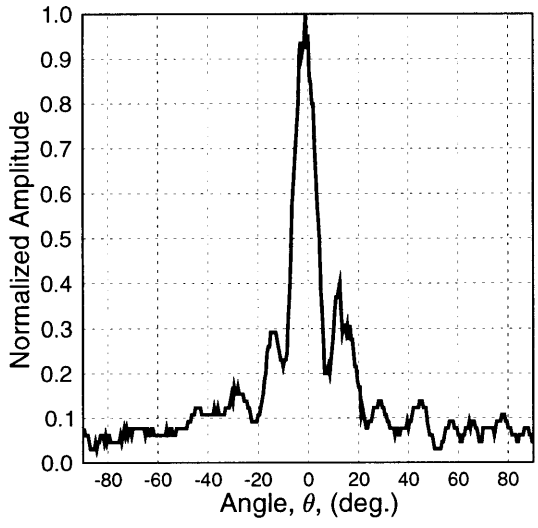

(c) Experimental: focusing at θ=0°

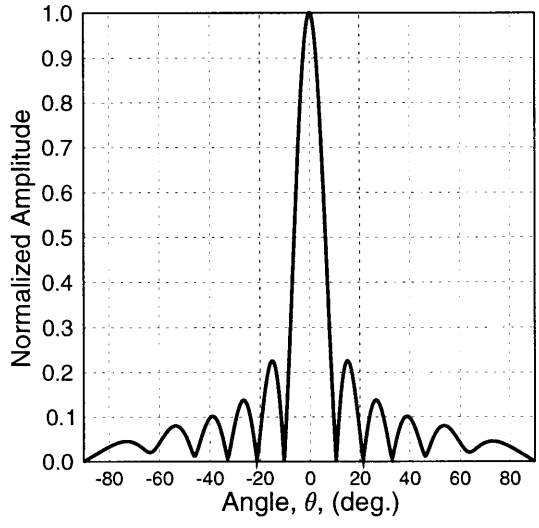

(d) Simulated: focusing at θ=0°

Figure 7.1: Experimental and simulated results demonstrating steering as compared to focusing behavior in mortar (R=30.48cm, F=30.48cm, N=8, c=3650m/s, f=170kHz, d=0.7λ, and θ=0^o).

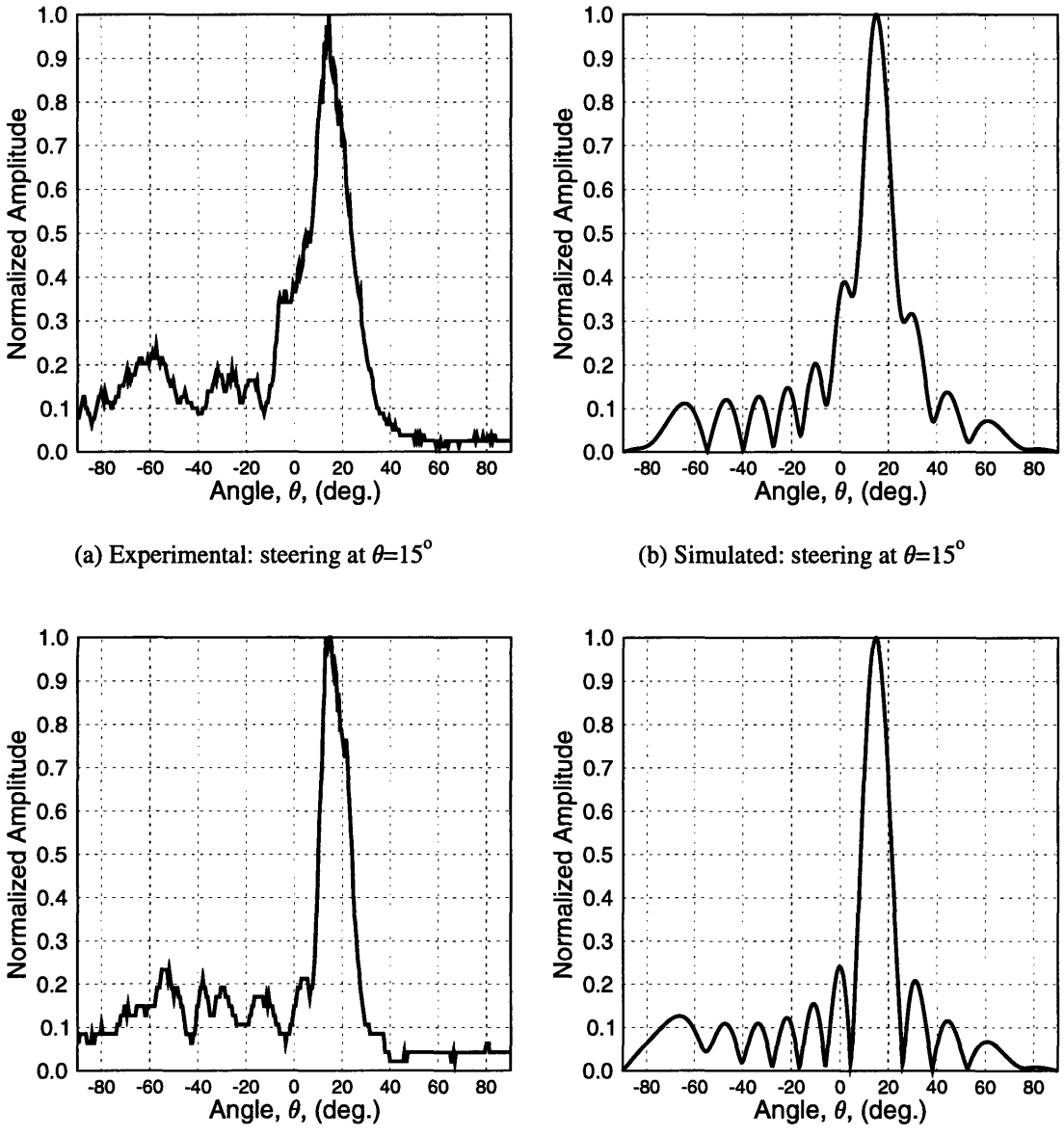

(a) Experimental: steering at θ=15°

(b) Simulated: steering at θ=15°

(c) Experimental: focusing at θ=15°

(d) Simulated: focusing at θ=15°

Figure 7.2: Experimental and simulated results demonstrating steering as compared to focusing behavior in mortar (R=30.48cm, F=30.48cm, N=8, c=3650m/s, f=170kHz, d=0.7λ, and θ=15^o).

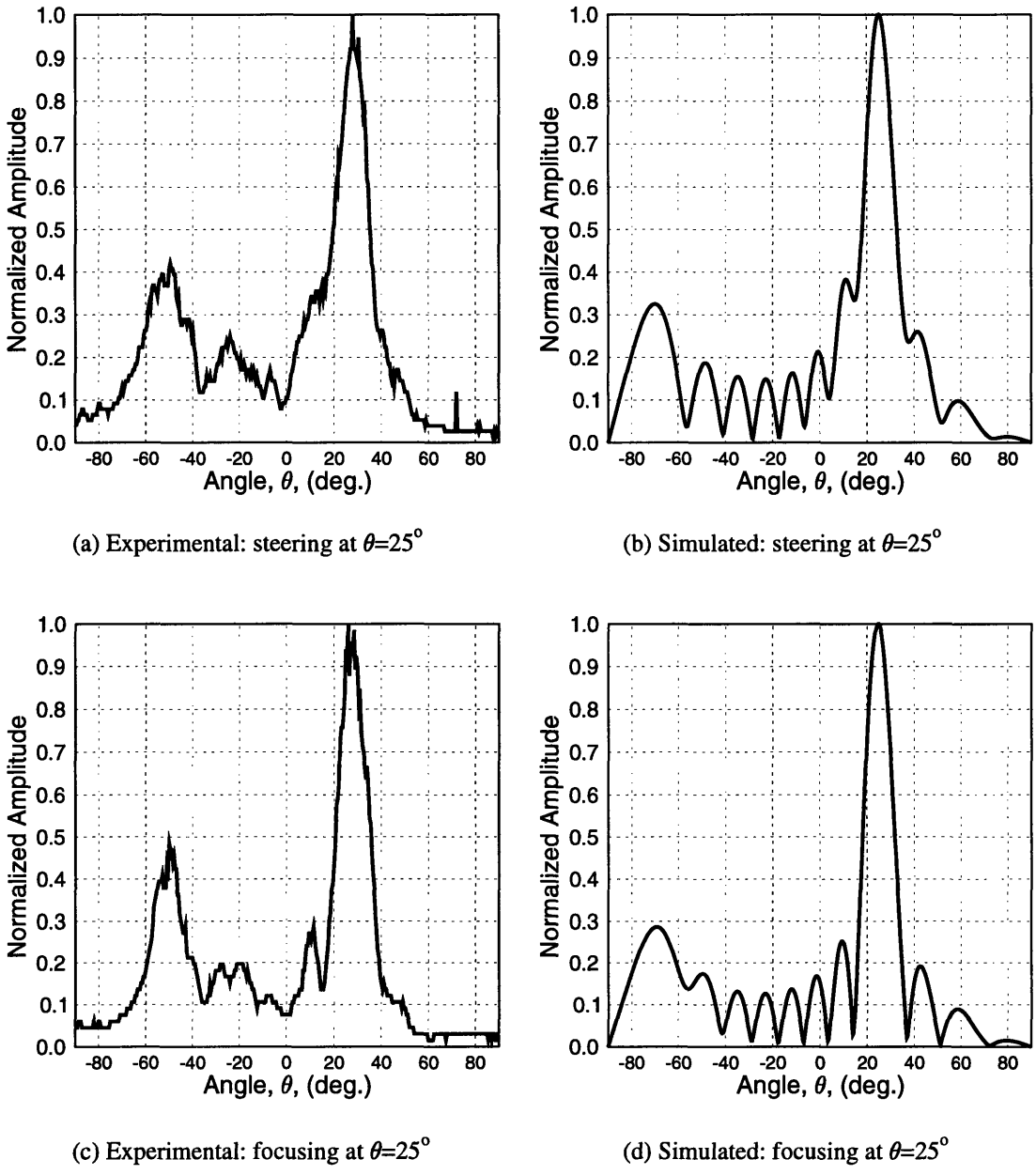

(a) Experimental: steering at θ=25°

(b) Simulated: steering at θ=25°

(c) Experimental: focusing at θ=25°

(d) Simulated: focusing at θ=25°

Figure 7.3: Experimental and simulated results demonstrating steering as compared to focusing behavior in mortar (R=30.48cm, F=30.48cm, N=8, c=3650m/s, f=170kHz, d=0.7λ, and θ=25^o).

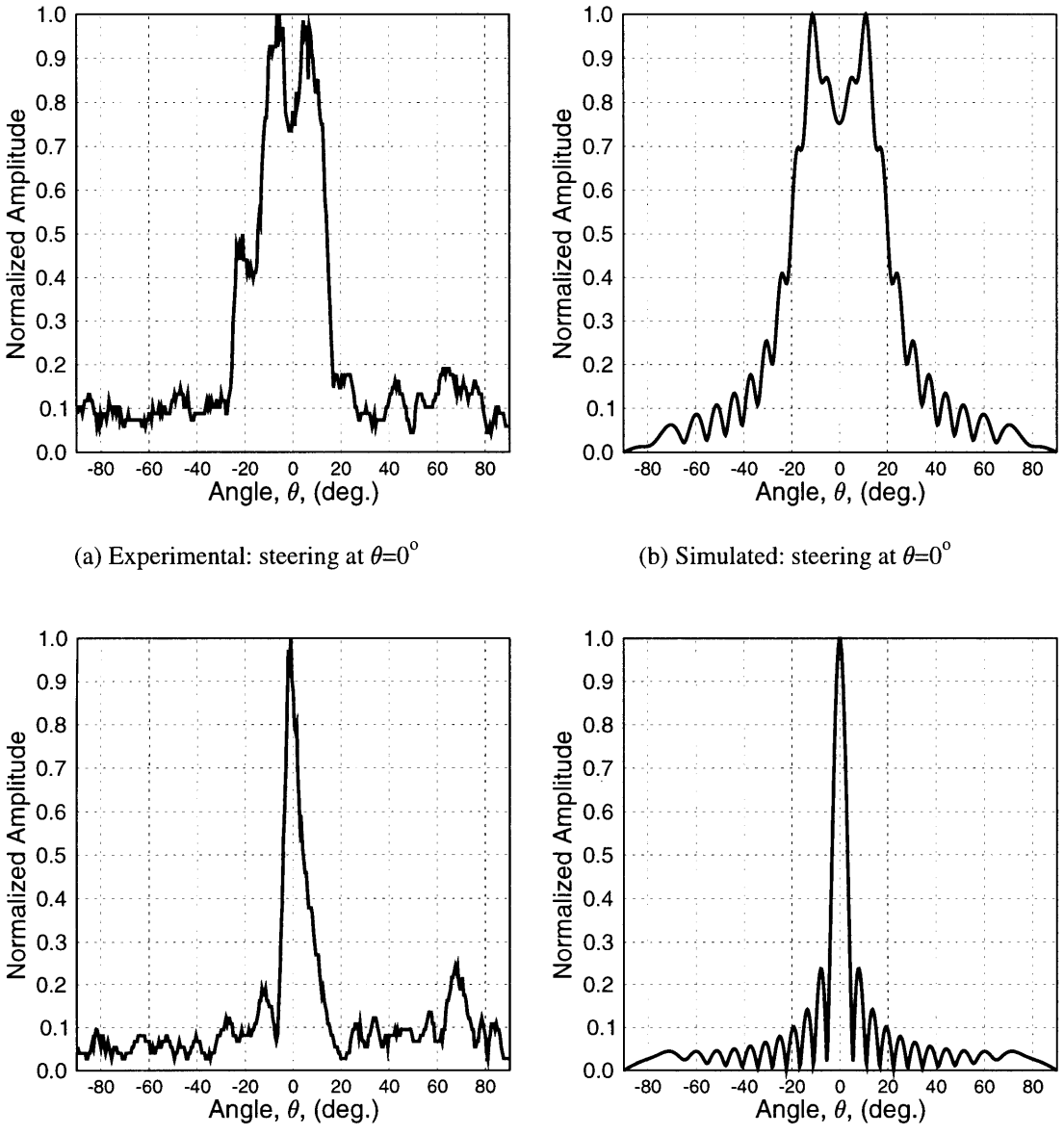

(a) Experimental: steering at θ=0°

(b) Simulated: steering at θ=0°

(c) Experimental: focusing at θ=0°

(d) Simulated: focusing at θ=0°

Figure 7.4: Experimental and simulated results demonstrating steering as compared to focusing behavior in mortar (R=30.48cm, F=30.48cm, N=16, c=3650m/s, f=170kHz, d=0.7λ, and θ=0^o).

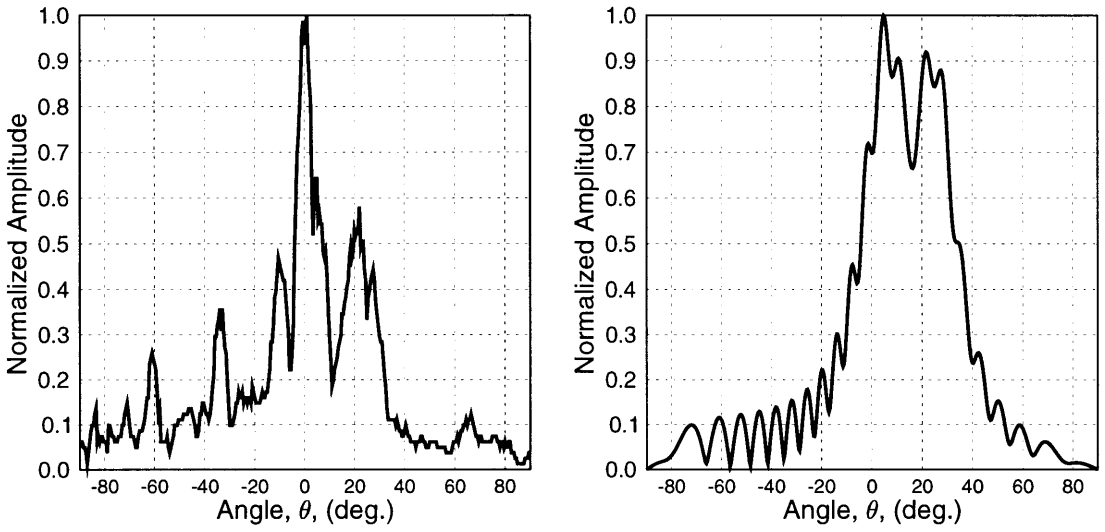

(a) Experimental: steering at θ=15^{o}

(b) Simulated: steering at θ=15^{o}

(c) Experimental: focusing at θ=15^{o}

(d) Simulated: focusing at θ=15^{o}

Figure 7.5: Experimental and simulated results demonstrating steering as compared to focusing behavior in mortar (R=30.48cm, F=30.48cm, N=16, c=3650m/s, f=170kHz, d=0.7λ, and θ=15^{o}).

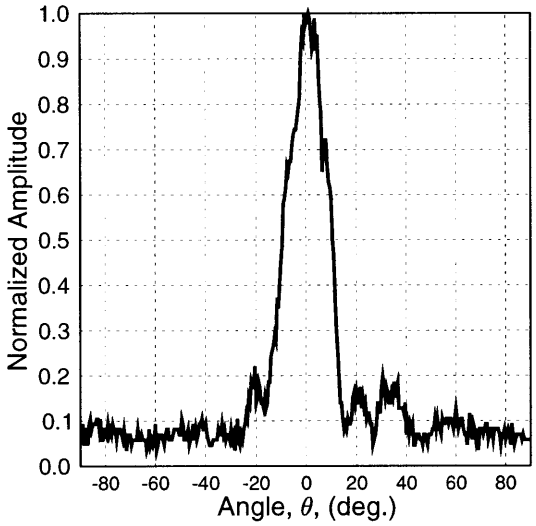

(a) Experimental: steering at θ=0°

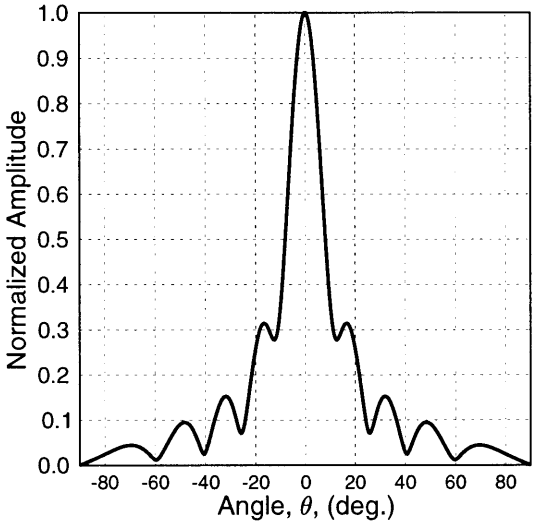

(b) Simulated: steering at θ=0°

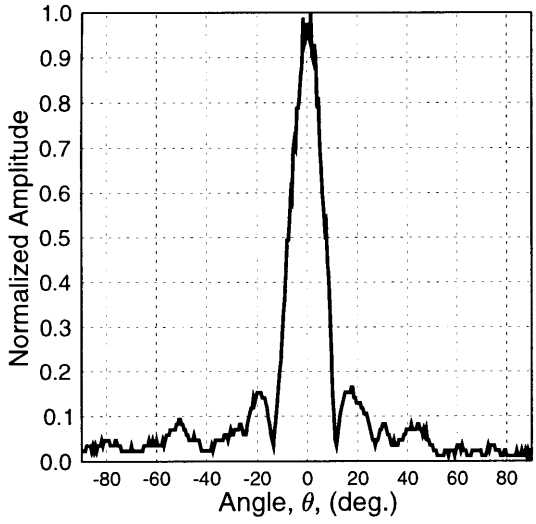

(c) Experimental: focusing at θ=0°

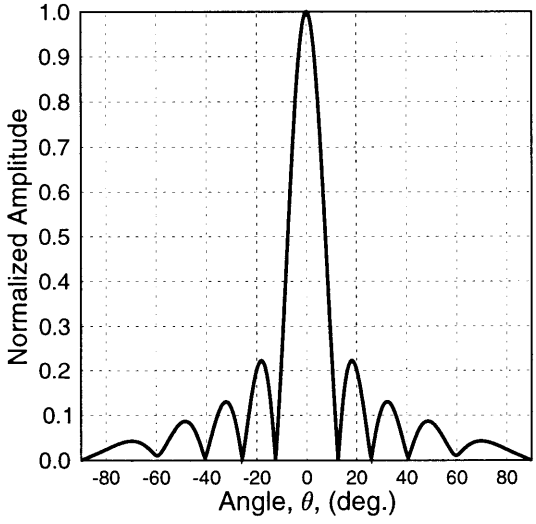

(d) Simulated: focusing at θ=0°

Figure 7.6: Experimental and simulated results demonstrating steering as compared to focusing behavior in concrete (R=30.48cm, F=30.48cm, N=8, c=3500m/s, f=140kHz, d=0.582λ, and θ=0^o).

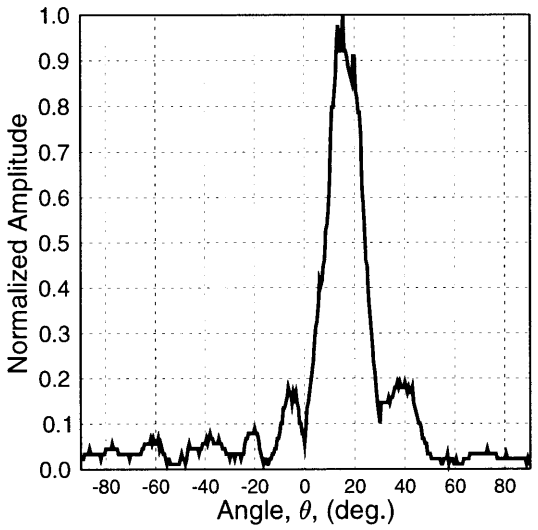

(a) Experimental: steering at θ=15^{o}

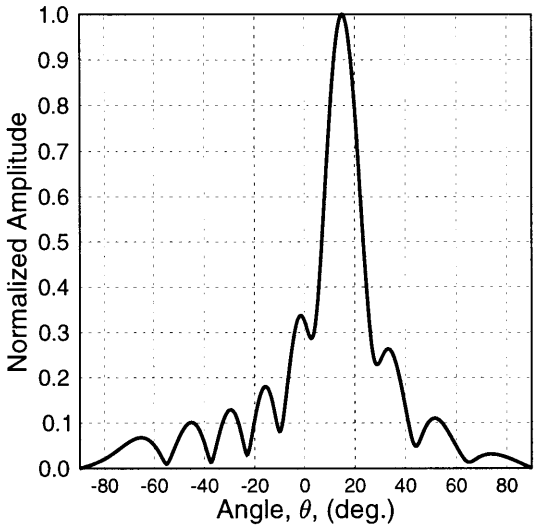

(b) Simulated: steering at θ=15^{o}

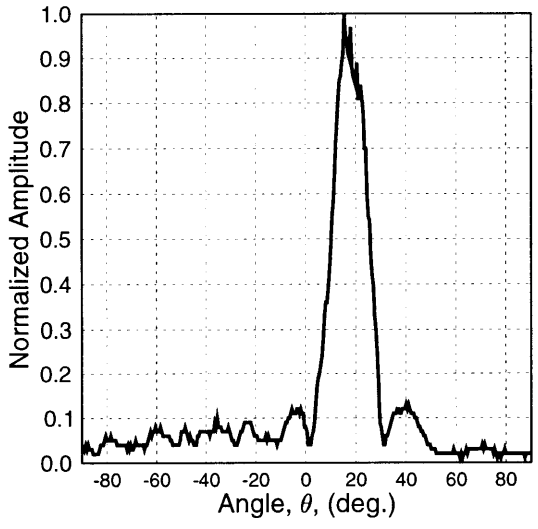

(c) Experimental: focusing at θ=15^{o}

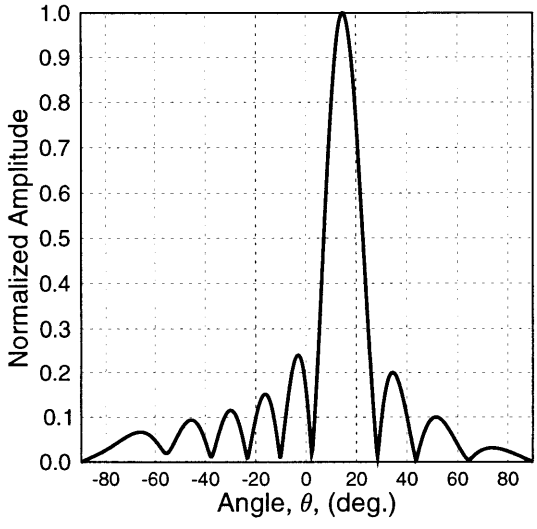

(d) Simulated: focusing at θ=15^{o}

Figure 7.7: Experimental and simulated results demonstrating steering as compared to focusing behavior in concrete (R=30.48cm, F=30.48cm, N=8, c=3500m/s, f=140kHz, d=0.582λ, and θ=15^{o}).

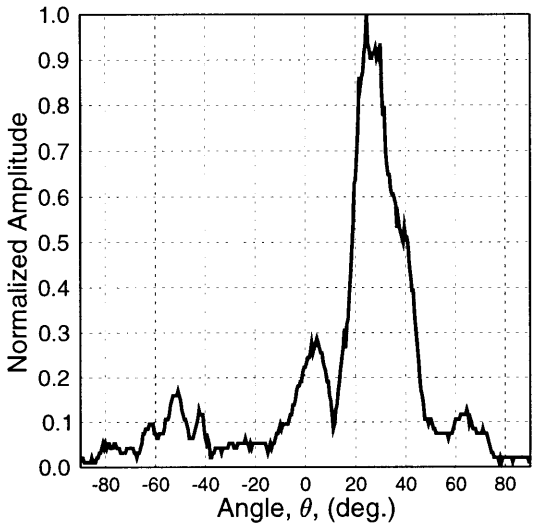

(a) Experimental: steering at θ=25°

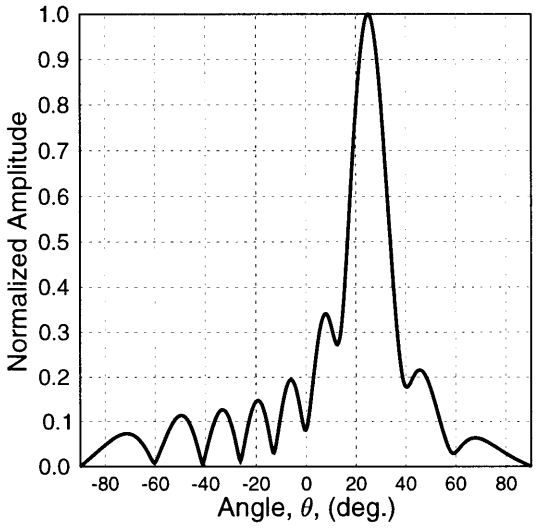

(b) Simulated: steering at θ=25°

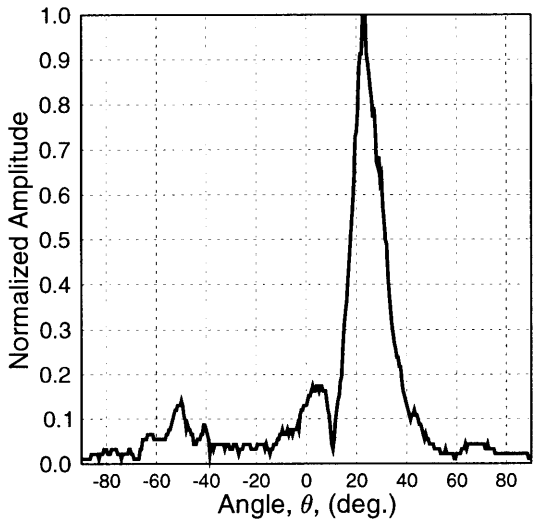

(c) Experimental: focusing at θ=25°

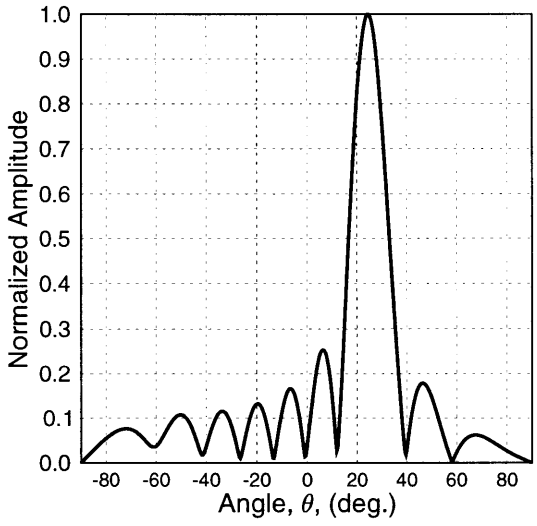

(d) Simulated: focusing at θ=25°

Figure 7.8: Experimental and simulated results demonstrating steering as compared to focusing behavior in concrete (R=30.48cm, F=30.48cm, N=8, c=3500m/s, f=140kHz, d=0.582λ, and θ=25^o).

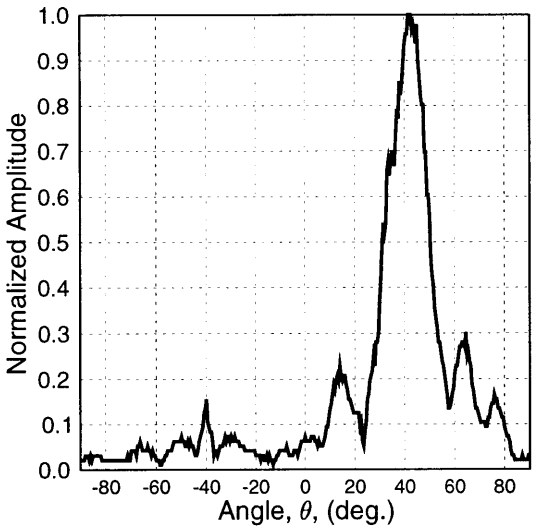

(a) Experimental: steering at θ=40°

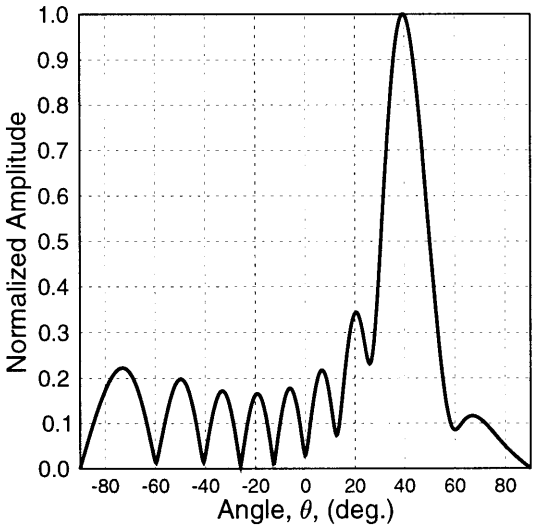

(b) Simulated: steering at θ=40°

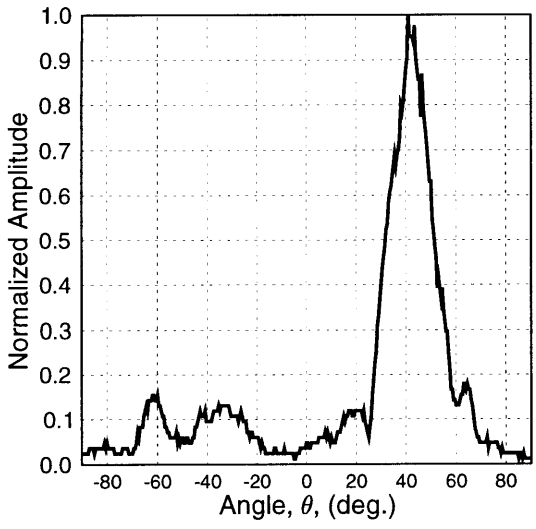

(c) Experimental: focusing at θ=40°

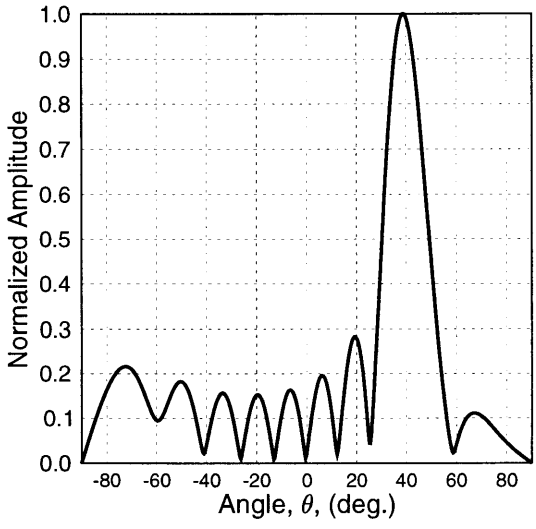

(d) Simulated: focusing at θ=40°

Figure 7.9: Experimental and simulated results demonstrating steering as compared to focusing behavior in concrete (R=30.48cm, F=30.48cm, N=8, c=3500m/s, f=140kHz, d=0.582λ, and θ=40^o).

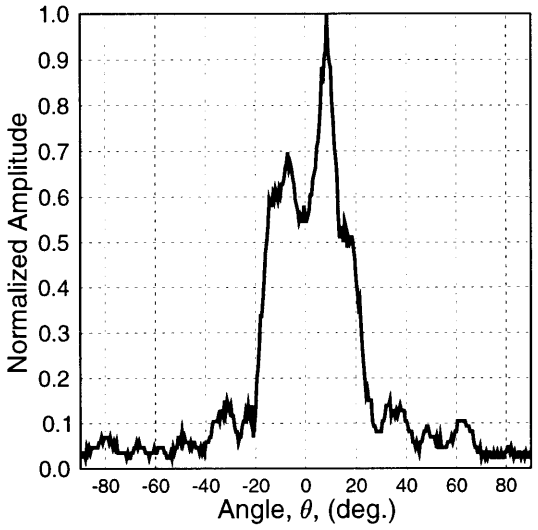

(a) Experimental: steering at θ=0°

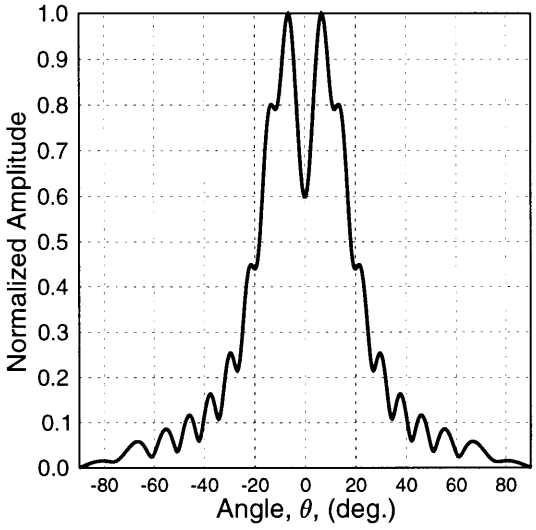

(b) Simulated: steering at θ=0°

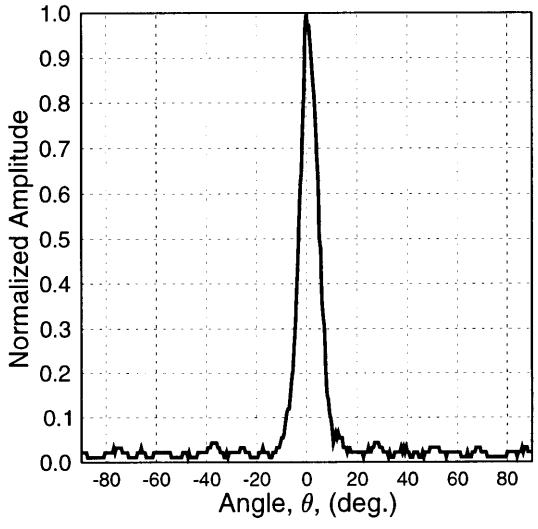

(c) Experimental: focusing at θ=0°

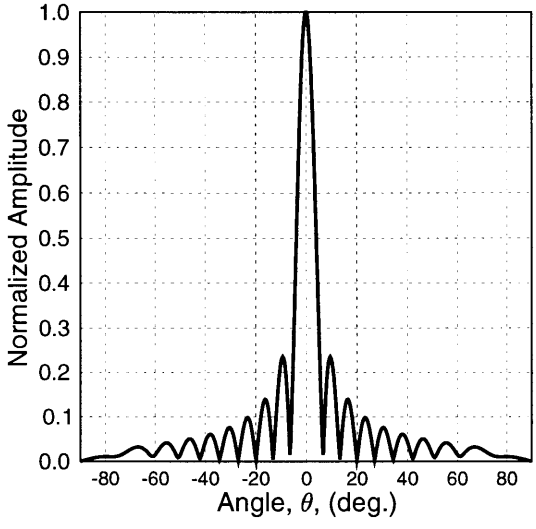

(d) Simulated: focusing at θ=0°

Figure 7.10: Experimental and simulated results demonstrating steering as compared to focusing behavior in concrete (R=30.48cm, F=30.48cm, N=16, c=3500m/s, f=140kHz, d=0.582λ, and θ=0^o).

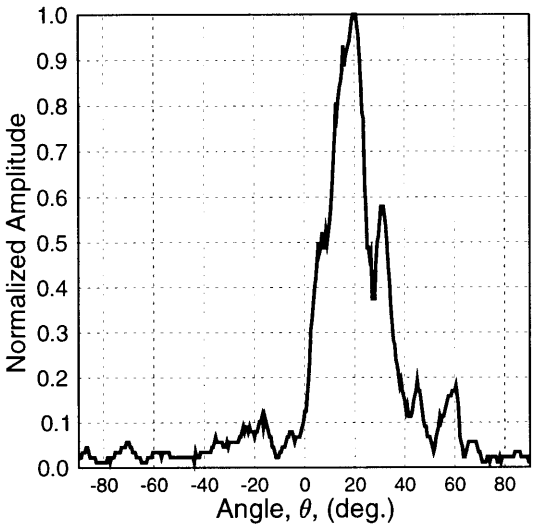

(a) Experimental: steering at θ=15°

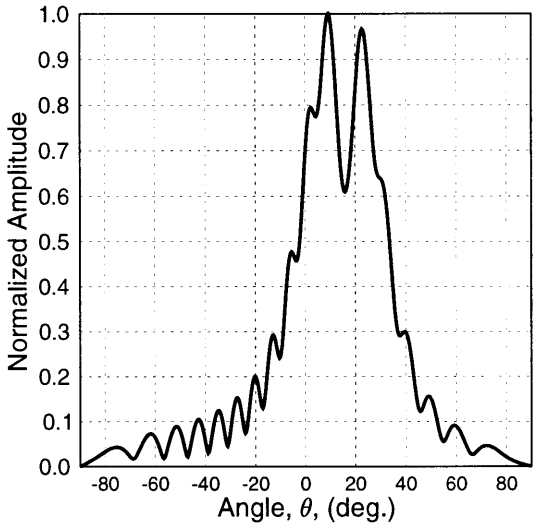

(b) Simulated: steering at θ=15°

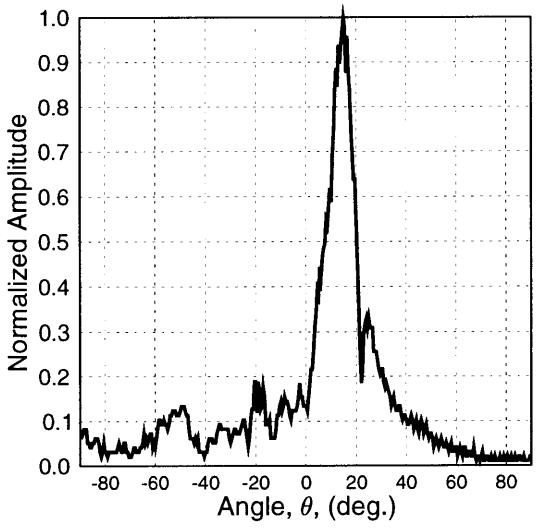

(c) Experimental: focusing at θ=15°

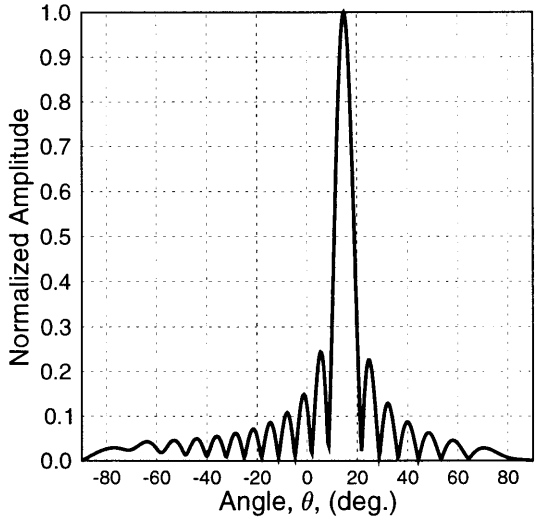

(d) Simulated: focusing at θ=15°

Figure 7.11: Experimental and simulated results demonstrating steering as compared to focusing behavior in concrete (R=30.48cm, F=30.48cm, N=16, c=3500m/s, f=140kHz, d=0.582λ, and θ=15^o).

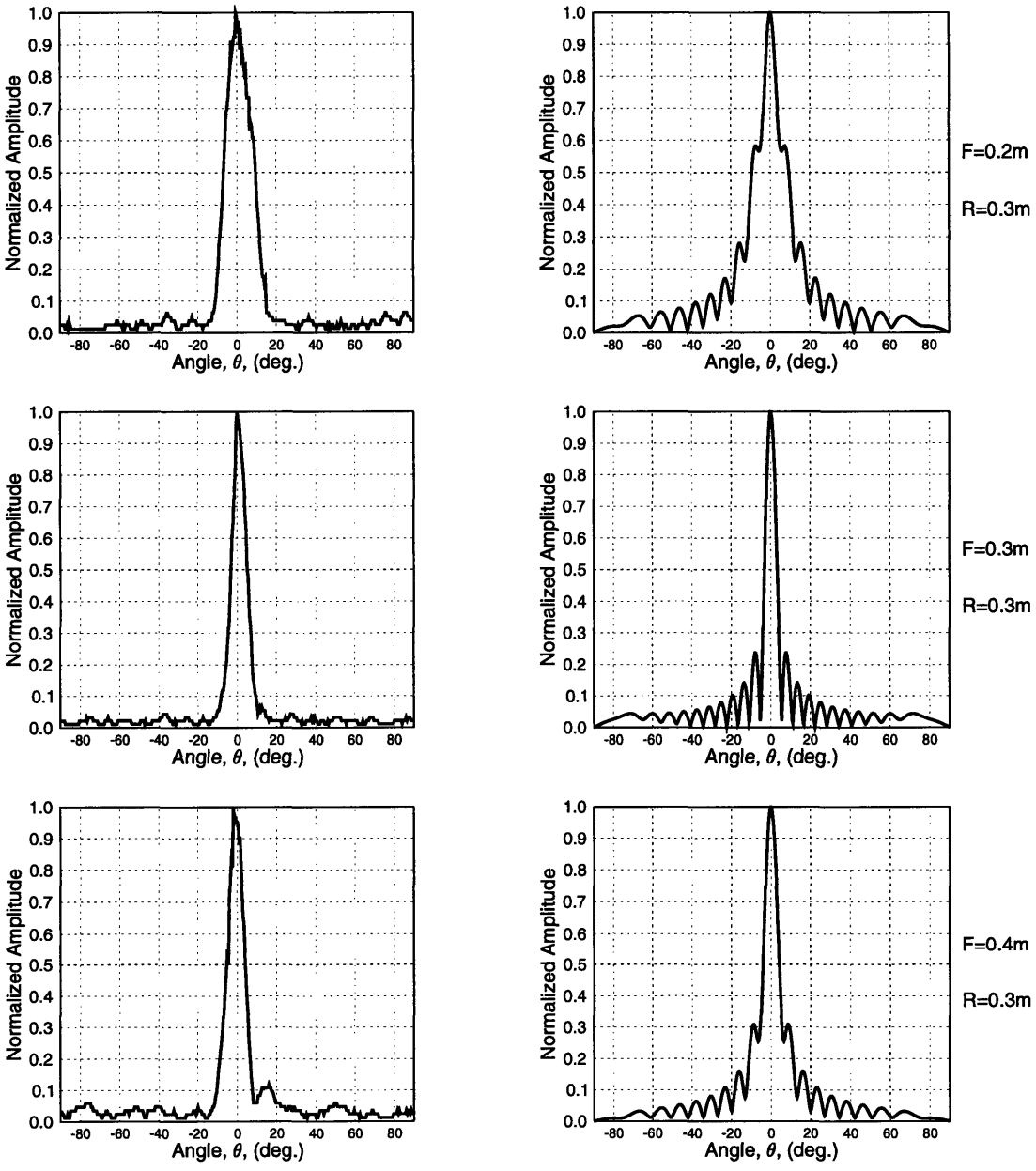

Figure 7.12: Experimental and simulated results demonstrating the behavior of focusing at a constant directivity distance for various focal lengths: (R=30.48cm, N=16, c=3500m/s, f=140kHz, d=0.582λ, and θ=0^o).

Chapter 8

Conclusion

A comprehensive examination of low-frequency ultrasonic phased arrays for the condition assessment of concrete structures was undertaken, revealing without a doubt that phase steering and focusing is possible in concrete and other cementitious materials. The directivity results demonstrate that the array can both steer and focus with exceptional steerability and accuracy, when compared to the proven numerical simulation. The behavior of focusing became a central issue in this study, as the inherent use of low-frequency ultrasound creates a significant near field zone where the directivity of steering is poor. A thorough examination of the benefits of focusing over steering within the transition zone of the array was accomplished analytically, numerically, and most importantly, experimentally.

8.1 Research Summary

A numerical simulation program was developed, in accordance with accepted simulation standards, which provides directivity plots, pressure distributions, and other pressure profiles for both steering and focusing of an ultrasonic phased array. Since an analytical pressure distribution for beam focusing cannot be attained, this numerical simulation provided an invaluable tool for determining the accuracy of the experimental focusing results. This model computed each element as an assemblage of discrete point sources, modified by a per element $\cos(\theta)$ envelope.

The traditional focusing formula was found to be deficient, as it could only be used for an array with an odd number of elements, and was also very clumsy to utilize because of a required constant, t_0. An improved formulation was derived, valid for even and odd numbered arrays.

An automated testing assembly was manufactured to validate the use of phased arrays in a cementitious medium, and to confirm the theoretical findings discussed above. A mortar and concrete disk was constructed, which was mounted on a programmable step motor. The phased array sensor was placed in a rectangular groove in the center of the disk, and focused/steered under various parameter settings. The disk was turned from -90° to 90° for each case, and the data obtained by a focused immersion receiver was used to construct experimental directivities.

Directivity is the key parameter used to evaluate the steerability and accuracy of a phased array. Steerability measures the correlation of the measured θ_s to the expected θ_s, which exhibited an average variation of only 0.75°. As mentioned, good accuracy implies a close match of the main lobe widths between the experimental and simulated directivities, which can be evaluated using a main lobe sharpness factor of $q_{-6dB} \cdot 180°$. The average deviation from the simulation in $q_{-6dB} \cdot 180°$ was only 1.4°.

A thorough numerical and experimental examination of the benefits of focusing over steering was made. The major observations were that focusing greatly enhances the directivity within the near field of an array, and that focusing converges to steering in the far field.

8.2 Future Work and Concluding Remarks

A key function of an ultrasonic phased array for NDE applications is the ability to image flaws, and other anomalies, that are located within the media. A concrete specimen representative of a typical imaging application has already been constructed, as shown in figure 8.1, which measures 63.5 cm in height, 77.5 cm in width, and 28 cm in thickness. This concrete "wall" has six 2.5 cm diameter through-holes and one rebar.

The largest limitation for adequate imaging is the supporting electronic system, which was initially designed for steel applications. A new circuit, designed by Coach Wei, is currently being fabricated, and will be available shortly. This system is far more advanced than that used in the directivity study, enabling transmiting and receiving from as high as 4,096 channels, with much improved range and resolution. The following are some key specifications:

- Computer Interface: Digital I/O Board or other ports
- Addressable Channel Number: 4,096
- Required I/O from Control Computer: 34
- Power: 110 volts/60 Hz(or: 220 volts/50 Hz)
- Minimum Pulse Width: 100 ns
- Pulse Rate: 0 Hz to 500 kHz
- Pulse Polarity: negative
- Pulse Magnitude: 80 to 500 volts
- Pulse Shape: rectangle
- Pulse Width: adjustable at a step of 100 ns
- Pulse Delay: Adjustable from 0 to 6.5 ms
- Pulse Delay Resolution: 0.5 ns

This circuit was specifically designed to meet the requirements needed for imaging of concrete structures. The most important parameter is the range of the pulse delays (6.5 ms), which will allow 180° steerability. The delay resolution of 0.5 ns will also allow exception angular resolution needed for image reconstruction. The linear phased array will utilized at most 32 elements, but a matrix array being developed may have

as many as 1024 elements (32x32). The system was designed to support, at most, a 64x64 matrix array.

A suitable linar phased array, optimized for proper imaging of cementitious materials, is still under construction. This sensor differs from that used in the directivity study in that the elevation distance "L" is approximately eight times the wavelength, which reduces the elevation angle to under 20°. It will also contain two matching layers, including an RTV layer for dry contact imaging. The sensor needs to be carefully designed, to obtain an optimum balance of transmitting and receiving efficiency. Exceptional imaging capabilities is expected, based on the the directivities obtained, and continued research aims to prove this.

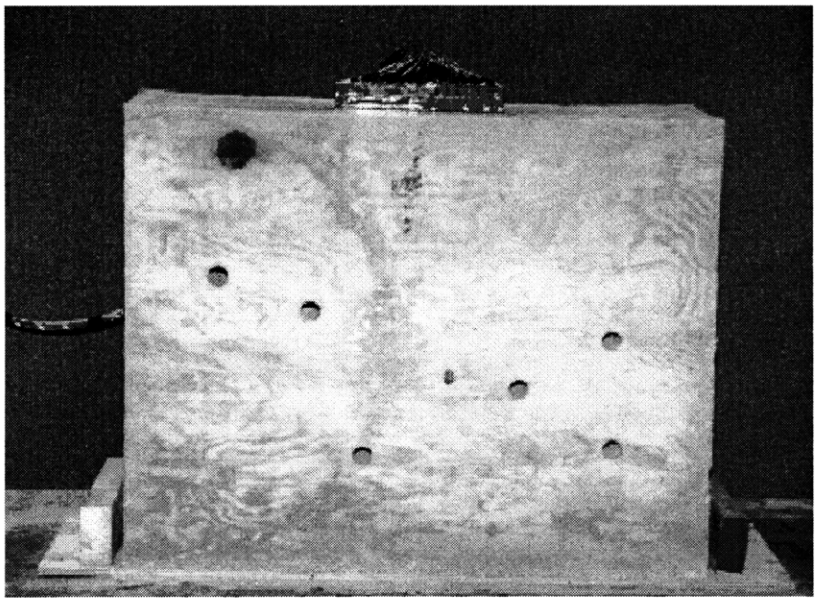

Figure 8.1: Concrete sample, with a phased array sensor imaging voids and rebar.

Appendix A

Analytical Pressure Distribution for Beam Focusing

A procedure leading to the derivation of the approximate pressure distribution for beam focusing was attempted. Unlike the case of steering [45], which resulted in an analytical solution, the results for focusing yielded an unclosed form.

A.1 Time delay simplification

According to Taylor's series expansion, the distance from the focal point to the n^{th} element:

$$r_n = \sqrt{r^2 + (nd)^2 - 2r(nd)\sin\theta_s} \approx r - (nd)\sin\theta_s + \frac{1}{2r}(nd)^2\cos^2\theta_s \,, \tag{A.1}$$

for the case $r \gg nd$, where r is the distance from the focal point to the 0^{th} element and $n = 0, 1, \cdots, N-1$. Similarly, equation (5.6) can be rewritten as:

$$\begin{aligned} &\left[1 + \left(\frac{d}{F}\left(n - \frac{N-1}{2}\right)\right)^2 - 2\sin\theta_s \frac{d}{F}\left(n - \frac{N-1}{2}\right)\right]^{1/2} \\ &\approx 1 - \sin\theta_s \frac{d}{F}\left(n - \frac{N-1}{2}\right) + \frac{1}{2}\cos^2\theta_s \frac{d^2}{F^2}\left(n - \frac{N-1}{2}\right)^2 \,, \end{aligned} \tag{A.2}$$

which gives rise to the time delay between the n^{th} and $(n-1)^{\text{th}}$ elements:

$$\begin{aligned}\Delta\tau_n &= t_n - t_{n-1} \\ &= \frac{F}{c}\left\{\left[1 - \sin\theta_s \frac{d}{F}\left(n - 1 - \frac{N-1}{2}\right) + \frac{1}{2}\cos^2\theta_s \frac{d^2}{F^2}\left(n - 1 - \frac{N-1}{2}\right)^2\right]\right. \\ &\quad \left. - \left[1 - \sin\theta_s \frac{d}{F}\left(n - \frac{N-1}{2}\right) + \frac{1}{2}\cos^2\theta_s \frac{d^2}{F^2}\left(n - \frac{N-1}{2}\right)^2\right]\right\}.\end{aligned} \tag{A.3}$$

Further we can get the equation after simplification:

$$\Delta\tau_n = \frac{d\sin\theta_s}{c} + \frac{1}{2}\cos^2\theta_s \frac{d^2}{cF}(N - 2n)\,. \tag{A.4}$$

By substituting eq. (4.1) into eq. (A.4), the time delay for the focusing with steering angle θ_s is:

$$\Delta\tau_n = \Delta\tau_0 + \frac{c\Delta\tau_0^2}{2F\tan^2\theta_s}(N - 2n)\,. \tag{A.5}$$

This means the time delay between neighboring elements (n^{th} and $(n-1)^{\text{th}}$) for the focusing, along with steering effect, is a second order polynomial of the time delay for pure steering $\Delta\tau_0$.

Therefore the time delay between the n^{th} and the 0^{th} elements, say Δt_n, is the summation of the time delay between two neighboring elements $\Delta\tau_i$, where $i = 1, 2, \cdots, n$:

$$\begin{aligned}\Delta t_n &= \Delta\tau_1 + \Delta\tau_2 + \ldots + \Delta\tau_n \\ &= n\Delta\tau_0 + \frac{c\Delta\tau_0^2}{2F\tan^2\theta_s}\left[nN - (2 + 4 + 6 + \ldots + 2n)\right] \\ &= n\Delta\tau_0 + \frac{c\Delta\tau_0^2}{2F\tan^2\theta_s}(nN - n^2 - n)\,.\end{aligned} \tag{A.6}$$

A.2 Analytical pressure distribution

For a single element, the pressure distribution can be expressed as: [65]

$$p(r,\theta,t) = \frac{p_0}{r}\frac{\sin\left(\frac{ka\sin\theta}{2}\right)}{\frac{k\sin\theta}{2}}\exp\left(-\frac{jka\sin\theta}{2}\right)\exp\left[j(\omega t - kr)\right]. \tag{A.7}$$

According to Huyghens' principle, the pressure distribution of the phased arrays for focusing and steering is the superposition of the pressure of single elements:

$$\begin{aligned} p(r,\theta,t) &= \sum_{n=0}^{N-1} p_n(r,\theta,t) \\ &= \sum_{n=0}^{N-1} \frac{p_0}{r}\frac{\sin\left(\frac{ka\sin\theta}{2}\right)}{\frac{k\sin\theta}{2}}\exp\left(-\frac{jka\sin\theta}{2}\right)\exp\left[j(\omega t_n - kr_n)\right] \\ &\approx \sum_{n=0}^{N-1} \frac{p_0}{r}\frac{\sin\left(\frac{ka\sin\theta}{2}\right)}{\frac{k\sin\theta}{2}}\exp\left(-\frac{jka\sin\theta}{2}\right)\exp\left[j\Big(\omega(t-\Delta t_n) - k(r - nd\sin\theta)\Big)\right]. \end{aligned} \tag{A.8}$$

With the assistance of eq. (A.6), we have the final expression of pressure distribution for beam focusing:

$$\begin{aligned} &p(r,\theta,t) \\ &= \frac{p_0 a}{r}\frac{\sin\left(\frac{ka\sin\theta}{2}\right)}{\frac{ka\sin\theta}{2}}\exp\left(-\frac{jka\sin\theta}{2}\right)\left(\sum_{n=0}^{N-1}\exp[j(An + Bn^2)]\right)\exp[j(\omega t - kr)], \end{aligned} \tag{A.9}$$

where:

$$
\begin{aligned}
A &= \frac{c(N-1)}{2F\tan^2\theta_s}\Delta\tau_0^2 - \omega\Delta\tau_0 + kd\sin\theta \ , \\
B &= \frac{c\Delta\tau_0^2}{2F\tan^2\theta_s} \ .
\end{aligned}
\tag{A.10}
$$

Bibliography

1. Krautkrämer, J. and H. Krautkrämer, (1990), *Ultrasonic testing of materials*, 4th ed., Springer-Verlag, New York.

2. Sansalone, M. and N. J. Carino (1991), "Stress wave propagation methods," *CRC Handbook on Nondestructive Testing of Concrete*, ed., V.M. Malhotra and N.J. Carino, CRC Press, p. 275-304.

3. Von Ramm, O. T. and S. W. Smith (1983), "Beam steering with linear arrays," *IEEE Transactions on Biomedical Engineering*, BME-30(8), August, 438–452.

4. Thomas, J. L. and M. A. Fink (1996), "Ultrasonic beam focusing through tissue inhomogeneities with a time reversal mirror: application to transskull therapy," *IEEE Trans. on Ultrasonics, Ferroelectrics, and Frequency Control*, 43(6), November, 1122–1129.

5. Weyman, A. E. (1994), *Principles and Practice of Echocardiography*, Lea & Febiger, Philadelphia.

6. McNab, A. and M. J. Campbell (1987), "Ultrasonic phased arrays for nondestructive testing," *NDT International*, 20(6), December, 333–337.

7. Hatfield, J. V., N. R. Scales, A. D. Armitage, P. J. Hicks, Q. X. Chen, and P. A. Payne (1994), "An integrated multi-element array transducer for ultrasound imaging," *Sensors and Actuators A*, 41–42, 167–173.

8. Malhotra, V. M. and N. J. Carino (1991), *CRC handbook on nondestructive testing of concrete*, CRC press.

9. Mehta, P. K., Monteiro, P. (1993), *Concrete: structure, properties, and materials*, Second Edition, Prentice Hall, New Jersey, 122–129.

10. Chrest, A. P. (1989), *Parking structures: planning, design, construction, maintenance, and repair*, Van Nostrand Reinhold, New York, 265.

11. Federal Highway Administration (1990), "Our nation's highways: selected facts and figures," *U.S. Department of Transportation*, Publication No. FHWA A-PL-90-024.

12. Wooh, S. C (1995), "Role of NDE in civil infrastructure condition assessment," present and future, Keynote Lecture, *International Workshop for Application of NDT Technology for Failure Prevention*, Jointly organized by Korean Society for Nondestructive Testing (KSNT) and Research Institute of Mechanical Technology (RIMT) of Pusan National University, Oct. 18–20).

13. Malhotra, V. M. (1976), *Testing hardened concrete: nondestructive methods*, Monograph No. 9, American Concrete Institute, Detroit, 204.

14. Krause, M., O. Bärmann, K. Langenberg, Krautkrämer (1995) "comparison of pulse-echo-methods for testing concrete," TOC regarding Ultrasound, *International Symposium Non-Destructive Testing in Civil Engineering*, Berlin,

15. Bungey, J., S. Millard, T. Molyneaux, J. Zhou (1995), "Radar assessment of structural concrete using neural networks," *NDT&E International*, 28(5), 281–288.

16. Buyukozturk, O., H. Rhim (1995), "Non-destructive testing of concrete using radar," *International Symposium Non-Destructive Testing in Civil Engineering*, 1, 85–93.

17. Clemena, G. (1991) "Short-pulse radar methods",*CRC Handbook on Nondestructive Testing of Concrete*, Editors, V.M. Maholtra and N.J. Carino, CRC Press, 253–274.

18. Cone, G. L., P. S. Nowak, R. Zoughi (1991), "Microwave nondestructive detection of rebars in concrete slabs," *Materials Evaluation*, Volume 49, No. 11, pp. 1385-7.

19. Diener, L. (1995), "Microwave near-field imaging with open-ended waveguide - comparison with other technique of nondestructive testing," *Research in Nondestructive Evaluation*, 7:137-152

20. Zoughi, R., (1995), "Microwave and millimeter wave nondestructive testing: a succinct introduction", *Research in Nondestructive Evaluation*, 7:71–75.

21. Eales, J., F. Holt (1987), "Nondestructive evaluation of pavements," *Concrete International*, Volume 9, No. 6, 41–45.

22. de Vekey, R. C. (1990), "Non-destructive evaluation of structural concrete: a review of european practice and developments," *Proceedings Nondestructive*

Evaluation of Civil Structures and Materials, University of Colorado, Boulder, Colorado. 26.-28.09.

23. Weil, G. (1991), "Infrared Thermographic Techniques", *CRC Handbook on Nondestructive Testing of Concrete*, Editors, V.M. Maholtra and N.J. Carino, CRC Press, 305–316.

24. Rhim, H. C. (1995), "Nondestructive evaluation of concrete using wideband microwave techniques", *Massachusetts Institute of Technology*, Department of Civil Engineering.

25. Olson, L., Sack, D. (1995), "Advanced NDT method for evaluating concrete bridges and other structures", *NDT&E International*, Volume 28, No. 6, 349–357.

26. Geng, Y. (1992), "Finite element assessment of cracks and delaminations in concrete bridge decks by the impact-echo method", *Massachusetts Institute of Technology*, Department of Civil Engineering.

27. Berthelot, J.-M., M. Ben Souda, and J. L. Robert (1994), "Identification of signals in the context of acoustic emission in concrete," *Journal of Nondestructive Evaluation*, 13(2), 63–73.

28. Landis (1994) "Development in NDE of concrete," *Northwestern University Center for Advanced Cement-Based Materials and BIRL Industrial Research Laboratory*, June.

29. Charlesworth, J. P. and J. A. G. Temple (1989), *Ultrasonic time-of-flight diffraction*, Research Studies Press LTD., Somerset, England.

30. Achenbach, J. D., I. N. Komsky, Y. C. Lee, and Y. C. Angel (1992), "Self-calibrating ultrasonic technique for crack depth measurement," *Journal of Nondestructive Evaluation*, 11(2), 103–107.

31. Galan, A. (1990), "Combined ultrasound Methods of Concrete Testing," *Developments in Civil Engineering*, 34, Elsevier, New York.

32. Turnbull, D. H. and F. S. Foster (1992), "Fabrication and characterization of transducer elements in two-dimensional arrays for medical ultrasound imaging," *IEEE Transactions on Ultrasonics, Ferroelectrics, and Frequency Control*, 39(4), July, 464–475.

33. Lemon, D. K. and G. J. Posakony (1980), "Linear array technology in NDE applications," *Mat. Eval.* July, 34–37.

34. AWS (1985), *Guide for the Nondestructive Inspection of Welds*, ANSI/AWS B1.10-86, American Welding Society.

35. Chinn, D.J. (1994), *Long-distance ultrasonic testing of steel structures*, Heron, (1).

36. Ditchburn, R.J., S.K. Burke and C.M. Scala (1996), "NDT of welds: state of the art," *NDT&E International*, 29(2), 111–117.

37. Lovejoy, A., P. Pedrick, A. Doran, T. A. Delchar, J.A. Mills, A. Stamm (1995), "A novel 8-bit ultrasound phased-array controller for hyperthermia applications," *Ultrasonics*, 33(1).

38. Buchanan, M. T. and K. Hynynen (1994), "Design and experimental evaluation of an intracavity ultrasound phased array system for hyperthermia," *IEEE Trans. on Biomedical Engineering*, 41(12), Dec., 1178–1187.

39. Oeftering, R. C. (1997), NASA Technical Briefs, LEW-16189.

40. Schwarz, H. P. (1987), *Mat. Eval.*, 45, 951.

41. Beardsley, B., M. Peterson, and J. D. Achenbach (1995), "A simple scheme for self-focusing of an array," *Journal of Nondestructive Evaluation*, 14(4), 169–179.

42. Mak, D.K. (1991), "Ultrasonic imaging analysis using a multi-transducer technique," *Ultrasonics*, 29, 308–311.

43. Mahaut, S. and G. Cattiaux (1996), "Applications of dynamic adaptive focusing to ultrasonic non destructive testing." *Review in progree in QNDE*, Vol 15.

44. Armitage, A. D., N. R. Scales, P. J. Hicks, P. A. Payne, Q. X. Chen, and J. V. Hatfield (1995), "An integrated array transducer receiver for ultrasound imaging," *Sensors and Actuators*, A 46–47, 542–546.

45. Shi Y. (1998), "Modeling of acoustic waves for linear phased arrays," *MIT MS thesis.*

46. Smith, S. W., G. E. Trahey, O. T. von Ramm (1992), "Two-dimensional arrays for medical ultrasound," Ultrasonic Imaging, 14, 213–233.

47. Crombie, P., P. Bascom, R. Cobbold (1997), "Calculating the pulsed response of linear arrays," IEEE Trans.*Ultrasonics, Ferroelectrics, and Frequency Control*, 44(5), 9.

48. Lockwood, G. R. , P.-C. Li, M. O'Donnell, and F. S. Foster (1996), IEEE Trans. Ultrasonics, Ferroelectrics, and Frequency Control, 43(1), 7.

49. Hoctor, R. T. and S. A. Kassam (1994), "Synthetic aperture ultraonic imaging system using a minimum redundancy phased array," U.S. patent 5 278 757.

50. Webb, S. (1996), *The physics of medical imaging*, Institute of Physics Publishing, Bristol and Philadelphia.

51. Mason, W. P. (1948), *Electromechanical transducers and wave filters*, (Van Nostrand, Princeton, N.J..

52. Krimholtz, R., Leedom, D., and Mattaei, G. (1970), "New equivalent circuits for elementary piezoelectric transducers," *Electronics Letters*, 6, 398–399, June.

53. De Silets, C. S. (1978), "Transducer arrays suitable for acoustic imaging," *Ph.D. Dissertation*, Stanford University, Stanford, CA, 1978.

54. Persson, H. W. and C. H. Hertz (1985), "Acoustic impedance matching of medical ultrasound transducer," *Ultrasonics*, March, 83–89.

55. Mitra, R. and T. K. Saksena (1995), "Effect of backing on vibrational amplitude characteristics of a piezoelectric ceramic transdcuer," *Indian Journal of Pure & Applied Physics*, Volume 33, pp210-214, April (1995).

56. Jong, Souquet, Faber and Bom (1985), "Vibration modes, matching layers and grating lobes," *Ultrasonics*, July.

57. Sayers, C. M., and C. E. Tait (1984), "Ultrasonic properties of transducer backing," *Ultrasonics*, March.

58. Silk, M. G. (1984), *Ultrasonic transducerts for nondestructive testing*, Adam Hilger Ltd, Bristol.

59. Wooh, S. C. and Y. Shi (1997), "Influence of phased array element size on beam steering behavior," *Ultrasonics*, accepted for publication.

60. Azar, L, Y. Shi, and S. C. Wooh (1998), "Beam focusing behavior of linear phased arrays," Submitted to *NDT&E International.*

61. Selfridge, A. R., G. S. Kino and B. T. Khuri-Yakub (1980), "A theory for the radiation pattern of a narrow-strip acoustic transducer," *Appl. Phys. Lett.*, 37(1), July, 35–36.

62. Smith, S. W., O. von Ramm, M. Haran, and F. Thurstone, (1979), "Angular response of piezoelectric elements in phased array ultrasound scanner," *IEE Trans. on Sonics and Ultrasonics*, Vol. SU-26, No. 3, May.

63. Greenstein, M., H. Yoshida, and M. S. Seyed-Bolorforosh (1997), "A 2.5 MHz 2D array with Z-axis electricall conductive backing," *IEEE Trans. on Ultrasonics, Fer., and Freq. Cont.*, Vol. 44, No. 5, September.

64. Clay, A. C. (1998), "Development and experimental characterization of ultrasonic phased arrays for nondestructive evaluation," *MIT MS thesis.*

65. Wooh, S. C. and Y. Shi (1998), "Optimization of ultrasonic phased arrays" *Review of Progress in Quantitative Nondestructive Evaluation*, D. O. Thompson and D. E. Chimenti, eds., Plenum Press, New York, in press.